EGG-EES-11478

Seismic Evidence of Conjugate Normal Faulting: the 1984 Devil Canyon Earthquake Sequence Near Challis, Idaho

A thesis
submitted in partial fulfillment
of the requirements for the degree of
Master of Science in Geophysics
Boise State University
Boise, Idaho

Suzette M. Jackson

Published August 1994

Idaho National Engineering Laboratory
EG&G Idaho, Inc.
Idaho Falls, Idaho 83415

Prepared for the
U.S. Department of Energy
Office of Environmental Restoration and Waste Management
Under DOE Idaho Field Office
Contract No. DE-AC07-76ID01570

DISCLAIMER

DISCLAIMER

Portions of this document may be illegible in electronic image products. Images are produced from the best available original document.

The thesis presented by Suzette M. Jackson entitled SEISMIC EVIDENCE OF CONJUGATE NORMAL FAULTING: THE 1984 DEVIL CANYON EARTHQUAKE SEQUENCE NEAR CHALLIS, IDAHO is hereby approved:

James E. Zollweg 7/28/94

Advisor Date

John R. Pelton 7/29/94

Committee Member Date

David W Rodgers 7/26/94

Committee Member Date

K M Hollenbaugh 7-29-94

Graduate Dean Date

ACKNOWLEDGEMENTS

I would like to thank the following individuals who helped with collecting the microearthquake data: Duke Anderson, Regina Henrissey, Tom Bice, Erwin McPherson, Lilian Lingling Leu, and Jimmy Chen. I also thank Charlie Langer, Bob Smith, Jim Pechmann, Sue Nava, Jim Taggart, and Mike Stickney for providing some of the seismic data used in this study. I appreciate the time taken by Regina Henrissey to locate many of the seismic stations with a portable GPS system. I thank Lila Pelot and Heather Redding for their help in obtaining some the published manuscripts cited in this study. The course of this study was greatly improved by guidance and helpful discussions with: Jim Zollweg, Dave Rodgers, Dick Smith, Bill Hackett, Jack Pelton, Mark Anders, Jim Pechmann, Tony Crone, Ron Bruhn, Ivan Wong, and Kathleen Haller. I thank Jim Zollweg, Dave Rodgers, Jack Pelton, Bill Hackett, and Dick Smith for their time and efforts reviewing this lengthy document.

ABSTRACT

Aftershock hypocenters of the 1984 Devil Canyon, Idaho earthquake indicate the sequence was associated with conjugate normal faulting on two northwest-striking normal faults that bound the Warm Spring Creek graben. The M_L 5.8 mainshock occurred on August 22, 1984 and is considered a late aftershock of the M_s 7.3 Borah Peak earthquake of October 28, 1983, which ruptured portions of the Lost River and Lone Pine faults. Focal mechanisms and the distribution of aftershock hypocenters suggest that the seismogenic part of the Challis segment of the Lost River fault has a planar geometry which strikes N 25° W and dips 75° SW, and the Lone Pine fault has a planar geometry which strikes N 39° W and dips 58° NE. Focal mechanisms indicate that the earthquakes on the Challis segment and Lone Pine fault were caused by predominantly normal faulting with minor components of left-lateral strike-slip. Their T-axes are consistent with the northeast-southwest extensional direction of the local Basin and Range province.

The mainshock nucleated at a depth of 12.8 $\pm$ 0.7 km on the Challis segment where the conjugate faults merge. The largest aftershock, M_L 5.0 on September 8, 1984, nucleated at a shallower depth of 7.1 $\pm$ 1.9 km on the Lone Pine fault. The Devil Canyon mainshock is interpreted to have ruptured unilaterally upward and to the northwest along the Challis segment of the Lost River fault system. Rupture dimensions inferred

from the aftershock distribution indicate the mainshock had a static stress drop of 14 bars. The largest aftershock may have ruptured upward and to the northwest along the Lone Pine fault. It is suggested that stress changes resulting from the rupture of the M_L 5.8 mainshock along the Challis segment increased shear stresses on the Lone Pine fault which was probably close to its yield stress. This increase caused the M_L 5.0 primary aftershock and most of its subsequent aftershocks to occur along the Lone Pine fault.

Characteristics of the conjugate normal faulting observed in the Devil Canyon sequence consist of normal faults that have their own orientations and sense of slip, but are mechanically coupled leading to a cause-and-effect relationship for contemporaneous slip along each fault. Similar characteristics are observed in other conjugate normal faulting sequences, as well as strike-slip and thrust conjugate faulting sequences worldwide. Comparison to these other conjugate faulting sequences suggests that the direction of rupture, location of the initiating earthquake, and the stress level on pre-existing faults may be important factors as to whether the conjugate fault becomes active.

TABLE OF CONTENTS

LIST OF TABLES

LIST OF FIGURES

LIST OF FIGURES (continued)

CHAPTER 1. INTRODUCTION

Conjugate normal faults are widely observed in the geologic record, but are not well understood. Improved capabilities of acquiring detailed earthquake data and the fortuitous occurrence of some conjugate fault sequences have made it possible to identify and study conjugate normal faults and other conjugate fault pairs. One question that has been raised is whether the conjugate faults move independently or simultaneously. On one hand, it does not seem geometrically possible that two conjugate faults can operate simultaneously because they would interfere where they cross each other (Freund, 1974), and in some examples, fault geometries do indicate that one fault consistently offsets the other (Horsfield, 1980). On the other hand, Horsfield (1980) has demonstrated through sand box experiments that conjugate normal fault pairs can operate contemporaneously by small scale faulting near their intersections. He further suggests that the same can happen in large-scale structures. Two recent earthquake sequences, the 1980 Irpinia, Italy and the 1982 North Yemen, Arabian Peninsula, provided seismological evidence that conjugate normal faults can move contemporaneously (Crosson et al., 1986; Langer et al., 1987).

The 1984 Devil Canyon earthquake sequence provides a rare opportunity to investigate conjugate normal faulting. Well-constrained hypocenters and focal mechanisms provide evidence for contemporaneous

activity along two northwest-striking conjugate normal faults. The 1984 Devil Canyon sequence is arguably the best seismological example of conjugate normal faulting observed to date. Characteristics of conjugate normal faulting observed in the Devil Canyon sequence have application to the tectonics of the Basin and Range and extensional settings worldwide.

The 1984 Devil Canyon earthquake sequence began on August 22, 1984 when a M_L 5.8 earthquake occurred south of Challis, Idaho, about ten months after the 1983 M_s 7.3 Borah Peak, Idaho earthquake (Figure 1). The Borah Peak mainshock was associated a maximum of 2.7 m of predominantly normal slip along the central segment of the Lost River fault (Crone et al., 1987). The 1984 Devil Canyon earthquake is considered an aftershock of the Borah Peak earthquake since it occurred along a northern segment of the Lost River fault and within a trend of aftershock epicenters that migrated northward beginning ten days after the Borah Peak mainshock (Zollweg and Richins, 1985). The 1984 sequence was named for Devil Canyon which is located near the epicenter of the M_L 5.8 event. The M_L 5.8 earthquake occurred on the Challis segment of the Lost River fault and its largest aftershock, M_L 5.0, occurred 17 days later on the Lone Pine fault (Figure 2).

In this study, the term "conjugate" refers to faults that occur in two intersecting sets and coordinated kinematically, with each set being distinctive in both orientation and sense of shear (Davis, 1984). Contemporaneous activity along the conjugate faults is defined as occurring within the time frame of the mainshock-aftershock sequence (three weeks for this sequence and generally less than one month in

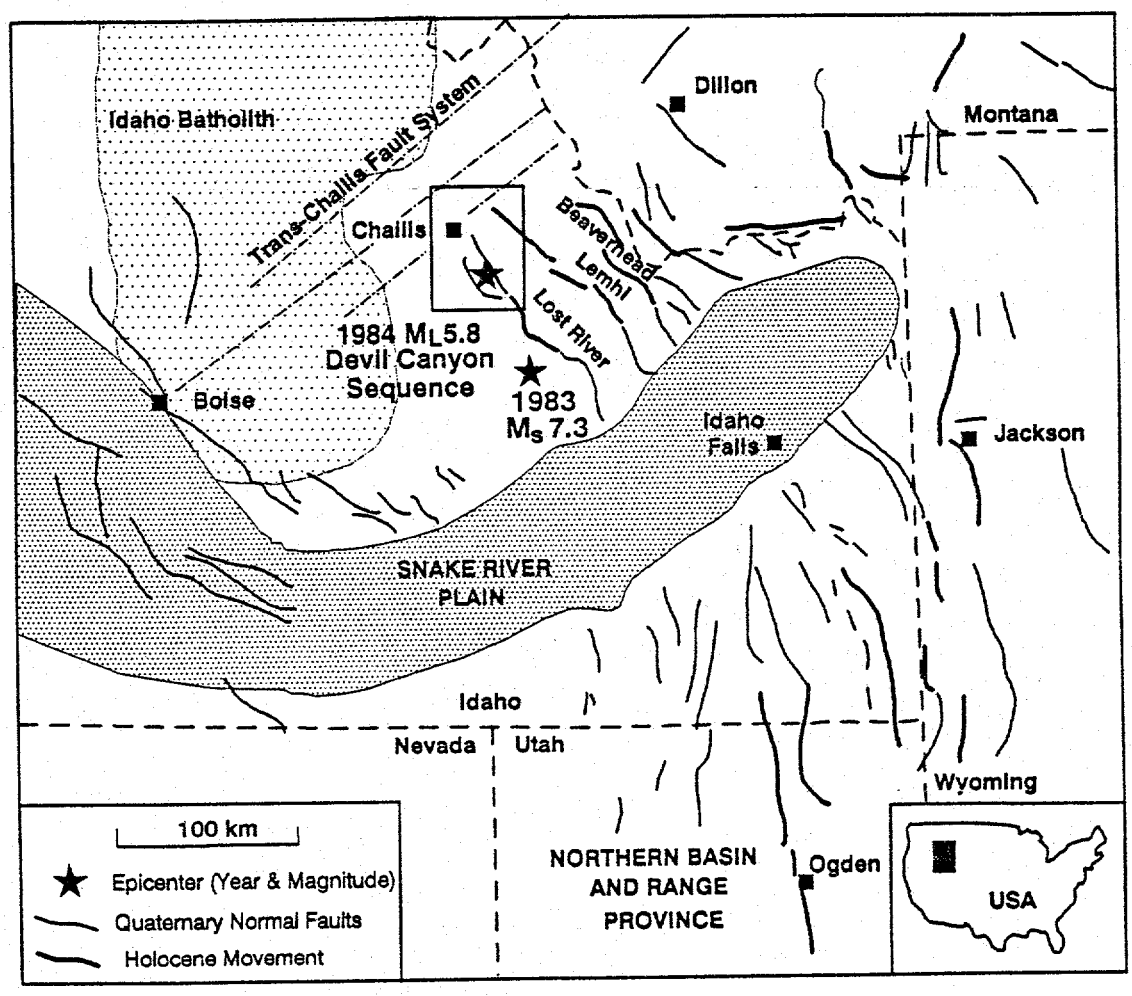

Figure 1. Tectonic setting and location of the study area for the 1984 Devil Canyon earthquake sequence. Faults from Anders et al. (1989).

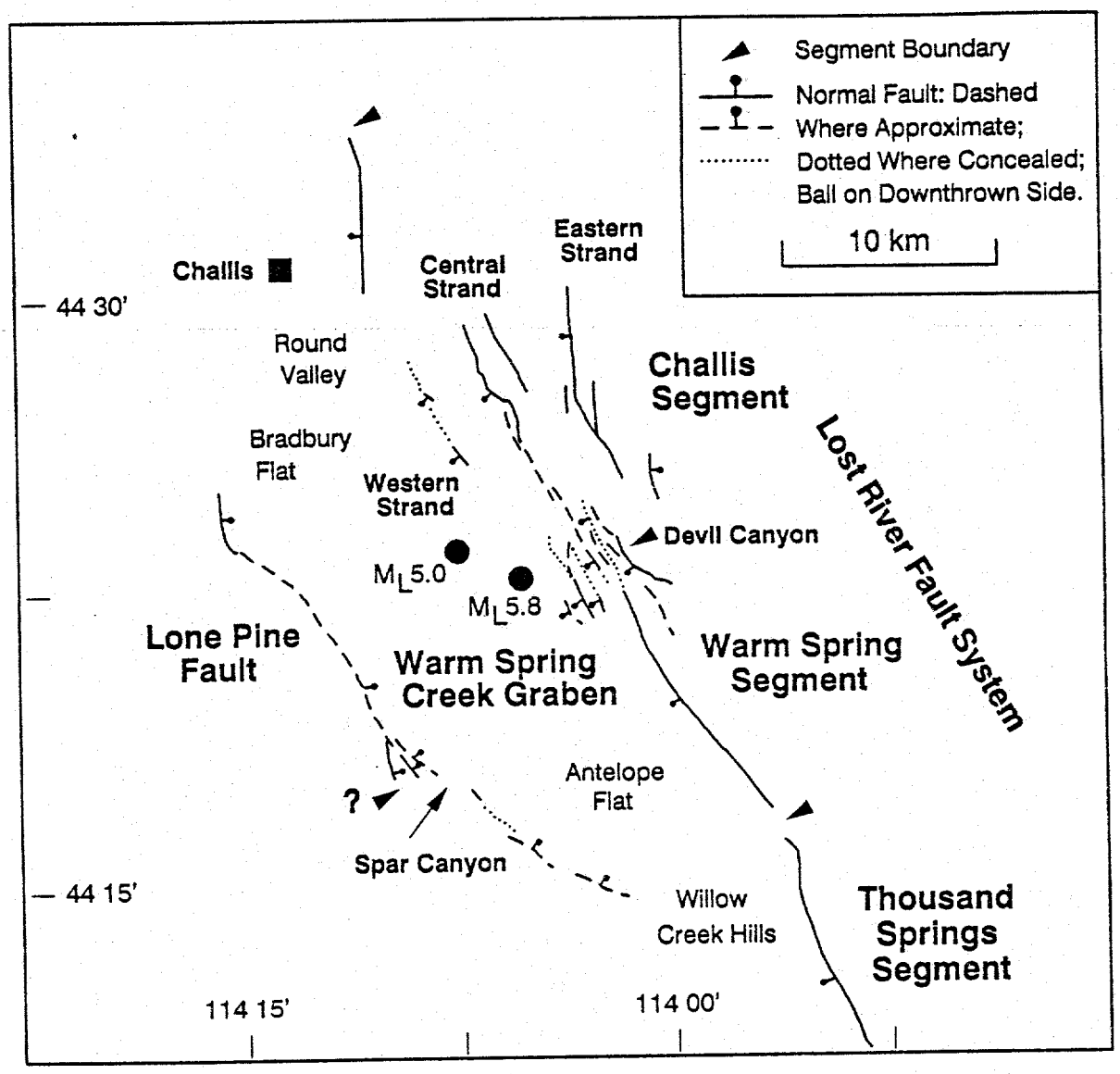

Figure 2. Locations of Quaternary normal faults and their proposed segment boundaries (Witkind, 1975; Rember and Bennett, 1979; Fisher et al., 1983; Hobbs et al., 1991; Crone and Haller, 1991; this study). Epicenters are shown for the August 22, 1984 M_L 5.8 (Zollweg and Richins, 1985) and September 8, 1984 M_L 5.0 earthquakes (this study).

other observed cases). Detailed recordings of microearthquakes from a dense array of temporary analog seismic stations are analyzed. The focal mechanisms and hypocenter spatial and temporal characteristics are combined with geological information to assess the style, geometry, timing, kinematics, and mechanics of conjugate normal faulting. The characteristics of conjugate normal faulting observed in the Devil Canyon sequence are compared to other conjugate normal faulting sequences, and strike-slip and thrust conjugate sequences worldwide.

CHAPTER 2. SEISMOTECTONIC SETTING

Tectonic and Geologic Framework

The 1984 Devil Canyon earthquake sequence occurred south of Challis, Idaho in the northern Basin and Range tectonic province, near the Idaho Batholith (Figure 1). The northern Basin and Range lies northwest of the eastern Snake River Plain, a northeast-trending Tertiary and Quaternary bimodal-volcanic track of the Yellowstone hotspot (Pierce and Morgan, 1992), and southeast of the trans-Challis fault system, a northeast-trending Eocene extensional feature (Bennett, 1986). Basin and Range extensional faulting began sometime between late Oligocene and mid-Miocene time, and has continued into the Holocene (Hait and Scott, 1978; Ruppel, 1982; Hobbs et al., 1991). Three major mountain ranges in this region include the northwest-trending Lost River, Lemhi, and Beaverhead mountains which extend about 140-150 km from the eastern Snake River Plain to the trans-Challis fault system. The ranges are bounded on their southwest flanks by major normal fault systems, resulting in a half-graben fault style (Figure 1).

The Devil Canyon epicentral area is situated within the Warm Spring Creek graben, which is bounded on the east side by northwest-striking segments of the Lost River fault and on the west side by the northwest-striking Lone Pine fault (Figure 2) (McIntyre et al., 1982; Hobbs et al., 1991). Uplifted blocks of Paleozoic sedimentary and

metamorphic rocks are exposed in the mountain ranges bounding the graben. Geologic cross-sections through the graben show a down-dropped block of Paleozoic basement rock overlain by Quaternary sedimentary and Tertiary volcanic rocks (Baldwin, 1951; Hobbs et al., 1991).

The northern portion of the Lost River fault consists of two fault segments, the Warm Spring and Challis segments (Scott et al., 1985). The Warm Spring segment extends from the Willow Creek Hills to Devil Canyon. This segment is characterized by a prominent range front, several steep fault scarps, and minor surface faulting along some Holocene scarps that occurred during the Borah Peak earthquake sequence (Crone and Haller, 1991). The 1983 surface faulting along this segment has been interpreted to be secondary in nature (Ward and Barrientos, 1986; Barrientos et al., 1987; Crone et al., 1987). Paleoseismic investigations along this segment suggest that prior to 1983 the most recent offset occurred 5500-6200 years ago (Schwartz and Crone, 1988).

Devil Canyon is located at the segment boundary between the Warm Springs and Challis segments. The segment boundary is interpreted from a 0.5 km left step in the Lost River fault, several subsidiary northwest-striking normal faults, and changes in the age of faulting and geomorphic expression of the Warm Spring and Challis segments (Hobbs et al., 1991; Crone and Haller, 1991).

The primary or central strand of the Challis segment strikes N 25° W from Devil Canyon to Challis, Idaho. Its faulting history is poorly known (Crone et al., 1987). Crone and Haller (1991) report that the fault scarp is subdued, suggesting a lower long-term slip rate. Reconnaissance studies by Scott et al. (1985) indicate very little

evidence for late Quaternary faulting. The geomorphic expression of the valley and range indicate the fault may separate into two diverging strands (central and western strands; Figure 2) (Crone and Haller, 1991). There may also be a third strand of the Challis segment located to the east which has an average strike of N 14° W (Figure 2) (Hobbs et al., 1991). No detailed information is currently available on the age of most recent offset or amount of displacement along the eastern strand. However, the fault displaces Eocene Challis volcanic rocks and is concealed beneath Quaternary landslide deposits (Hobbs et al., 1991).

The Lone Pine fault strikes approximately N 39° W from the Willow Creek Hills to Bradbury Flat, about 2 km south of the Salmon River (Figure 2) (Baldwin, 1951). Minor surface faulting associated with the Borah Peak earthquake was observed along the southern end of the Lone Pine fault near the Willow Creek Hills (Crone et al., 1987). Limited field reconnaissance indicates that there may be evidence of Holocene movement prior to 1983 (C. Waag, personal communication, 1993). Segmentation of this fault has not been investigated in detail, but a change in the strike of the Lone Pine fault north of Spar Canyon and the presence of several short northwest-striking subsidiary normal faults at Spar Canyon (Hobbs et al., 1991) suggest the presence of a segment boundary (Figure 2).

Contemporary Seismicity

The Devil Canyon sequence as discussed here began with a M_L 5.8 earthquake on August 22, 1984 at 09:46 UTC, ten months after the Borah Peak mainshock. The sequence occurred about 15 km north of the northern

terminus of immediate aftershock zone of the Borah Peak earthquake (Figure 3). The Devil Canyon mainshock was one of the three largest of the Borah Peak aftershocks, all of which had M_L 5.8.

Modeling of long-period body waves by Doser and Smith (1985) indicate that the rupture of the Borah Peak earthquake consisted of a single event which began at the southern end of the Thousand Springs segment and propagated unilaterally northwestward toward the surface. Richins et al. (1987) show that the majority of aftershock hypocenters, within a three-week time window, are located along the Thousand Springs segment (Figure 3). Hypocenters for these aftershocks define a northwest-striking normal fault dipping to the southwest along the Thousand Springs segment (Richins et al., 1987; Shemeta, 1989). Very few aftershocks were observed south of the mainshock epicenter along the Mackay segment (Richins et al., 1987). Susong et al. (1990) suggested that the intersection zone or segment boundary between the Mackay and Thousand Springs segments arrested the spread of rupture to the south along the Mackay segment either by rupture branching or interlocking of subsidiary faults (King, 1983; Bruhn et al., 1987, 1990), thus directing unilateral rupture to the northwest along the Thousand Springs segment. They also propose that the intersection zone was the site of the rupture nucleation for the Borah Peak mainshock. Based on the pattern of surface faulting in the Willow Creek Hills near the Thousand Springs segment and along the Warm Springs segment, fault rupture may have terminated at this location due to a barrier (Boatwright, 1985; Crone et al., 1987).

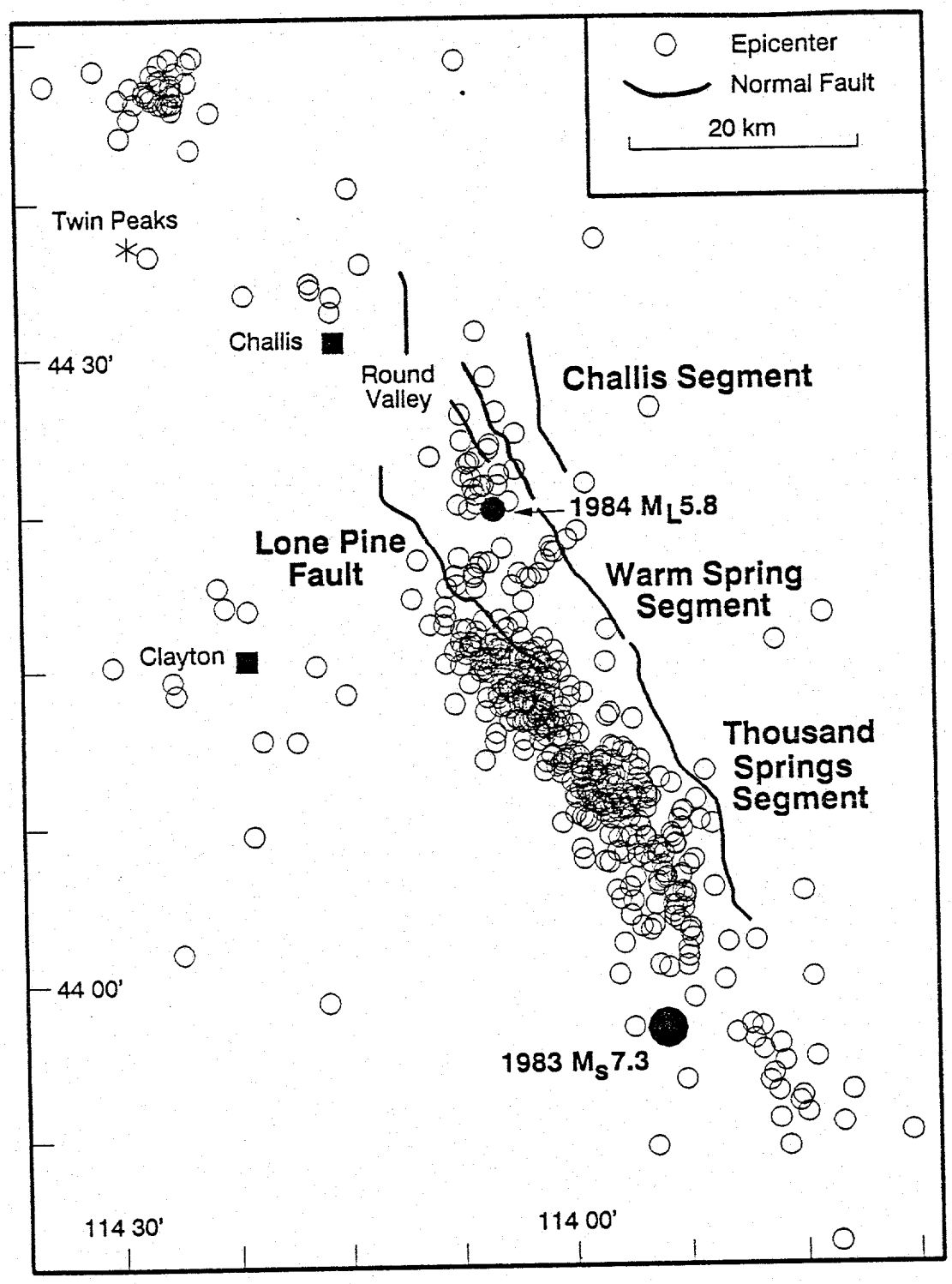

Figure 3. Epicenters for the 1983 M_s 7.3 Borah Peak, Idaho mainshock, its immediate aftershocks (October 29 to November 19, 1983; Richins et al., 1987), and later aftershocks ($M_L \geq 3.0$; November 19, 1983 to August 23, 1984; Zollweg and Richins, 1985).

Zollweg and Richins (1985) noted that aftershock epicenters migrated northwest along the Lost River fault from the immediate aftershock zone to the trans-Challis fault system near Twin Peaks beginning about ten days after the Borah Peak mainshock. They also showed a concentration of epicenters in the area of the Devil Canyon sequence prior to the M_L 5.8 on August 22, 1984 (Figure 3).

After the M_L 5.8 earthquake, aftershocks continued until at least late September, 1984. There were 50 aftershocks exceeding M_L 3.0, including five that exceeded M_L 4.0 and one that had M_L=5.0. Sixteen of these small to moderate size aftershocks are analyzed in this study, including the primary aftershock, M_L 5.0.

Regional Stress Field

Stress data indicate that the Basin and Range province northwest of the eastern Snake River Plain is characterized by an extensional stress field oriented northeast-southwest. Figure 4 shows a compilation of minimum principal stress orientations from: 1) Zoback and Zoback (1989) for the region; 2) Zollweg and Richins (1985) near Twin Peaks; 3) Stickney (1993) near the Beaverhead fault; and 4) Jackson et al. (1993) for the eastern Snake River Plain. The focal mechanism for the M_L 5.8 August 22, 1984 earthquake shows a T-axis consistent with the surrounding northeast-southwest extensional stress orientation (Zollweg and Richins, 1985).

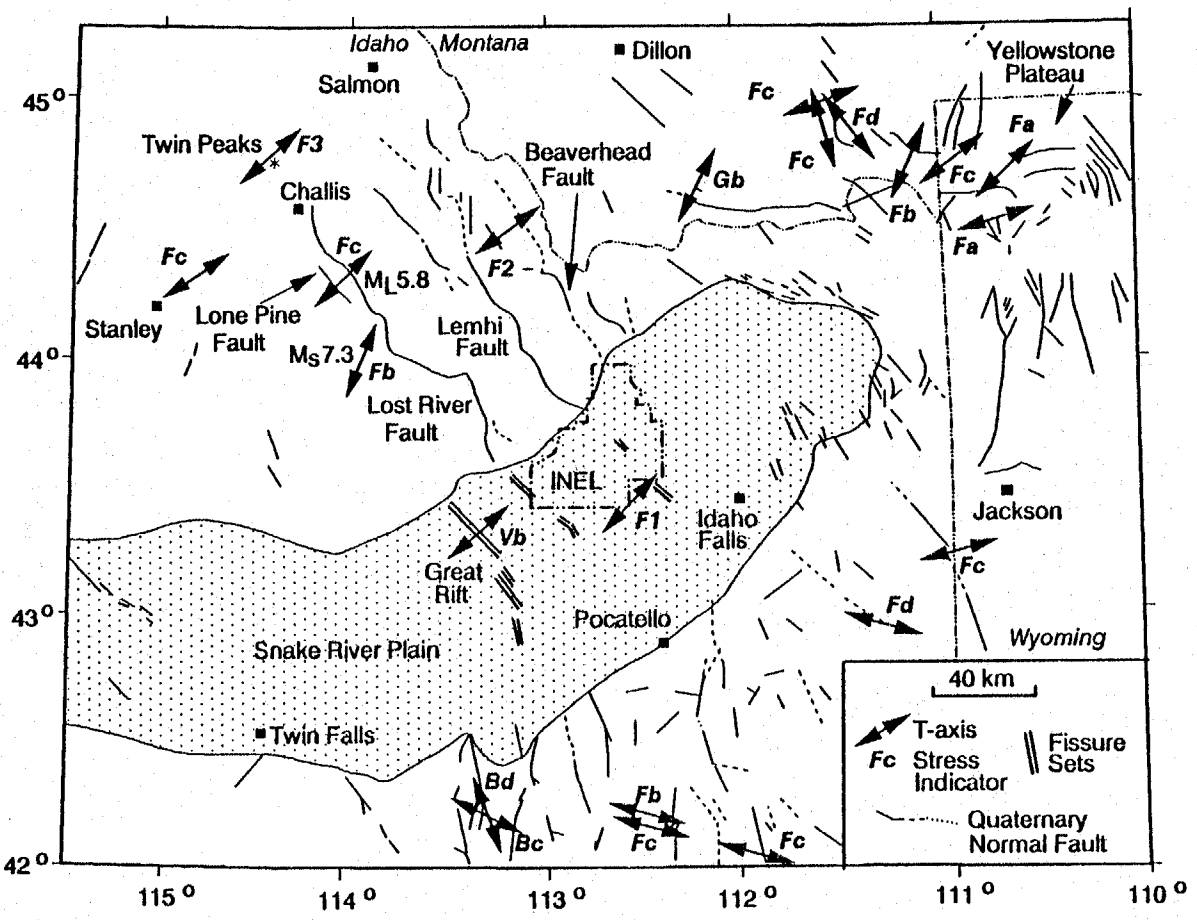

Figure 4. Distribution of minimum principal stress orientations from focal mechanisms (F), fault-slip data (G), alignment of volcanic rift zones (V), and borehole breakouts (B) as compiled by Zoback and Zoback (1989). Quality ranking (a, b, c, or d) as assessed by Zoback and Zoback (1989). Also included are T-axes from: *F1* - Jackson et al. (1993); *F2* - Stickney (1993); and *F3* - Zollweg and Richins (1985). M_L 5.8 indicates T-axis for Devil Canyon mainshock and M_s 7.3 indicates T-axis for 1983 Borah Peak earthquake. Figure modified from Jackson et al. (1993).

CHAPTER 3. DATA COLLECTION AND ANALYSES

Data Collection for the 1984 Microearthquake Survey

Within a day of the M_L 5.8 earthquake on August 22, 1984, the U. S. Geological Survey (USGS), University of Utah Seismograph Stations (UUSS) and Idaho National Engineering Laboratory (INEL) began installing twenty-three portable analog seismographs in and around the aftershock zone. The seismographs operated from August 23, 1984 to September 14, 1984. A total of thirty sites were occupied covering an area 40 x 60 km with an average station spacing of about 10 km and providing good azimuthal coverage (Figure 5). Up to twenty-two stations operated at one time and the closest stations were within 1-2 km of the epicentral area, providing good focal depth control. Table 1 lists the code, name, and location of each temporary station. Locations for the INEL, USGS, and one UUSS stations were determined using a Magellan NAV PRO 1000 portable global positioning system receiver. The remainder of the UUSS station locations were obtained from topographic maps. All GPS locations were reduced to the topographic map datum (1927 North American datum). Elevations were measured from the topographic maps.

The USGS and UUSS operated Sprengnether MEQ-800 portable seismographs and the INEL operated Teledyne Geotech Portacorders. The INEL and USGS used Mark Products model L4-C seismometers and the UUSS used Teledyne Geotech model S-13 and Kinemetrics Ranger seismometers.

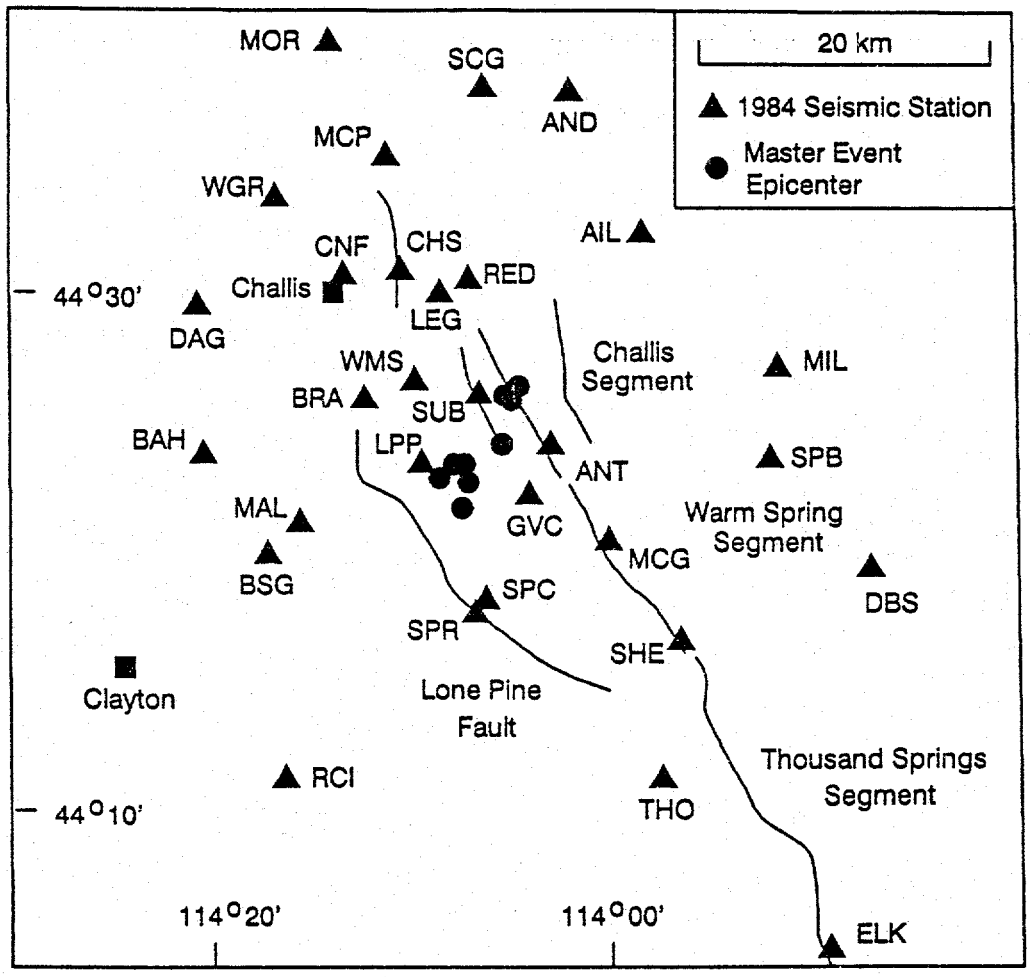

Figure 5. Location of temporary seismic stations for the 1984 Devil Canyon microearthquake survey. Also shown are the epicenters of the master events used to assess station delays.

TABLE 1.

Station locations for 1984 Devil Canyon microearthquake survey.

Code	Station Name	Location Latitude (deg-min)	Location Longitude (deg-min)	Elevation (m)
Idaho National Engineering Laboratory[a]				
SUB	Substation	44 26.457	114 6.347	1732
WMS	Warm Springs Ranch	44 26.773	114 9.630	1632
U.S. Geological Survey[a]				
AIL	Trail Creek	44 32.357	113 58.263	1682
AND	Anderson Spring	44 37.973	114 1.730	1564
ANT	Antelope Flat	44 24.157	114 3.330	1890
BRA	Bradbury Gulch	44 26.073	114 12.113	1600
CHS	Challis Hot Springs	44 31.390	114 10.313	1516
CNF	Challis National Forest	44 30.423	114 13.280	1574
DBS	Doublespring Creek	44 20.957	113 46.980	2012
ELK	Elkhorn Creek	44 4.457	113 49.297	2097
MAL	Malm Gulch	44 21.140	114 14.963	1670
MIL	Mill Creek	44 27.307	113 51.830	1841
MOR	Morgan Creek	44 39.857	114 13.897	1792
RED	Red Rocks	44 31.207	114 6.880	1878
SHE	Sheep Creek	44 16.773	113 56.947	2269
SPB	Sheep Pen Basin	44 23.723	113 50.997	2216
SPR	Spar Canyon	44 17.857	114 6.597	2012
WGR	Wine Glass Ranch	44 34.140	114 16.163	1713
University of Utah[b]				
BAH	Bayhorse	44 23.891	114 20.145	2073
BSG	Bradshaw Gulch	44 20.000	114 16.661	1634
DAG	Daugherty Gulch	44 29.738	114 20.256	2139
GVC	Grandview Canyon	44 22.256	114 3.642	1853
LEG	Leaton Gulch	44 30.270	114 8.273	1652
LPP	Lone Pine Peak	44 23.435	114 9.337	1757
MCP	McNabb's Point	44 35.433	114 10.932	1536
MCG	McGowan Creek	44 20.699	114 0.384	2152
RCI	Road Creek	44 11.367	114 16.115	1774
SCG	Shotgun Creek	44 38.186	114 6.195	1512
SPC	Spar Canyon	44 17.950	114 6.469	1999
THO	Thousand Springs[a]	44 11.190	113 57.280	2036

a - Locations measured with a portable global positioning system with an accuracy of ± 30 m. Locations are reduced to the topographic map datum by subtracting 15 m from the latitude, and 71 m from the longitude.
b - Locations measured from topographic maps have an estimated error of ± 30-60 m.

All of the portable seismographs operated at gains ranging from 72 to 96 dB with filters set at 0-10 or 5-10 Hz. The majority of seismographs produced two-day records, although a few generated one-day records. In both cases, drum rotation rates were 60 mm/min. Dates of the seismograms that were evaluated for each station in this study are listed in Appendix A.

Earthquake Analyses

P-Wave Arrival Times

P-wave arrival times and polarities of two-hundred-forty-eight aftershocks were measured from seismograms for the time period of August 27, 1984 to September 14, 1984. Arrival times were read to $\pm$ 0.02 s using an ocular. Station polarities were determined from comparing six Cyprus mine blasts, eight teleseisms, and several squat tests (see Appendix A). Before locations were determined, corrections were made to the P-wave arrival times to account for errors due to time drifts in the seismograph clocks. To minimize relative errors in the hypocentral locations, corrections were also applied to the arrival times to account for differences in elevations between the stations and imperfections in the velocity model.

Time Corrections

Time corrections were made by comparing portable WWV radio receivers to the internal clocks of the seismographs. WWV and internal-clock time codes were recorded simultaneously on the UUSS and INEL seismograms so that the internal clock error could be measured. The

UUSS and INEL set their seismograph clocks to lag behind WWV time by 2.0 to 4.0 s. The USGS used an oscilloscope to measure the difference between the WWV radio receiver and internal clock, and set the internal clocks to match WWV time; the observed time error was noted on the seismogram. Appendix A lists the time differences as measured from the INEL and UUSS seismograms. Time differences listed in Appendix A for USGS stations are opposite the time errors noted on their seismograms.

For each earthquake, Equation [1] was used to correct the observed P-wave arrival time using the time differences. Equation [1] is based on the assumption that the drift rate of the seismograph clock is linear between time comparisons.

$$T_p = T_{op} + [\frac{(T_{op}-T_1)}{T_2-T_1} \times (\Delta t_2 - \Delta t_1)] + \Delta t_1 \qquad [1]$$

where T_p is the corrected P-wave arrival time (s); T_{op} is the observed P-wave arrival time (s); Δt_1 and Δt_2 are the time differences (s) measured between WWV and seismograph clock at times T_1 and T_2, respectively (see Appendix A); and T_1 and T_2 are the times (s) when WWV and seismograph clock codes were compared. T_1 is the closest time of Δt_1 before and T_2 is the closest time of Δt_2 after T_{op}.

Time comparisons before or after observed P-wave arrival times were missing from several seismograms due to seismograph clock failures. Time corrections for these P-wave arrival times were estimated by using the average drift rate computed from the other time differences for that station. Because the drift rate for WMS was erratic, time corrections could not be estimated for P-wave arrival times from September 7, 1984

at 18:39 UTC through September 10, 1984 at 19:40 UTC. These P-wave arrival times were not included in the hypocenter determinations.

Velocity Model

Initially, the 1-D Borah Peak velocity models developed by Richins et al. (1987) and Shemeta (1989) were used to locate the Devil Canyon aftershocks (Figure 6). When compared to the Devil Canyon velocity model finally adopted, the Borah Peak velocity models resulted in larger RMS errors and caused P-wave arrivals that had the character of refracted waves to be modelled as direct waves. The latter problem had a major effect on the angle of incidence which caused difficulties in determining focal mechanisms. Thus, two complementary methods using blast and earthquake data were employed in an analysis to develop a better 1-D velocity model (see Appendix B for details). The overall low resolution of the seismic data only permitted evaluation of 1-D velocity models.

The Devil Canyon velocity model shown in Figure 6 was developed from this analysis. It has an intermediate layer of 5.9 km/s at depths of 8.5 to 11.0 km which is not present in the Borah Peak velocity models. This intermediate layer was required to provide a better fit to the earthquake data used in the analysis (Figures B-3 and B-4 in Appendix B). The Devil Canyon velocity model was chosen to locate the aftershocks because it: 1) resulted in lower RMS errors; 2) allowed P-wave arrivals had the character of refracted waves to be calculated as refracted waves on focal mechanisms; and 3) had the best fit to the earthquake data used in the velocity model analysis.

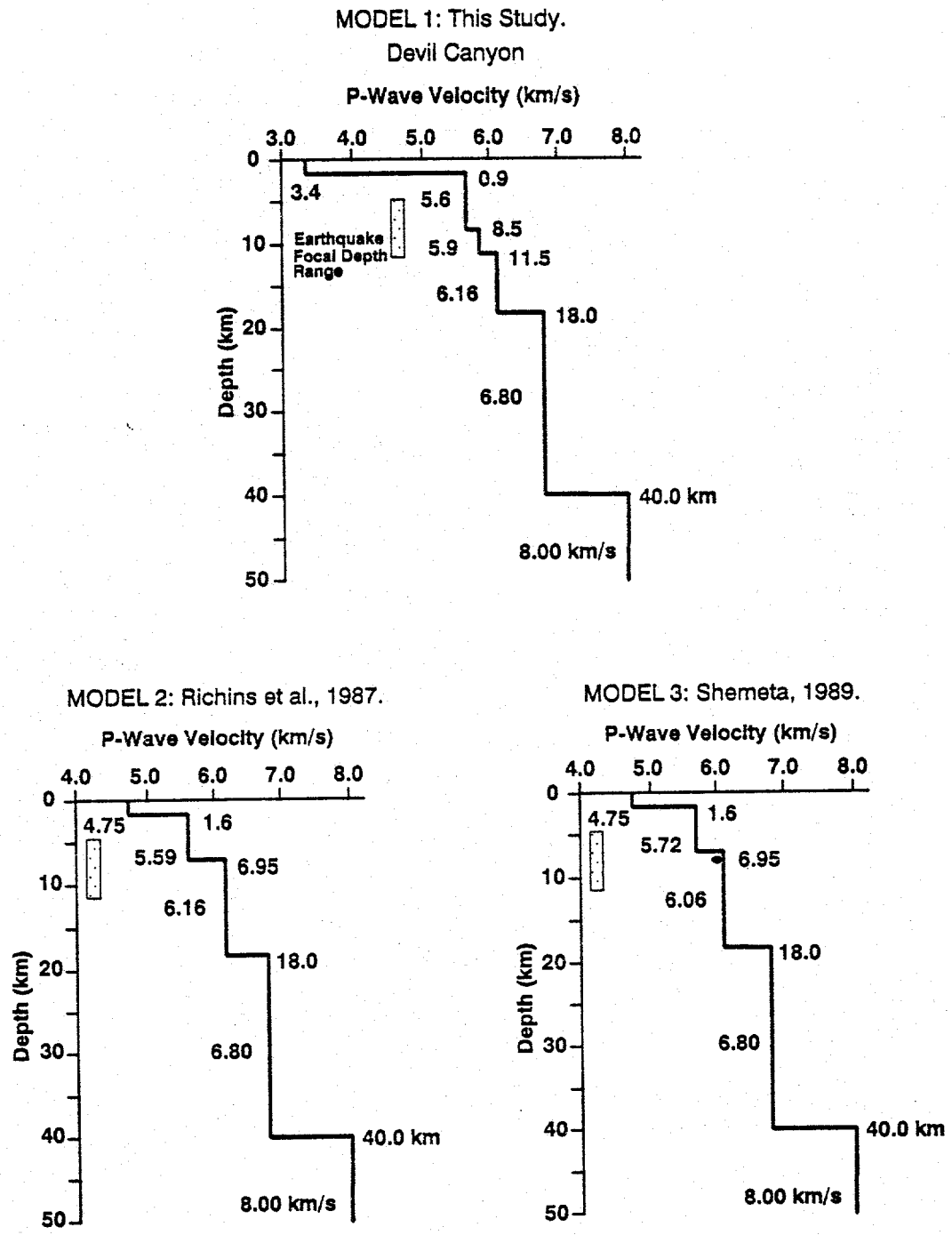

Figure 6. P-wave velocity profiles developed for 1) 1984 Devil Canyon earthquake sequence from this study; 2) 1983 Borah Peak aftershock study (Richins et al., 1987); and 3) investigation of digitally recorded 1983 Borah Peak aftershocks (Shemeta, 1989).

Elevation and Station Corrections

Stations were located at elevations ranging from 1512 to 2269 m. Since differences in elevations could amount to as much as 0.22 s difference in arrival times, elevation corrections were applied. The elevation corrections (see Appendix A) were computed using a near-surface velocity of 3.4 km/s and a datum elevation of 2000 m.

A master event technique similar to Corbett (1984) was used to determine station delays. In applying the master event technique, it was assumed that the calculated travel-time residuals are due to fixed station delays that cannot be accounted for in the velocity model. Near-station effects and inadequacies in the velocity model were reduced by using station delays estimated from the master events to locate all remaining earthquakes in the sequence. Thus, the remaining earthquakes have accurate relative hypocenters which provide a better representation of fault relationships associated with the earthquake sequence (Johnson and Hadley, 1976).

Nine earthquakes that were recorded by twenty-one or twenty-two stations were selected as master events to establish the station delays listed in Appendix A. Figure 5 shows the locations of the nine master events. All but three of the twenty-two stations were used to determine the master-event locations. WMS was not used since its clock drift was very erratic. LEG and SPC were not used since stations CHS and SPR were located within 3 km, respectively (Figure 5). CHS and SPR were chosen to determine the master-event locations since these station's were located with the portable GPS.

Nine master events were used to determine P-wave delays for twenty-two stations using the Devil Canyon velocity model. The resulting travel-time residuals were averaged for each station to determine the station delay (Appendix A). The epicenters and focal depths of the nine master events were also averaged, resulting in 44° 24.24′, 114° 6.37′, 7.58 km. This average location was used as the starting location in determining the station delays for the eight remaining stations. The initial set of station delays were subtracted from their respective P-wave arrival times of earthquakes selected to determine the travel-time residuals of the remaining stations. Travel-time residuals from a minimum of seven earthquakes were averaged to determine delays for the remaining stations, except for RED. Only four events could be used to establish the station delay for this station because of its short operating period.

Locations and Focal Mechanisms

The P-wave arrival times adjusted for clock, elevation, and station corrections were used in the HYPOINVERSE computer location program (Klein, 1989) with the Devil Canyon velocity model (Figure 6; Model 1) to determine the hypocenters and parameters for computing focal mechanisms. The average location for the nine master events was used as the starting location in the HYPOINVERSE program for all two-hundred-forty-eight earthquakes listed in Appendix C.

Clear, impulsive first motions of the best located earthquakes were used in the FPFIT computer program (Reasenberg and Oppenheimer, 1985) to determine focal mechanisms. Focal mechanisms were computed for

earthquakes having: 1) RMS $\leq$ 0.05 s; 2) gaps $\leq$ 70°; and 3) magnitudes (M_L) greater than 1.0. The earthquakes selected by these criteria occur at various depths and locations along the Challis segment and Lone Pine fault. Forty-seven focal mechanisms are shown in Appendix D. To test the effect of potential errors in the velocity model, focal mechanisms were computed for variations in the depth ($\pm$0.5 km) of the intermediate-layer (5.9 km/s) upper boundary of the Devil Canyon velocity model (Figure 6). Increasing the depth of the upper boundary appears to steepen the dips of the nodal planes for earthquakes below 8.5 km (see Appendix D).

Estimate of 1984 Mainshock Focal Depth

The depth phase pP interpreted on short-period vertical seismograms for three world-wide and Canadian standard seismograph stations was used to estimate the focal depth of the August 22, 1984 mainshock since regional seismographic stations recorded refracted waves as first arrivals. Seismograms from stations Lormes, France (LOR), Frobisher Bay, Canada (FRB), and Mould Bay, Canada (MBC) at distances between 30° and 80° have the best observed pP and P phases. Figure 7 shows the geometry of the pP- and P-wave travel paths at the hypocenter. The focal depth of the mainshock is estimated to be 12.8 $\pm$ 0.7 km based on pP-P arrival-time differences (Table 2) using Equation [2] (Bullen and Bolt, 1985):

$$h = \frac{\Delta T \, V_a}{2 \cos i_h} \qquad [2]$$

where h is the focal depth (km); ΔT is the time difference (s) between pP- and P-wave arrival times; V_a is the average velocity (km/s) between the earthquake hypocenter and earth's surface (5.3 km/s for the Devil Canyon velocity model, see Figure 6); and i_h is the angle of incidence (°) at the hypocenter given by Pho and Behe (1972).

The error for the mainshock focal depth is considered to be as large as 1 to 2 km. The error of 0.7 km is based only on reading errors estimated for the arrival times of the pP- and P-waves observed on the seismograms. This error does not account for inhomogeneous velocities, possible misidentification of sP as pP (no independent evidence for correct identification was obtained), and the limited number of observations used.

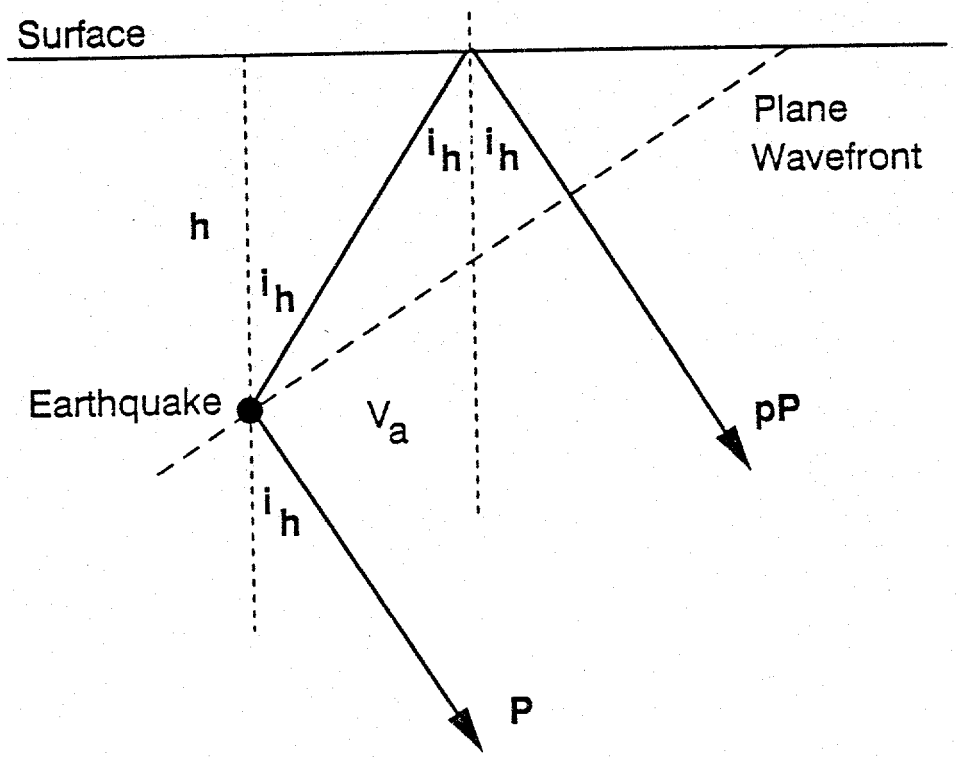

Figure 7. Geometry of pP and P depth phases at the hypocenter used to determine the focal depth (h) in Equation [2] (Bullen and Bolt, 1985).

TABLE 2.

Focal depth estimates for August 22, 1984 M_L 5.8 earthquake.

Code	Station Name	Distance[a] (°)	$T_{pP}-T_P$ (s)	i_h[b] (°)	Depth[c] (km)
LOR	Lormes, France	75	4.5±0.2	20.88	12.7
MBC	Mould Bay, Canada	32	4.2±0.2	32.33	13.2
FRB	Frobisher Bay, Canada	32	4.0±0.2	32.33	12.5
				Mean ±one-sigma[d]	12.8 ± 0.7

a - Based on travel time of P-waves estimated from mainshock origin time, 09:46 30.1 UTC (Zollweg and Richins, 1985) using "Table of P" in Herrin (1968).
b - Pho and Behe (1972).
c - See Equation [2] in text.
d - One-sigma includes reading errors.

CHAPTER 4. RESULTS

Two-hundred-forty-eight aftershocks were analyzed in this study and have ERH and ERZ values less than or equal to 0.7 and 1.7 km, resulting in errors of 950 m horizontally and 2300 m vertically, respectively, at the 95% confidence level (for the half-length of the long axis of the ellipse). Two-hundred-thirty-seven earthquakes are located in a cluster within the Warm Spring Creek graben, and ninety-five of these earthquakes have ERH and ERZ values less than or equal to 0.5 and 1.0 km, resulting in errors of 670 m horizontally and 1350 m vertically, respectively, at the 95% confidence level. All two-hundred-forty-eight earthquakes are used to evaluate the spatial and temporal patterns of the 1984 Devil Canyon earthquake sequence. The best located earthquakes (ERH $\leq$ 0.5 km and ERZ $\leq$ 1.0 km) and results of the focal mechanisms are used to resolve the fault orientations.

Spatial Patterns

The M_L 5.8 mainshock is located near Devil Canyon which is at the location of the segment boundary between the Challis and Warm Spring segments (Figure 8). Zollweg and Richins (1985) suggest that their epicenter for the mainshock is accurate to within 3 km. The largest or primary aftershock, M_L 5.0 on September 8, 1984 at 06:16 UTC, was located by the temporary network and has a horizontal error of 540 m and vertical error of 1890 m at the 95% confidence level. It is located

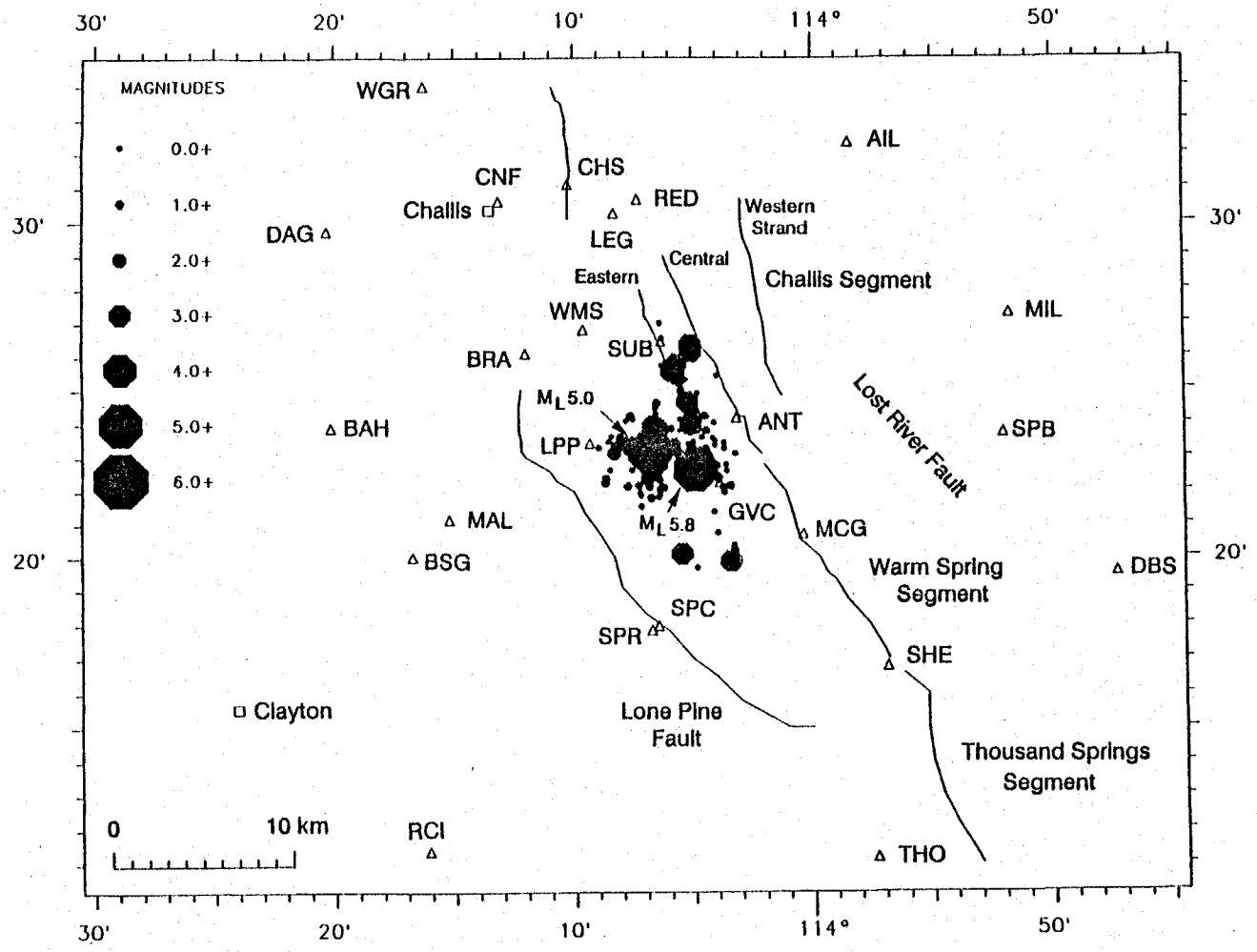

Figure 8. Epicenters (two-hundred-forty-eight) for the 1984 Devil Canyon earthquake sequence and locations of some 1984 temporary seismic stations. Maximum horizontal error for the epicenters is 950 m at the 95% confidence level. The mainshock epicenter is included in the for reference and has a horizontal error of 3 km (Zollweg and Richins, 1985).

2 km northwest of the mainshock, closer to the Lone Pine fault. Two-hundred-thirty-seven aftershocks that occurred from August 27 to September 14, 1984 are concentrated in a zone 15 km long and 8 km wide and centered within the Warm Spring Creek graben between the Challis segment and the northern portion of the Lone Pine fault. Epicenters in the northeastern part of the graben form a linear trend along the Challis segment. In the northwestern portion, near the epicenter of the primary aftershock, they form more of a cluster. Eleven aftershocks are located about 4-5 km south of the M_L 5.8 mainshock between the Warm Spring segment and southern portion of the Lone Pine fault. They form two small clusters (Figure 8).

Cross Sections of Hypocenters

Vertical cross sections through the two-hundred-forty-eight hypocenters plotted perpendicular and parallel to the strikes of the Lost River and Lone Pine faults show that focal depths range from 2.5 to 11.5 km with the majority occurring between 5 and 10 km (Figures 9-13). The hypocenters form two distinct patterns: 1) a linear trend along a structure that dips to the southwest and aligns with the surface location of one or more of the Challis segment fault strands; and 2) a linear trend along a structure that dips to the northeast and aligns with the surface location of the Lone Pine fault (Figure 10). The hypocenters outlining the two faults merge at a depth range of 9 to 11 km, depending the orientation of the cross section. Based on the location of Zollweg and Richins (1985) and the focal depth of 12.8 $\pm$ 0.7 km calculated in this study, the M_L 5.8 hypocenter is located at a depth

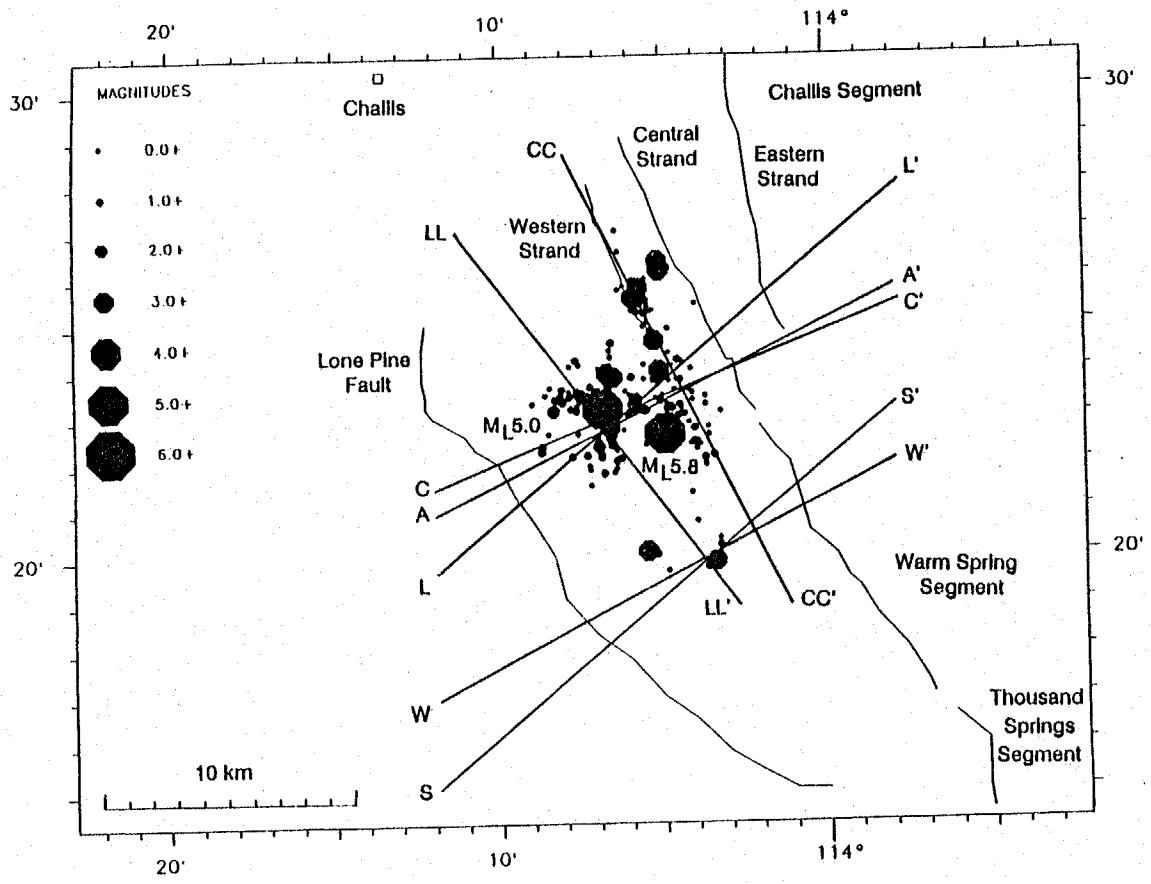

Figure 9. Map of two-hundred-forty-eight epicenters for the 1984 Devil Canyon earthquake sequence showing the locations of the cross sections for Figures 10-16. A-A′ is oblique to the faults; C-C′ is perpendicular to the central strand of the Challis segment; L-L′ is perpendicular to the northern portion of the Lone Pine fault; S-S′ is perpendicular to the southern portion of the Lone Pine fault; W-W′ is perpendicular to the Warm Springs segment; LL-LL′ is parallel to the Lone Pine fault; and CC-CC′ is parallel to the Lost River fault.

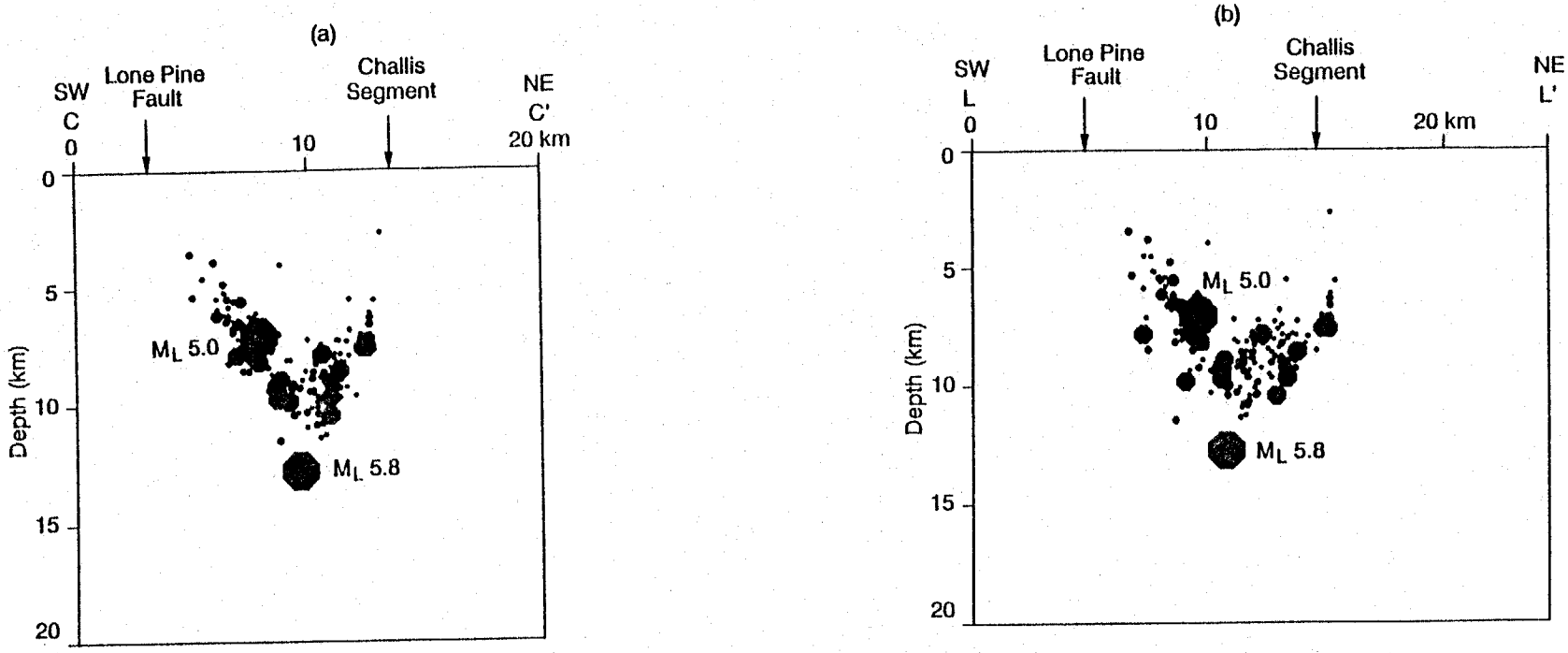

Figure 10. Cross sections through two-hundred-forty-eight hypocenters oriented perpendicular to the: a) Challis fault segment; and b) Lone Pine fault. Maximum errors of the aftershocks are 950 m horizontally and 2970 m vertically at the 95% confidence level. The mainshock hypocenter is included in the depth sections for reference, and has a horizontal error of 3 km (Zollweg and Richins, 1985) and vertical error of 700 m (this study). See Figure 9 for locations of cross sections and magnitude scale.

where the two structures merge. The hypocenter for the M_L 5.0 primary aftershock is located at 7.1 ± 1.9 km on the northeast dipping structure associated with the Lone Pine fault.

Depth profiles oriented along strike of the Lost River and Lone Pine faults are shown in Figure 11 (a) and (b), respectively. Hypocenters of one-hundred-eighteen aftershocks extend over a length of 15 km along the Lost River fault (Figure 11 a). The hypocenter for the M_L 5.8 mainshock is located near the boundary between the Challis and Warm Spring segments. The majority of aftershocks (one-hundred-eleven) extend over a length of 11 km to the northwest of the mainshock. Seven hypocenters are located to the southeast along the Warm Spring segment. Focal depths are as deep as 11.5 km at the southeast end and 8.5 km at the northwest end of the fault, indicating a shallowing of maximum focal depths to the northwest. The hypocenters (one-hundred-twenty-six) northwest of the mainshock along the Lone Pine fault (Figure 11 b) extend over a distance of 5 km and range in depth from 3.5 to 11 km. The M_L 5.0 hypocenter is located in the center of this cluster. Four hypocenters are located southeast of this cluster along the southern portion of the Lone Pine fault.

Since the majority of aftershocks occur within two distinct areas, the hypocenters are separated into two groups; the events (two-hundred-thirty-seven) located between the Challis segment and the northern portion of the Lone Pine fault, and the events (eleven) between the Warm Spring segment and southern portion of the Lone Pine fault. Cross sections of the two-hundred-thirty-seven hypocenters in Figure 12 (a) show very few earthquakes within the interior between the two faults

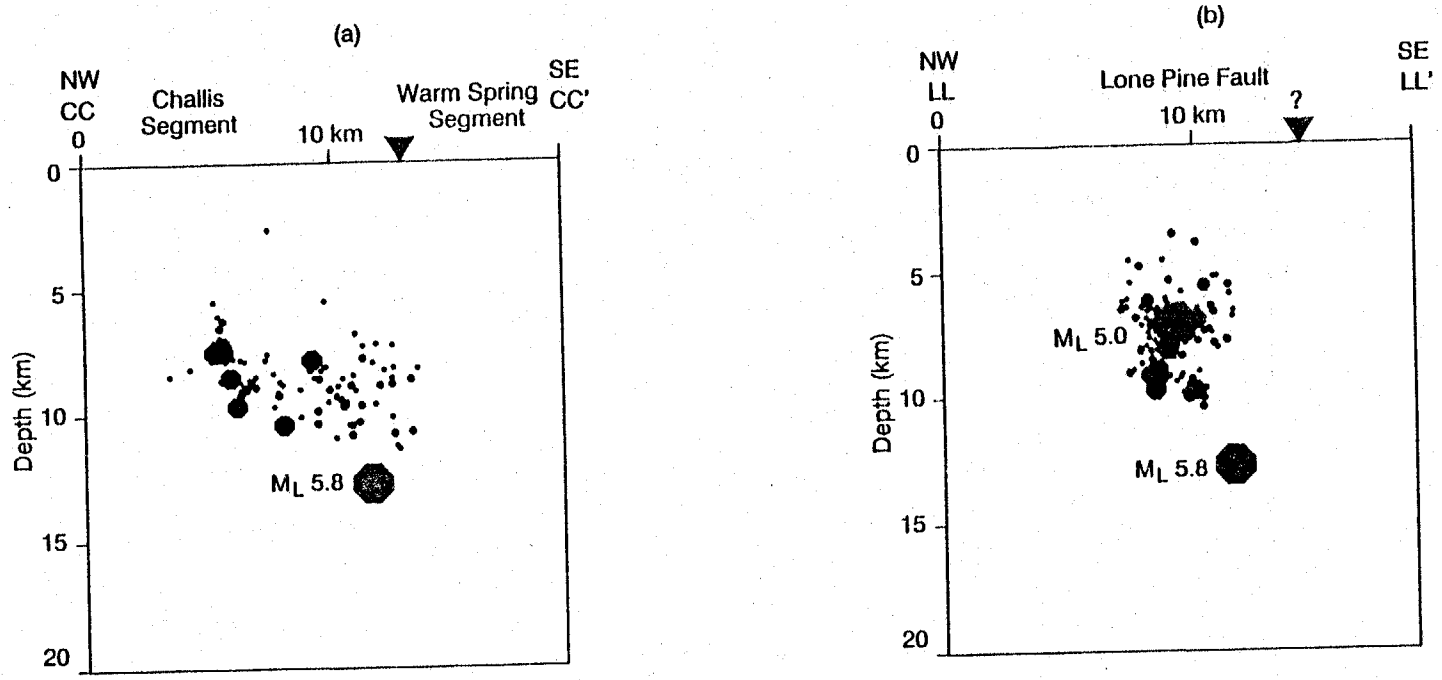

Figure 11. Cross sections through: a) one-hundred-eighteen hypocenters oriented parallel to the Lost River fault; and b) one-hundred-thirteen hypocenters parallel to the Lone Pine fault. Maximum errors of the hypocenters are 950 m horizontally and 2300 m vertically at the 95% confidence level. The M_L 5.0 aftershock has a horizontal error of 540 m and vertical error of 1890 m at the 95% confidence level. The mainshock hypocenter is included in the depth sections for reference and has a horizontal error of 3 km (Zollweg and Richins, 1985) and vertical error of 700 m (this study). See Figure 9 for locations of cross sections and magnitude scale.

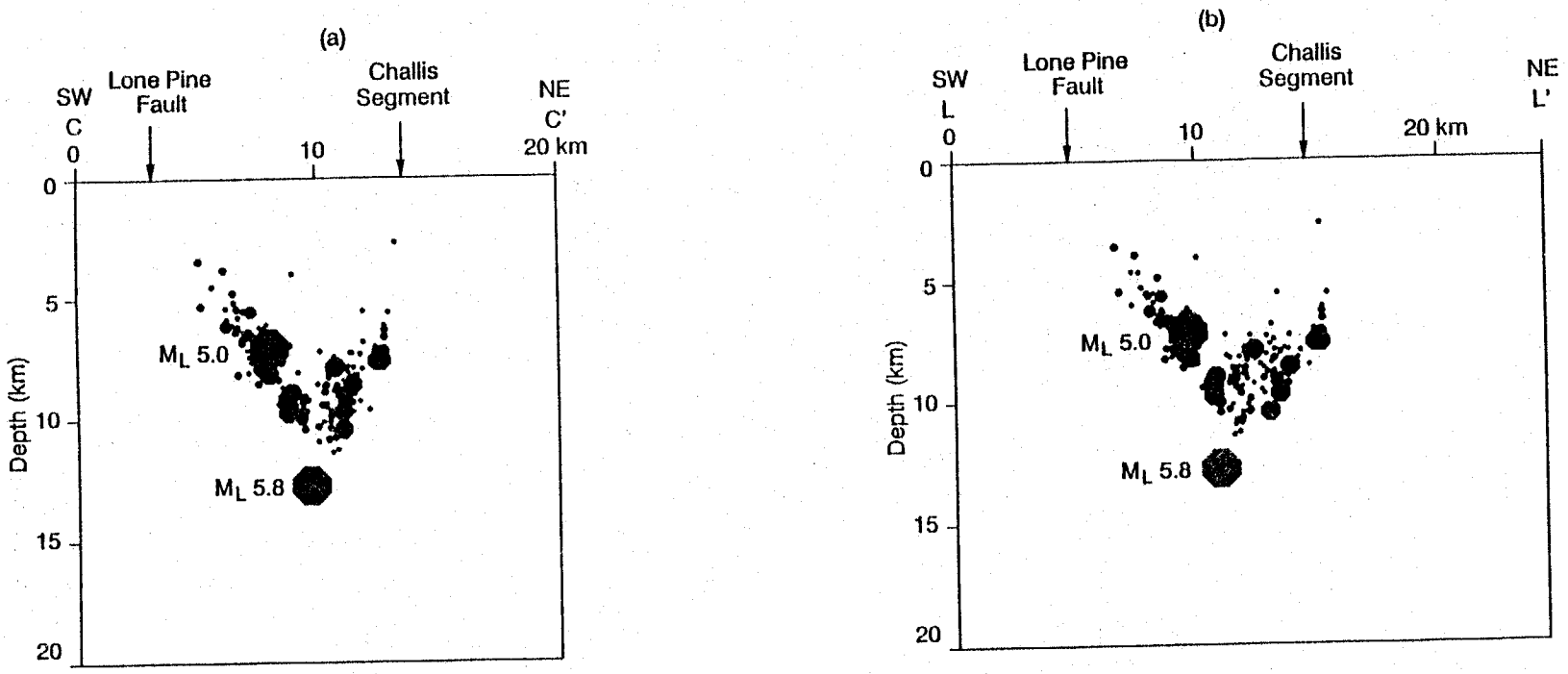

Figure 12. Cross sections through two-hundred-thirty-seven hypocenters oriented perpendicular to the: a) Challis fault segment; and b) Lone Pine fault. Maximum errors of the hypocenters are 950 m horizontally and 2300 m vertically at the 95% confidence level. The M_L 5.0 aftershock has a horizontal error of 540 m and vertical error of 1890 m at the 95% confidence level. The mainshock hypocenter is included in the depth sections for reference and has a horizontal error of 3 km (Zollweg and Richins, 1985) and vertical error of 700 m (this study). See Figure 9 for locations of cross sections and magnitude scale.

whereas in Figure 12 (b) the hypocenters are more scattered about the southwest dipping fault. The cross section in Figure 12 (a) shows that the hypocenters cluster more tightly along the northeast dipping fault. The cross sections in Figure 13 for the eleven hypocenters show two clusters of events that are 7 to 11.5 km deep. The cross sections in Figure 10 show that the seven events within the northeast cluster are located on the Lost River fault and the four events within the southwest cluster are located on the Lone Pine fault. Possibly, the northeast cluster forms a linear trend that has an apparent dip of 73° SW and aligns with the surface location of the Warm Spring segment (Figure 13 a). The southwest cluster may form a linear trend that has an apparent dip of 65° NE and aligns with the surface trace of the southern portion of the Lone Pine fault (Figure 13 b). In summary, the cross sections in Figures 10-13 show two oppositely dipping fault zones were active during the 1984 Devil Canyon sequence.

Temporal Patterns

Observations from the seismograms indicate that the rates of earthquake activity varied with time in three distinct periods: 1) August 27 to September 3; 2) September 4 to 7; and 3) September 8 to 14, 1984. Maps of the epicenters and perpendicular and parallel cross sections through the hypocenters for the three time periods (248 events total) are shown in Figures 14, 15, and 16, respectively. From August 27 to September 3, 1984, the majority of hypocenters are located along the Challis and Warm Spring segments, and cluster about the southwest dipping fault at depths of 7 to 11.5 km (Figure 14 b, c, and d). A

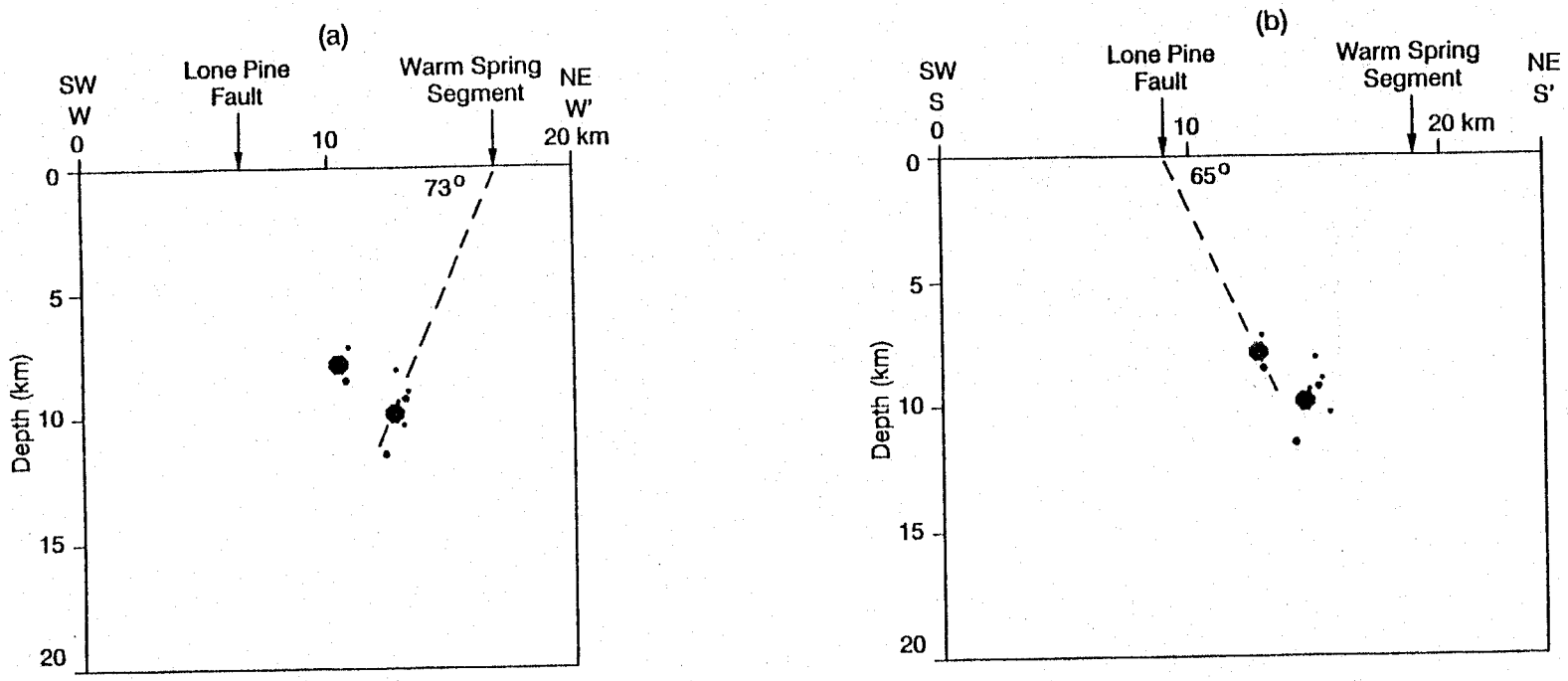

Figure 13. Cross sections through eleven hypocenters oriented perpendicular to the: a) Warm Spring fault segment; and b) southern portion of the Lone Pine fault. Dashed lines indicate possible fault orientations. Maximum errors of the hypocenters are 950 m horizontally and 2970 m vertically at the 95% confidence level. See Figure 9 for locations of cross sections and magnitude scale.

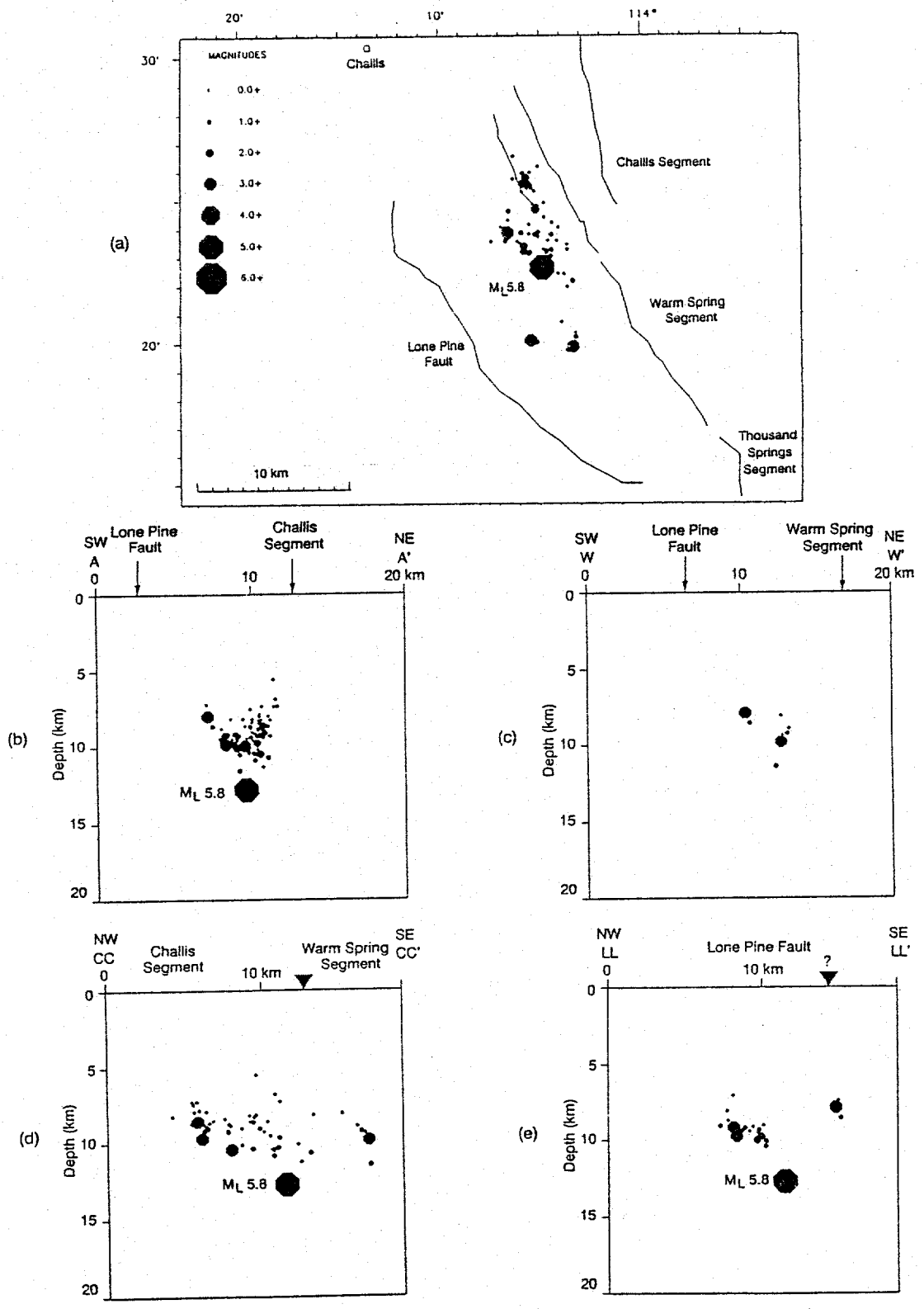

Figure 14. August 27 to September 3, 1984 hypocenters. In (d) and (e), the hypocenter for the August 22, 1984 M_L 5.8 is plotted for reference (epicenter from Zollweg and Richins, 1985; depth based on this study). Inverted triangles indicate segment boundaries (Crone and Haller, 1991; this study). See Figure 9 for locations of cross sections.

smaller number of hypocenters cluster about the northeast dipping fault at depths of 7 to 10 km (Figure 14 b and c). The majority of activity during this time period occurred along the Challis segment and northern portion of the Lone Pine fault northwest of the M_L 5.8 hypocenter (Figure 14 d and e), near the depths where the two faults merge (Figure 14 b). During this time period, nine of the eleven southern events occurred along the Warm Spring segment and southern portion of the Lone Pine fault (Figure 14 c, d, and e).

Aftershock activity suddenly increased around 21:00 UTC on September 3, 1984. The map and cross sections in Figure 15 show that earthquakes from September 4-7, 1984 were distributed along both faults northwest of the M_L 5.8 hypocenter. Hypocenters range from 6 to 11.5 km for both faults, even though they cluster about the southwest-dipping fault along the Challis segment (Figure 15 b), particularly at the northwestern end of the segment where two aftershocks of M_L 3.7 and 3.1 occurred within 7 minutes of each other (September 4, 05:50 and 05:57 UTC; Appendix C) (Figure 15 a). Only two of the eleven southern events were located south of the primary activity along the Warm Spring segment. A slight migration of hypocenters to shallow depths along both faults and to the west is apparent on the map and cross-section in Figure 15 (a and b, respectively).

Following the M_L 5.0 on September 8, 1984 at 06:16 UTC, aftershock activity increased dramatically. The map and cross sections in Figure 16 show all but a few hypocenters are clustered about the northeast-dipping fault at depths of 3 to 10 km. The map view in Figure 16 (a)

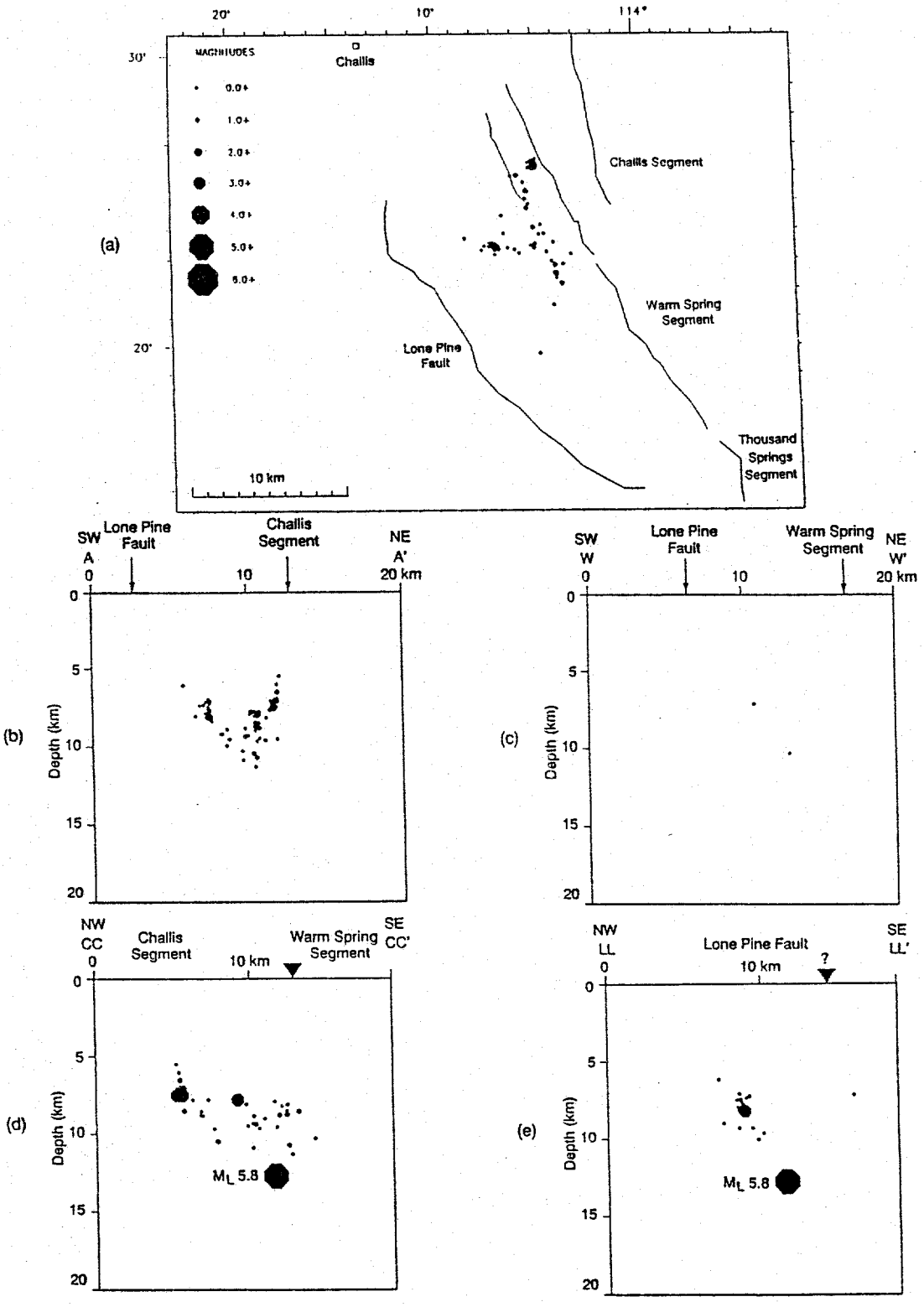

Figure 15. September 4 to September 7, 1984 hypocenters. In (d) and (e), the hypocenter for the August 22, 1984 M_L 5.8 is plotted for reference (epicenter from Zollweg and Richins, 1985; depth based on this study). Inverted triangles indicate segment boundaries (Crone and Haller, 1991; this study). See Figure 9 for locations of cross sections.

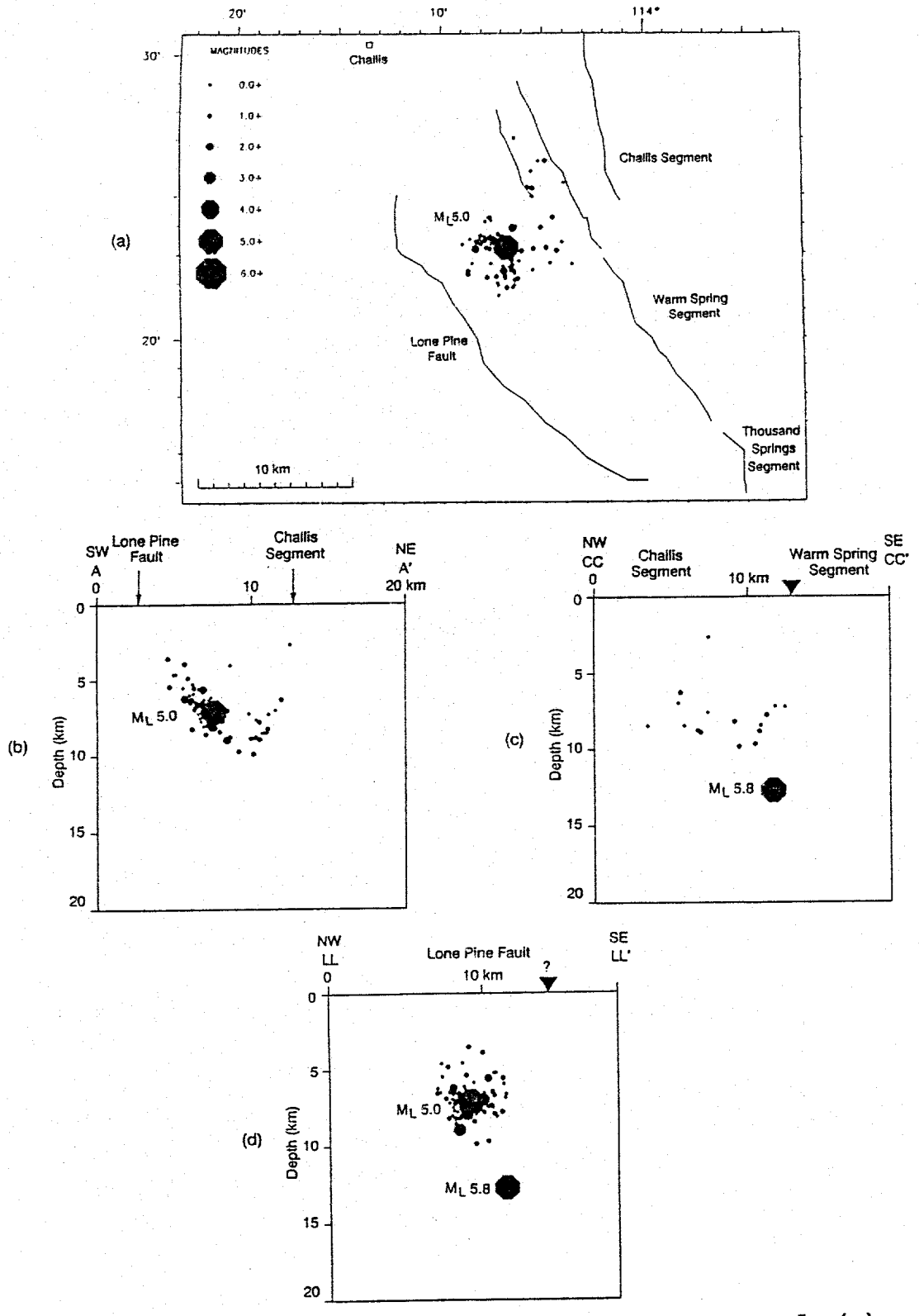

Figure 16. September 8 to September 14, 1984 hypocenters. In (c) and (d), the hypocenter for the August 22, 1984 M_L 5.8 is plotted for reference (epicenter from Zollweg and Richins, 1985; depth based on this study). Inverted triangles indicate segment boundaries (Crone and Haller, 1991; this study). See Figure 9 for locations of cross sections.

shows the activity forms a cluster further to the west than in Figure 15 (a). The hypocenters located on the southwest-dipping fault are at depths of 6.5 to 10 km (Figure 16 b). As during the previous time periods, the majority of activity occurred northwest of the M_L 5.8 hypocenter on both faults. During this time period, no events were located south of the primary activity along the Warm Spring segment (Figure 16 c and d).

Overall throughout the three time periods, the activity along the southwest-dipping fault associated with the Challis segment appeared to be concentrated at a depth range of 6 to 11.5 km and along an 11 km length of the fault northwest of the M_L 5.8 hypocenter. Most of the activity along the Challis segment occurred from August 27 to September 7, 1984, prior to the M_L 5.0 although several hypocenters are located along the Challis segment following the M_L 5.0 (Figures 14 d, 15 d, and 16 c). In contrast, fewer earthquakes occurred on the northeast-dipping structure associated with the Lone Pine fault before the occurrence of the M_L 5.0 on September 8, 1984 (Figure 14 e, 15 e, and 16 d). Prior to the M_L 5.0 event, activity was observed in the region to the south along the Warm Spring segment. The activity that followed the M_L 5.0 event occurred primarily on the Lone Pine fault to the northwest of the M_L 5.8 hypocenter. During the three time periods, there was a slight migration of hypocenters along both structures from deeper to shallower depths (Figures 14 b, 15 b, and 16 b).

Focal Mechanisms

Forty-three focal mechanisms of aftershocks having RMS $\leq$ 0.05 s, gaps $\leq$ 70°, and $M_L \geq 1.0$ were computed. Fifteen of these were associated with the southwest-dipping fault and twenty-eight with the northeast-dipping fault. Four focal mechanisms having RMS $\leq$ 0.09 s, gaps $\leq$ 105°, and $M_L \geq 1.0$ were computed for the eleven southern events located along the Warm Spring segment. Figure 17 shows the locations of nine focal mechanisms representing the aftershocks associated with the southwest-dipping Challis and Warm Spring fault segments, and the focal mechanism for the mainshock on August 22, 1984 (Zollweg and Richins, 1985). The focal mechanism for September 4, 1984 at 05:50 UTC is representative of eight similar focal mechanisms for the northwestern area (see Appendix D). Taking into consideration these nine focal mechanisms and the ones shown in Figure 17, the aftershocks along the Challis segment show predominantly normal faulting with a small component of left-lateral strike-slip, similar to the mainshock. Two of the mechanisms show a combination of reverse and left-lateral strike-slip faulting. Excluding the reverse mechanisms (840829 15:09 UTC and 840901 14:11 UTC in Figure 17), Table 3 shows the average orientation of the preferred nodal plane associated with the aftershocks along the Challis fault strike N 22$\pm$20° W and dip 50$\pm$20° SW. The aftershock focal mechanisms have an average strike and dip similar to the mainshock (Table 3). The T-axes orientations range from WNW-ESE to NNE-SSW, with most oriented similar to the northeast-southwest direction of the mainshock. The average orientation and plunge of the T-axes are N 41$\pm$21° E and 5$\pm$5°, respectively.

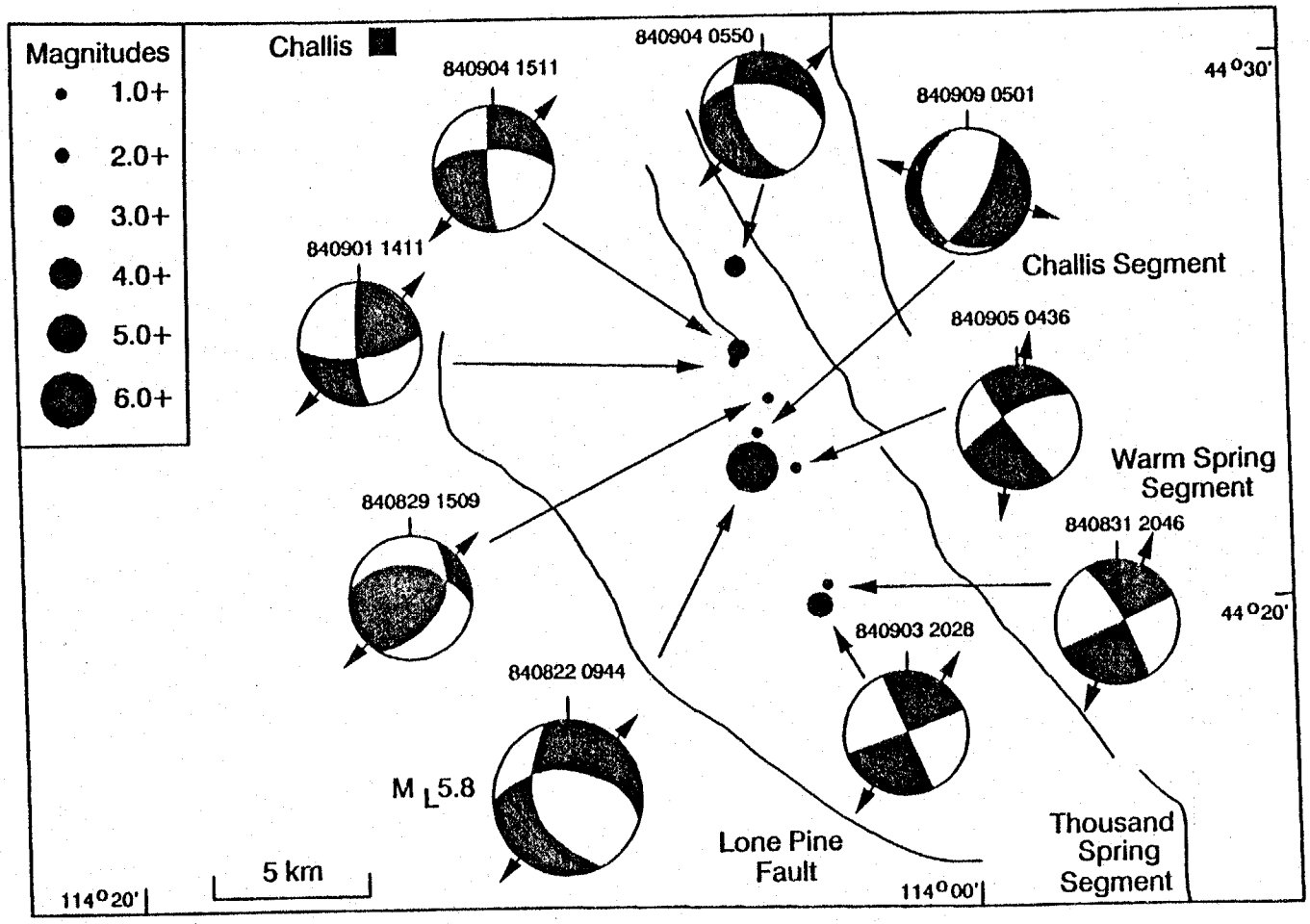

Figure 17. Lower hemisphere focal mechanisms for aftershocks ($M_L \geq 1.0$) along the Challis segment. The focal mechanism 840904 0550 is representative of eight similar focal mechanisms for the northwestern area (see Appendix D). Focal mechanism for the M_L 5.8 earthquake was obtained from Zollweg and Richins (1985). Compressional quadrants are shaded. Orientations of the T-axes are indicated by short arrows extended from the focal spheres. Numbers indicate the date (year, month, and day) and time (hour and minute) in UTC.

TABLE 3.

Results of the 1984 Devil Canyon earthquake focal mechanisms

Earthquake or Fault	Fault Plane Strike (°)	Fault Plane Dip (°)	T-Axis Azimuth (°)	T-Axis Plunge (°)
Mainshock M_L 5.8[a]	N 27 W	50 SW	N 36 E	7
Challis Segment[b]	N 22±20 W	50±20 SW	N 41±21 E	5±5
Aftershock M_L 5.0	N 5 W	40 NE	N 49 E	2
Lone Pine Fault[c]	N 47±32 W	46±22 NE	N 35±19 E	7±6
Warm Spring Segment[d]	N 20-25 W	80-90 SW	N 18-26 E	0-4
Southern Portion Lone Pine Fault[d]	N 62 W	55-58 NE	N 3-4 E	10

a - Zollweg and Richins, 1985.
b - Average and standard deviation of thirteen aftershocks associated with the Challis fault.
c - Average and standard deviation of twenty-seven aftershocks associated with the Lone Pine fault.
d - Values for two focal mechanisms unless they are the same.

The focal mechanisms associated with aftershocks along the northeast dipping Lone Pine fault are shown in Figure 18. The focal mechanism shown for September 9, 1984 at 07:07 UTC is representative of fourteen similar focal mechanisms, and the one for September 9, 1984 at 12:44 UTC is representative of five similar focal mechanisms (see Appendix D). The largest aftershock, M_L 5.0, on September 8, 1984 at 06:16 UTC and the majority of aftershocks northwest of its epicenter indicate predominantly normal faulting with a small component of left-lateral strike-slip (Figure 18). The average orientations of fault planes and T-axes determined from the twenty-seven focal mechanisms and the largest aftershock are shown in Table 3. The strike of the fault plane associated with the largest aftershock is oriented N 5° W, where the average of all aftershocks strikes N 47±32° W. The fault plane dip of the largest aftershock (40° NE) is similar to the average fault plane dip of all the aftershocks (46±22° NE). The T-axes for aftershocks associated with the northeast dipping fault are predominantly oriented northeast-southwest, with a few oriented ENE-WSW. Table 3 shows that the primary aftershock has a T-axis that trends N 49° E and plunges 2°, similar to the average T-axes trend, N 35±19° E, and plunge, 7±6°, of all the aftershocks.

Two focal mechanisms along the Warm Spring segment show left-lateral strike-slip mechanisms with near vertical dipping nodal planes striking N 20-25° W (Figure 17). Their T-axes are oriented N 18-26° W consistent with those for the Challis segment (Table 3). The two focal mechanisms associated with the southern portion of the Lone Pine fault have nodal planes striking N 62° W and dipping 55-58° NE (Figure 18).

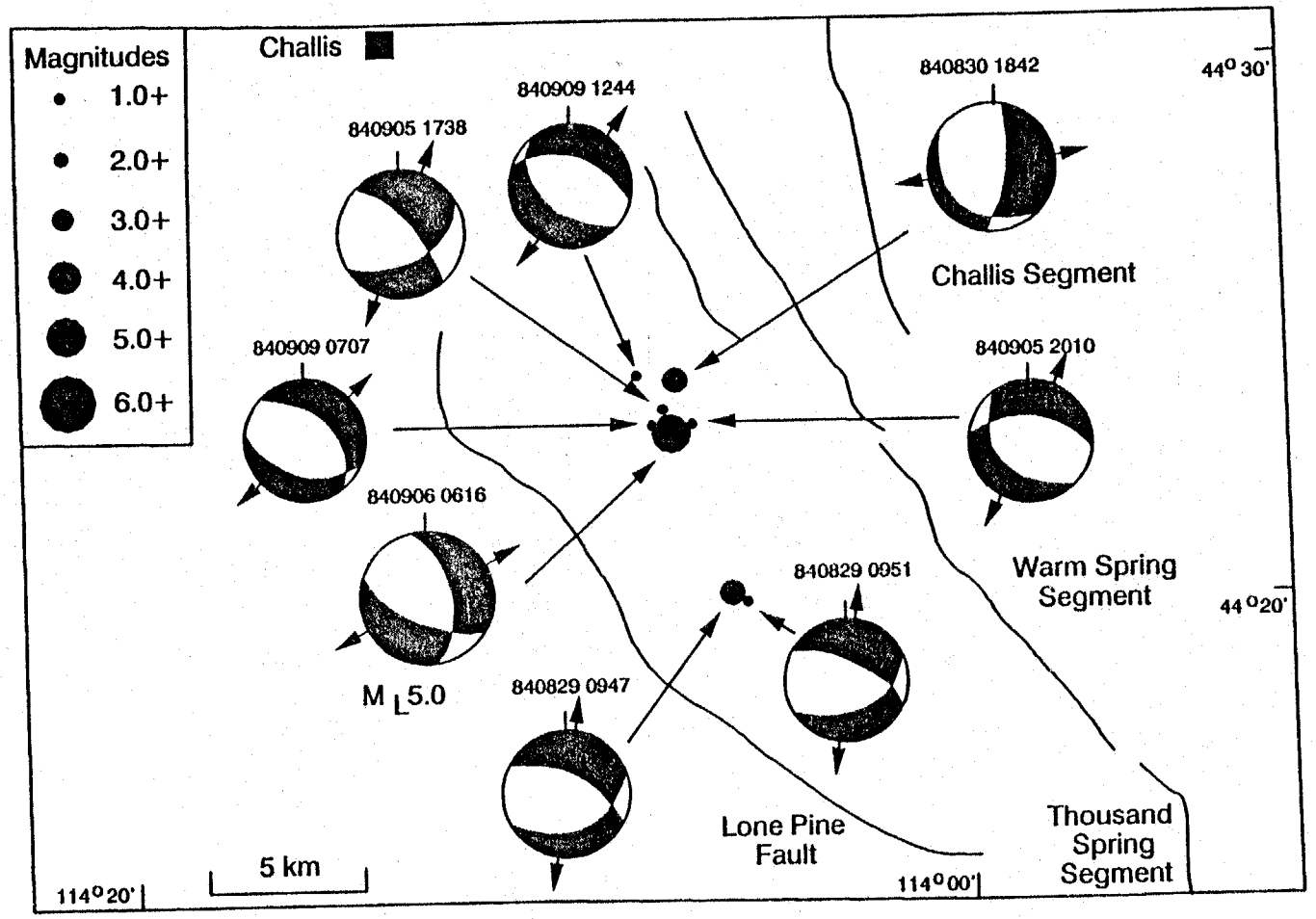

Figure 18. Lower hemisphere focal mechanisms for aftershocks ($M_L \geq 1.0$) along the Lone Pine fault. The focal mechanisms 840909 0707 and 840909 1244 are representative of fourteen and five similar focal mechanisms, respectively (see Appendix D). Compressional quadrants are shaded. Orientations of the T-axes are indicated by short arrows extended from the focal spheres. Numbers indicate the date (year, month, and day) and time (hour and minute) in UTC.

These nodal planes strike more west-northwest and have steeper dips than those for the northern portion of the Lone Pine fault (Table 3). The T-axes for these two focal mechanisms are oriented N 3-4° E and are not consistent with the T-axes orientations of the focal mechanisms along the northern portion of the Lone Pine fault.

Selected focal mechanisms for the aftershocks along the Lost River and Lone Pine faults and the mainshock are shown in Figure 19. The strikes of nodal planes for the focal mechanisms of the mainshock and aftershocks along the Challis and Warm Spring segments trend more NNE-SSW than for those of the aftershocks along the Lone Pine fault (Table 3). Nodal plane dips indicated by the focal mechanisms of both the mainshock and aftershocks are similar along both faults. The T-axes and plunge orientations for the mainshock and aftershocks are consistent with northeast-southwest direction of extension and predominantly normal faulting with a minor component of left-lateral strike-slip.

Resolution of Fault Orientations

Hypocenters with ERH $\leq$ 0.5 km and ERZ $\leq$ 1.0 km and the focal mechanism results (Table 3) were used to resolve the orientations of the faults. Since none of the aftershocks located south along the Warm Spring segment have values meeting these criteria, the following discussion focuses on resolution of the southwest and northeast dipping faults associated with the Challis segment and Lone Pine fault, respectively. Based on the limited data of eleven hypocenters and results of the four focal mechanisms, the Warm Spring segment may strike

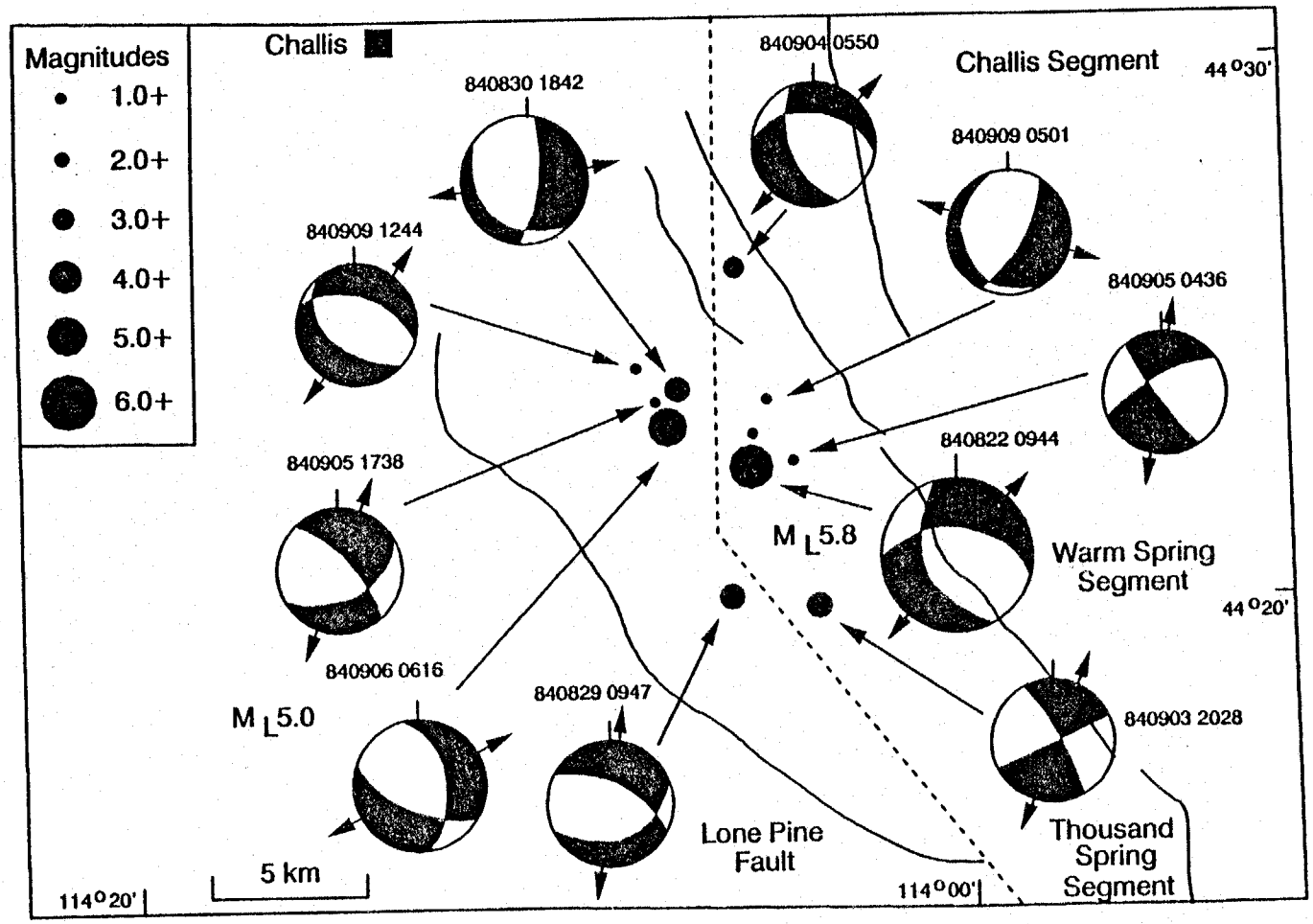

Figure 19. Lower hemisphere focal mechanisms for aftershocks ($M_L \geq 1.0$) along the Challis segment and Lone Pine fault. Focal mechanisms were selected from Figures 17 and 18. Focal mechanism for the M_L 5.8 earthquake was obtained from Zollweg and Richins (1985). Compressional quadrants are shaded. Orientations of the T-axes are indicated by the short arrows extended from the focal spheres. Numbers indicate the date (year, month, and day) and time (hour and minute) in UTC.

N 20-25° W and dip 70° SW, whereas the southern portion of the Lone Pine fault may strike N 62° W and dip 55° NE.

Ninety-five hypocenters having horizontal and vertical errors less than 670 and 1350 m, respectively, at the 95% confidence level are shown in cross-sections perpendicular to the Challis segment and Lone Pine fault in Figure 20. The best orientation for a cross-section through forty-six hypocenters which results in the least amount of scatter about the southwest dipping fault is perpendicular to the strike, N 25° W, of the central strand of the Challis segment. Visually projecting lines to the surface traces of the Challis segment from the hypocenters suggests apparent dips of 60°, 75°, and 87° SW for the eastern, central, and western strands, respectively (Figure 20 a). Because there are very few aftershocks located at depths less than 6 km, there are three possible fault plane orientations: 1) a plane striking N 25° W and dipping 87° SW, associated with the western strand; 2) a plane striking N 25° W and dipping 75° SW, associated with the central strand; or 3) a plane striking N 14° W and dipping 60° SW, associated with the eastern strand.

Hypocenters located west of the primary southwest dipping fault could be associated with the western strand of the Challis segment, but the dip of 87° SW exceeds the mean value for the dips of the focal mechanisms (50$\pm$20° SW; Table 3), by about two standard deviations. Since the aftershock activity extends along an 11-km length of the fault, hypocenters to the west of the fault in this orientation of the cross-section (Figure 20 a) may be more representative of an irregular fault surface than an indication of activity along the western strand.

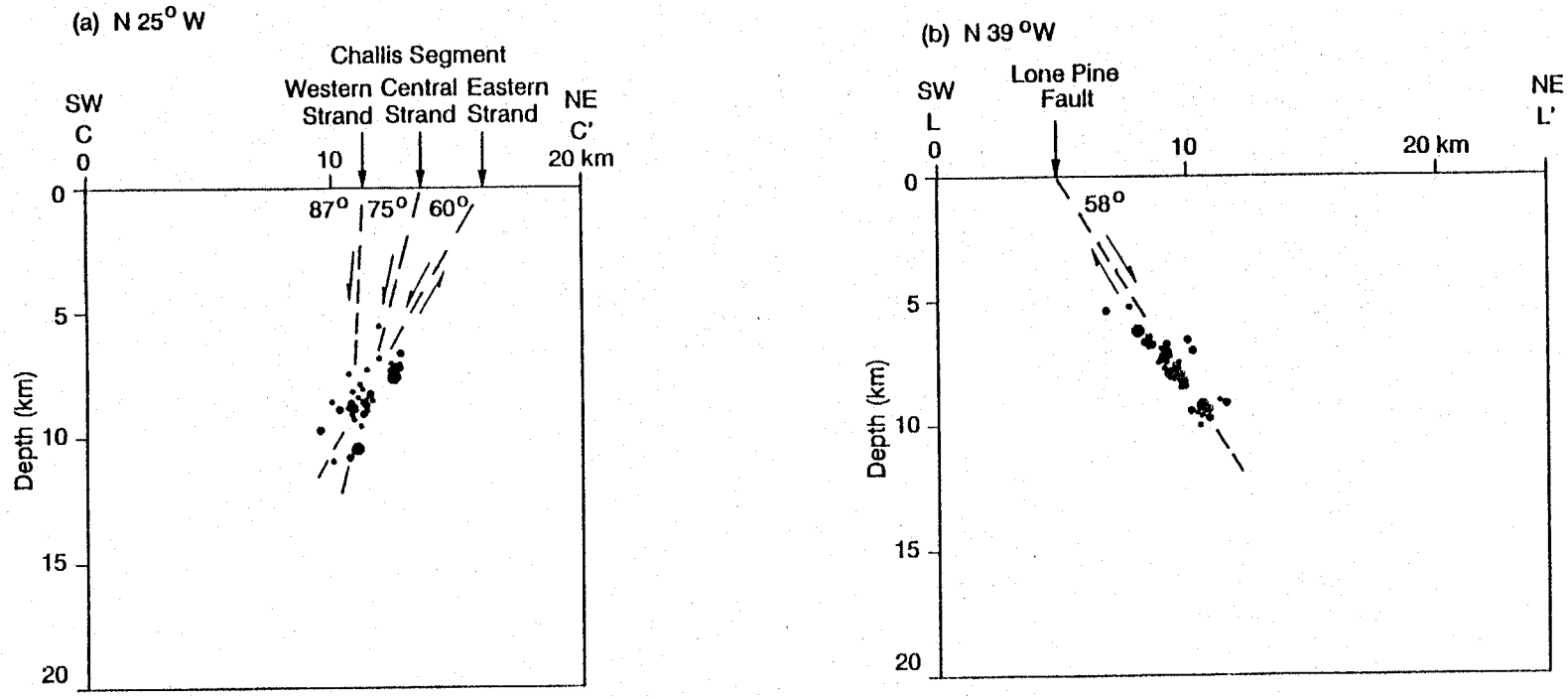

Figure 20. Cross-sections through ninety-five hypocenters oriented perpendicular to the: (a) Challis segment; and (b) Lone Pine fault. Maximum errors of the hypocenters are 670 m horizontally and 1350 m vertically at the 95% confidence level. Dashed lines show possible fault orientations determined by visually projecting a line from the hypocenters to the surface trace of the faults. Arrows indicate the sense of movement along the faults. See Figure 9 for magnitude scale.

The strike directions for the central and eastern strands are consistent with the mean strike value of the focal mechanisms, N 22±20° W (Table 3), but the dip of 60° SW for the eastern strand is more consistent with the average dip value of 50±20° SW (Table 3) than the dip of 75° SW for the central strand. Based on the alignment of the hypocenters with the surface traces of the faults, the southwest dipping fault is interpreted to be associated with movements along the eastern or central strands of the Challis segment.

A cross-section oriented perpendicular to N 39° W, the strike of the Lone Pine fault, shows the best orientation for the alignment of forty-nine hypocenters that cluster about the northeast dipping fault. A line visually projected from the surface trace of the Lone Pine fault through the hypocenters results in an apparent dip of 58° NE (Figure 20 b). The average value and one-standard deviation for the preferred nodal planes from the focal mechanisms strike N 47±32° W and dip 46±22° NE (Table 3). Both the strike and dip indicated by the hypocenter distribution are consistent with the focal mechanism results.

CHAPTER 5. DISCUSSION

Style of Faulting

Based on the focal mechanisms and hypocenter locations of the majority of aftershocks, the 1984 Devil Canyon earthquake sequence was associated with normal slip along the Challis segment and Lone Pine fault, two northwest-striking conjugate normal faults which bound the Warm Spring Creek graben. The August 22, 1984, M_L 5.8, mainshock was associated with rupture along the Challis segment and the September 8, 1984, M_L 5.0, primary aftershock was associated with rupture along the Lone Pine fault. The Devil Canyon aftershock hypocenters are confined to planar fault zones bordering the Warm Spring Creek graben. This indicates that from August 27 to September 14, 1984 the down-dropped block of the Warm Spring Creek graben experienced no internal brittle deformation and rupture was concentrated along the bounding normal faults (Figure 12). The aftershock activity occurred along an 11-km length of the Challis segment and 5-km length of the Lone Pine fault, and was confined to the brittle upper crust from 5 to 13 km depth (Figure 11).

Since very few aftershocks (eleven) were associated with the Warm Spring segment and southern portion of the Lone Pine fault during this time period (Figures 10 and 13), the following discussions of geometry, temporal patterns, kinematics, and mechanics of faulting focus on the

nature of conjugate faulting displayed by the Challis segment and northern portion of the Lone Pine fault. The few aftershocks that were located in the southern region along the Warm Spring and southern portion of the Lone Pine fault may not be related to the conjugate normal faulting along the Challis segment and northern portion of the Lone Pine fault because the southern region had been active following the Borah Peak mainshock, prior to the August 22, 1984 event (Figure 3).

Fault Geometries

Hypocenters for the southwest-dipping Challis segment are interpreted to define a fault plane that strikes N 14-25° W and dips 60°-75° SW, whereas hypocenters for the northeast-dipping Lone Pine fault define a fault plane that strikes N 39° W and dips 58° NE (Figure 20). The focal mechanisms and distribution of hypocenters associated with movements along the central and eastern strands of the Challis segment suggests that two possible fault geometries may exist: 1) a planar fault striking N 14° W and dipping 60° SW associated with the eastern strand; or 2) a planar fault striking N 25° W and dipping 75° SW associated with the central strand. Based on the following observations, the hypocenters are interpreted to be associated with the central strand of the Challis segment (Figure 21 a): 1) the average strike of the aftershocks (N 22$\pm$20° W) and mainshock (N 27° W) focal mechanisms are consistent with the strike of the central strand (N 25° W); 2) the central strand of the Challis segment has evidence of repeated Quaternary offset (Crone and Haller, 1991) whereas the eastern

strand is concealed beneath Quaternary landslide deposits (Hobbs et al., 1991); and 3) the central strand of the Challis segment is aligned with the segments of the Lost River fault whereas the eastern strand is offset 2.5 km to the east and bends away from the Lost River fault trend. However, movements associated with the eastern strand cannot be ruled out because there is very little aftershock activity along the Challis segment at depths less than 6 km.

The strike of the Lone Pine fault, N 39° W is consistent with the average value of the preferred nodal planes of the focal mechanisms, N 47°$\pm$32 W. A dip of 58° NE for the Lone Pine fault is close to within one standard deviation of the mean dip N 35$\pm$19° E suggested by the focal mechanisms (Table 3). This correspondence between the distribution of hypocenters and focal mechanisms suggests that the Lone Pine fault is a planar fault that strikes N 39° W and dips 58° NE.

The preferred orientation for the Challis segment is a planar fault that strikes N 25° W and dips 75° SW. The orientation for the Lone Pine fault is a planar fault oriented N 39° W and dipping 58° NE (Figure 21 a). The distribution of hypocenters merge near a depth range of 10 to 11 km (Figure 12) suggesting the conjugate faults merge at this same depth range. The mainshock occurs slightly below the intersection of these faults (Figures 12 and 21a). Based on the geometry in Figure 21 (b), the Lone Pine fault could: 1) terminate near the intersection with the Challis segment, since the mainshock is postulated to be associated with the Challis segment; or 2) continue with the same 58° NE angle with depth. The Challis segment could: 1) terminate near the

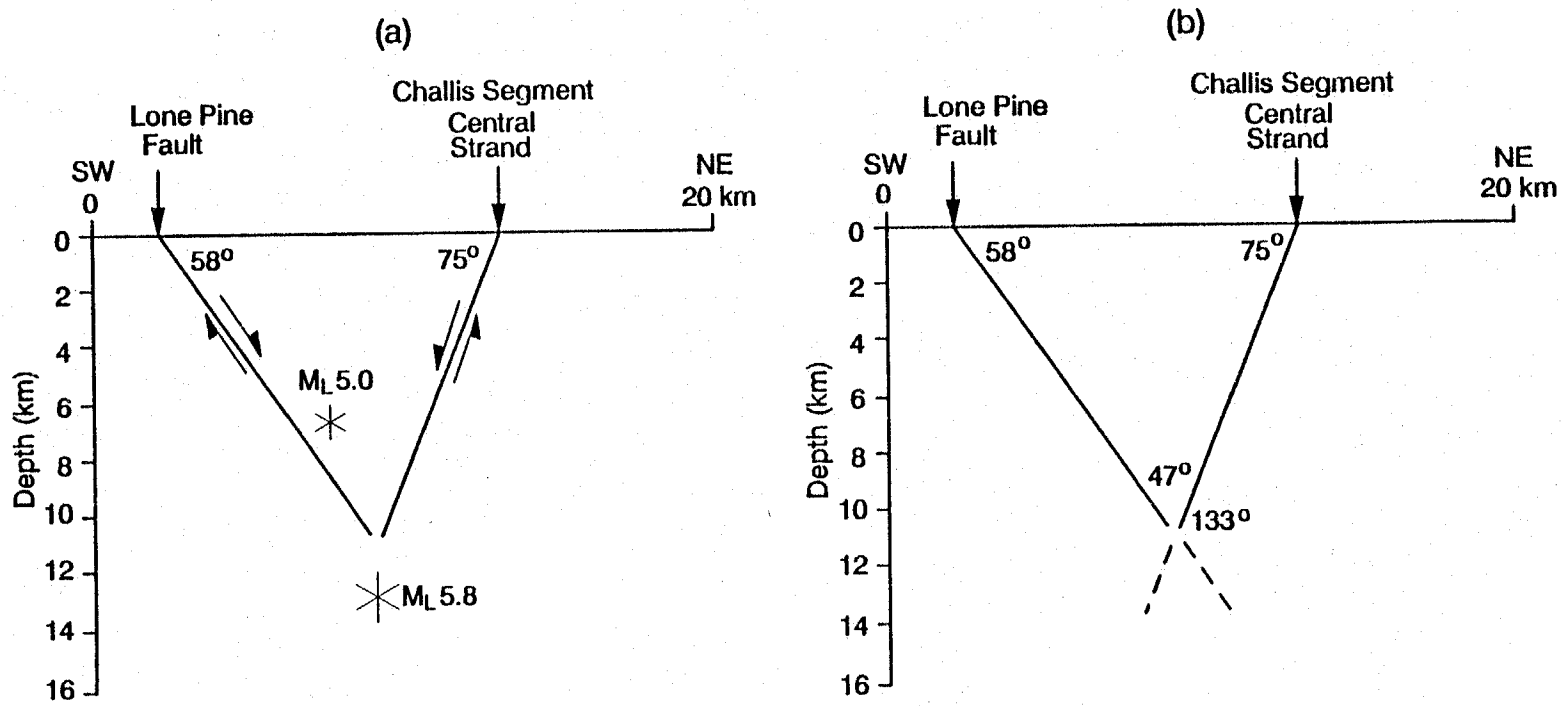

Figure 21. (a) Interpreted fault geometries for the Lone Pine fault, and central strand of the Challis segment based on the distribution of hypocenters. Stars indicate the depths of the M_L 5.8 mainshock and the largest M_L 5.0 aftershock (this study). (b) acute and obtuse angles for the conjugate orientation of the Challis segment and Lone Pine fault. Dotted line schematically represents the acute and obtuse angles of the conjugate fault planes.

intersection with the Lone Pine fault; or 2) continue with the same 75° SW angle with depth. Since aftershocks are not located below the mainshock on either the Challis segment or Lone Pine fault, no information is available to determine the orientation of the faults below 13 km.

The orientations of these faults indicates the 1984 Devil Canyon sequence was associated with conjugate normal faulting. Using the dips of 75° SW and 58° NE, the acute angle that bisects the conjugate faults is 47° and the obtuse angle is 133° (Figure 21 c). These values are consistent with the angles that result from physical and theoretical models of conjugate faulting (Horsfield, 1980; Davis, 1984). The strike of these faults indicate that they are oriented in an oblique manner to each other. Their line of intersection trends N 33° W and plunges about 10° N.

Temporal Pattern of Faulting

The temporal faulting pattern suggests alternating movements along the Challis segment and Lone Pine fault. The 1984 Devil Canyon sequence began with a M_L 5.8 mainshock on August 22, 1984 which occurred near the segment boundary between the Warm Spring and Challis segments at a depth of 12.8±0.7 km. Hypocenters were located primarily along the Challis segment from August 27 to September 7, 1984, although several were located at depth on the Lone Pine fault. During this period, a spatial migration of hypocenters toward the northwest and from deeper to shallower depths is apparent in the cross sections parallel and perpendicular to the Challis segment, respectively. Hypocenters

associated with the Lone Pine fault were located near the Challis segment and at deep depths, then migrated to the west and shallower depths (Figures 14 and 15).

The M_L 5.0 primary aftershock occurred 17 days later on September 8, 1984 and was associated with the Lone Pine fault. It was located to the northwest and at a shallower depth (7.1±1.9 km) than the mainshock hypocenter. Following this event from September 8 to 14, 1984 the aftershock activity shifted to the Lone Pine fault at depths of 3 to 8 km. During this time, the number of aftershocks occurring on the Challis segment decreased significantly (Figure 16).

Freund (1974) suggested that it is unlikely conjugate faults operate simultaneously and that each conjugate fault would be active during different time periods. In sand box experiments, Horsfield (1980) observed that alternating movements on conjugate normal faults occurred with gradual offset of small segments along each fault near their intersection during the same time period. The observed temporal pattern of conjugate faulting along the Challis segment and Lone Pine faults from August 27 to September 14, 1984 is consistent with Horsfield's (1980) observations.

Fault Kinematics

Rupture Direction

Based on the location of the mainshock at the southeastern end of the Challis segment, its deeper depth than the majority of aftershocks, and spatial migration of the aftershocks to the northwest and shallower depths, the mainshock ruptured unilaterally to the northwest and upward

along the Challis segment. The spatial migration of aftershocks from deeper to shallower depths on the Lone Pine fault and the northwest location of the epicenter for the primary aftershock relative to the mainshock epicenter may suggest a unilateral rupture pattern upward and to the northwest along the Lone Pine fault. Similar observations for the location of the mainshock and aftershock distribution along fault strike were used to infer a unilateral northwest rupture direction for the Borah Peak earthquake (Doser and Smith, 1985). Moderate to large magnitude mainshocks of Basin and Range earthquakes generally nucleate near the base of the seismogenic crust where shear stresses are greatest, and rupture upward to the surface (Sibson, 1982; Das and Scholz, 1983; Smith and Bruhn, 1984; Doser and Smith, 1989).

The northwest rupture direction along the Challis segment and northern portion of the Lone Pine fault may have been influenced by: 1) a low stress region along the Warm Spring segment and southern portion of the Lone Pine fault; or 2) the nature of the segment boundaries along the Lost River and Lone Pine faults. Dynamic ruptures along the Challis segment and northern portion of the Lone Pine fault may not have propagated to the southeast because they would have been terminated rapidly as they propagated into a low stress or unstressed region. Stress in the region along the Warm Spring segment and southern portion of the Lone Pine fault was most likely released by the Borah Peak aftershock activity and coseismic rupture, or possibly creep (Figure 3).

Alternatively, the nature of the segment boundary between the Warm Spring and Challis segments may have played a role in influencing the rupture direction and location of rupture nucleation for the August 22,

1984 mainshock and September 8, 1984 aftershock. Segment boundaries along faults may be characterized by irregularities along the fault which include steps, bends, branching faults, and cross faults and may also be the site of rupture nucleation or termination (Bruhn et al., 1987, 1990, 1991; Crone and Haller, 1991; Machette et al., 1991; Sibson, 1987, 1989; Zhang et al., 1991; Scholz, 1990). Along the central part of the Lost River fault, Janecke (1993) suggests that segment boundaries coincide with two types of structural complexities: 1) zones of distributed faults and steps or jogs in the normal faults; and 2) intersections with pre-existing Eocene to Oligocene cross faults.

At Devil Canyon, the location of the segment boundary between the Warm Springs and Challis segments, there is a 500-m left step between the Warm Spring segment and central strand of Challis segment, and several short, northwest-striking normal faults. Near this location, the Challis segment also diverges into at least three fault strands, the western, central, and eastern strands (Figure 22). Recent, unpublished geologic mapping does not indicate any evidence for a cross fault near this location (M. Anders, personal communication, 1993). The short, northwest-striking normal faults between the Warm Spring and Challis segments may have arrested the spread of rupture to the south either by rupture branching or interlocking of subsidiary faults (King, 1983; Bruhn et al., 1987, 1990), as suggested by Susong et al. (1990) for the explanation of rupture direction for the Borah Peak earthquake. Based on the epicenter and its location error relative to the segment boundary, it is possible that the Challis and Warm Spring segments' intersection zone may also be coincident with the nucleation depth of

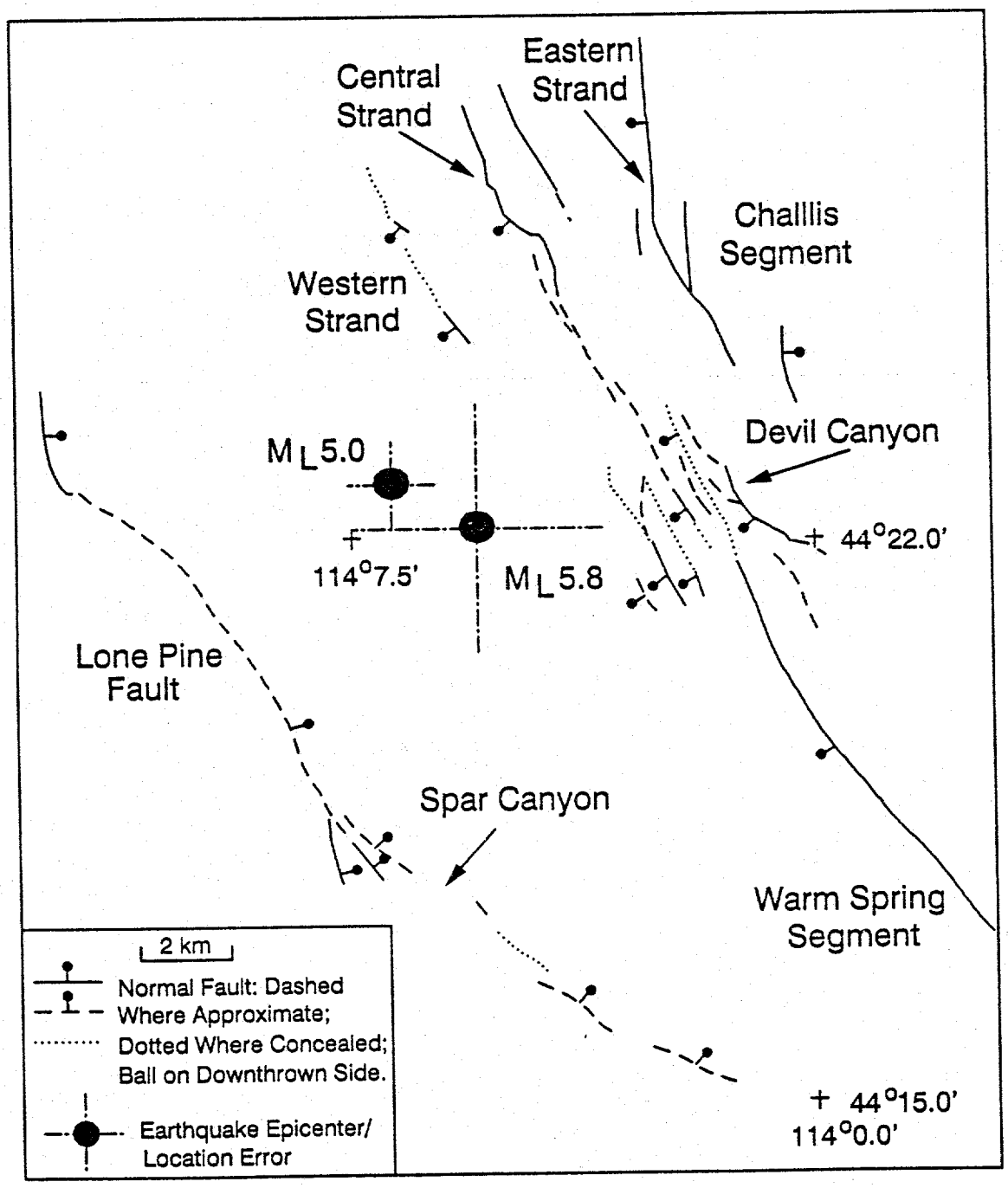

Figure 22. Normal faults along the Warm Spring and Challis segments and the Lone Pine fault (Rember and Bennett, 1979; Fisher et al., 1983; Hobbs et al., 1991). Epicenters and location error are shown for the M_L 5.8 mainshock (Zollweg and Richins, 1985) and M_L 5.0 largest aftershock (this study).

the M_L 5.8 mainshock (Figure 22). However, it was not possible to quantitatively determine depth projections of the intersection zone because the strikes of the central strand (interpreted to have been active during this sequence) of the Challis segment and Warm Spring segment differ by only 5° and no detailed mapping of the short northwest-striking normal faults is available to provide estimates of their fault dips.

The rupture along the Challis segment appears to have caused the rupture on the Lone Pine fault. The M_L 5.0 and aftershocks on the Lone Pine fault are located to the northwest of M_L 5.8 hypocenter (Figures 14c, 15c, and 16c). Possibly the short, northwest-striking normal faults north of Spar Canyon arrested the spread of rupture to the south along the Lone Pine fault.

Nucleation Depth and Seismogenic Crustal Thickness

The 1984 Devil Canyon mainshock and primary aftershock nucleated within the brittle crust. The thickness of the seismogenic crust for this region is on the order of 16-20 km based on the nucleation depth of the Borah Peak mainshock (Smith et al., 1985). The 1984 Devil Canyon mainshock hypocenter was located at a depth of 12.8 $\pm$ 0.7 km whereas the primary aftershock was located at a shallower depth of 7.1 $\pm$ 1.9 km. Figure 23 shows that the aftershocks occur at depths of 12 km or less and no aftershocks occur at or below the depth of the mainshock.

One possibility for the lack of Devil Canyon earthquakes below 13 km could be that temperatures below this depth exceed the limiting temperatures of 350$\pm$100° C for earthquake nucleation (Chen and Molnar,

1983). Blackwell et al. (1992) provides evidence that the geothermal gradient in the Basin and Range province north of the eastern Snake River Plain is 25-36° C/km. Based on the gradient of 36° C/km, the limiting temperature of 450° C for earthquake nucleation would occur at about 13 km, close to the depth above which earthquakes occur in the Devil Canyon sequence. Other earthquake sequences generally have focal depths that terminate above the brittle/quasi-plastic transition. For example, focal depths of mainshocks and aftershocks in conjugate thrust sequences (discussed later in this chapter, Table 6) do not exceed 7 km.

Extensional Stress Direction

The orientation of minimum principal stress indicated by the T-axes from the 1984 focal mechanisms along both the Challis fault segment and Lone Pine fault are consistent with a northeast-southwest extensional direction, similar to the results of the extensional direction for the Borah Peak mainshock and its aftershocks and other earthquake focal mechanisms within this region of the Basin and Range province (Figure 24). Gephart and Forsyth (1985) suggested that P- and T-axes from focal mechanisms may be unreliable indicators of stress directions because earthquakes commonly occur along pre-existing zones of weakness. Since the T-axes for the Devil Canyon mainshock and aftershocks are consistent with T-axes for other stress indicators in this region (Zoback and Zoback, 1989), they are considered to be an indicator for the orientation of the regional extensional stress field. Focal mechanisms for both faults indicate predominantly normal faulting with small varying components of left-lateral strike-slip motion within

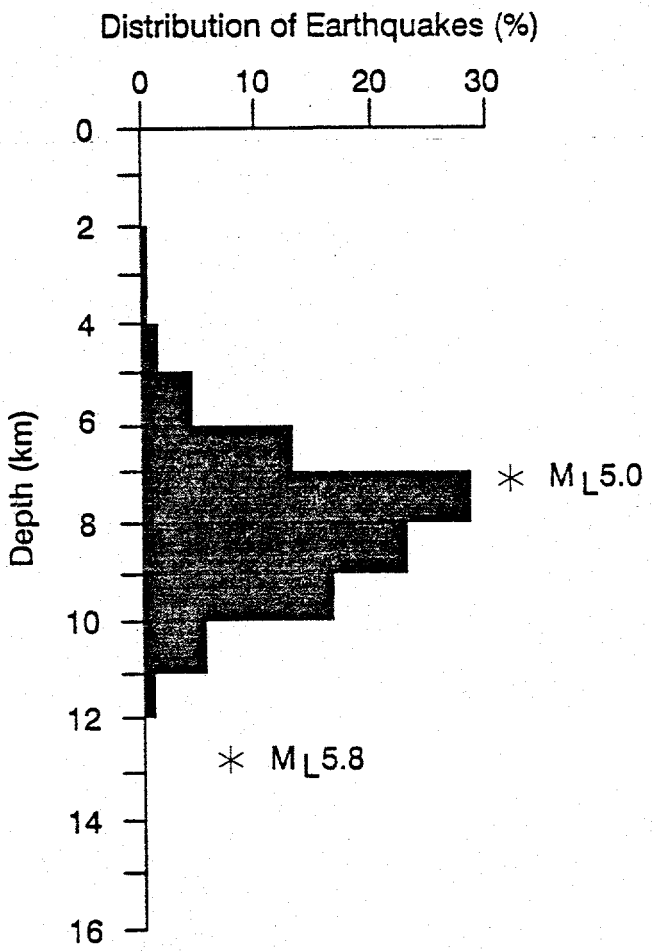

Figure 23. Percentage distribution of earthquakes with depth for the 1984 Devil Canyon sequence. Stars indicate the depth where the M_L 5.8 mainshock and M_L 5.0 primary aftershock occurred based on this study.

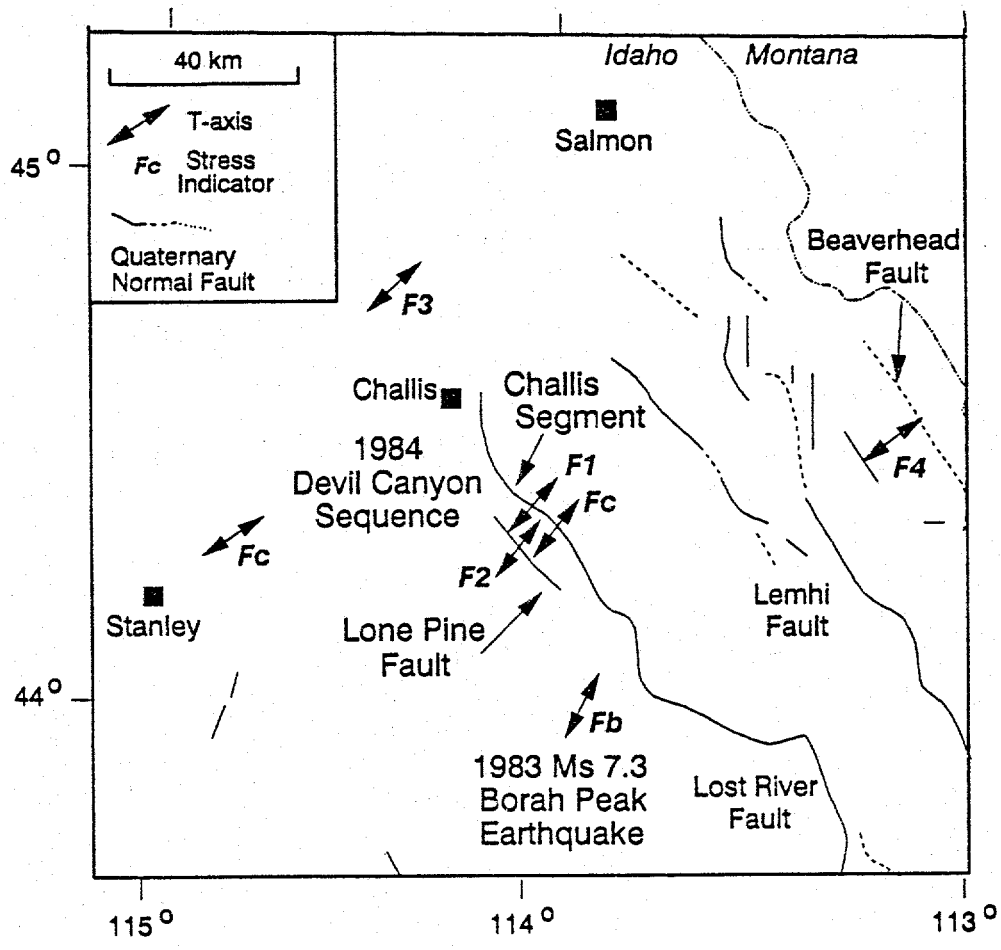

Figure 24. Distribution of minimum principal stress orientations from focal mechanisms (F) as compiled by Zoback and Zoback (1989). Quality ranking (b or c) as assessed by Zoback and Zoback (1989). *Fc* for the T-axis on the Challis segment is for the M_L 5.8 mainshock from Zollweg and Richins (1985). Also included are T-axes from other sources: *F1* and *F2* - are the averages of the T-axes from Table 3 (this study) for the Challis segment and Lone Pine fault, respectively; *F3* - Zollweg and Richins (1985); and *F4* - Stickney (1993). Figure modified from Jackson et al. (1993).

a uniform northeast-southwest oriented extensional stress field. The left-lateral strike-slip motion along the conjugate faults is consistent with the motion along the central portion of the Lost River fault and the Twin Peaks region (Figure 25).

Fault Mechanics

Stress Drops and Rupture Dimensions

The distribution of aftershock hypocenters define the mainshock rupture area of 11 km long by 11.5 km deep for the Challis segment (Figure 11 a). This results in moment magnitudes (M_w) of 6.1, 6.4, and 5.9 using Wells and Coppersmith's (1994) relationships for rupture area, subsurface-rupture width, and subsurface-rupture length, respectively. The moment magnitude values overestimate the instrumentally determined magnitudes M_L 5.8, M_s 5.1, m_b 5.0, and M_w 5.6 (M_w estimated from body waves; NEIS, 1984a) for the mainshock. M_w 5.7, 6.3, and 5.3 were estimated for the same fault-dimension relationships (respectively) using a fault area 5 km long and 10 km wide as indicated by the distribution of hypocenters for the Lone Pine fault. These values also exceed the instrumentally determined magnitudes M_L 5.0, M_s 4.4, and m_b 5.0 (NEIS, 1984b) for the primary aftershock. Using the spatial distribution of aftershock hypocenters (5 to 23 days later) to define the subsurface fault dimensions may result in overestimates of the true moment magnitudes of the mainshock because aftershocks may extend beyond the zone of coseismic rupture (Mendoza and Hartzell, 1988; Dietz and Ellsworth, 1990).

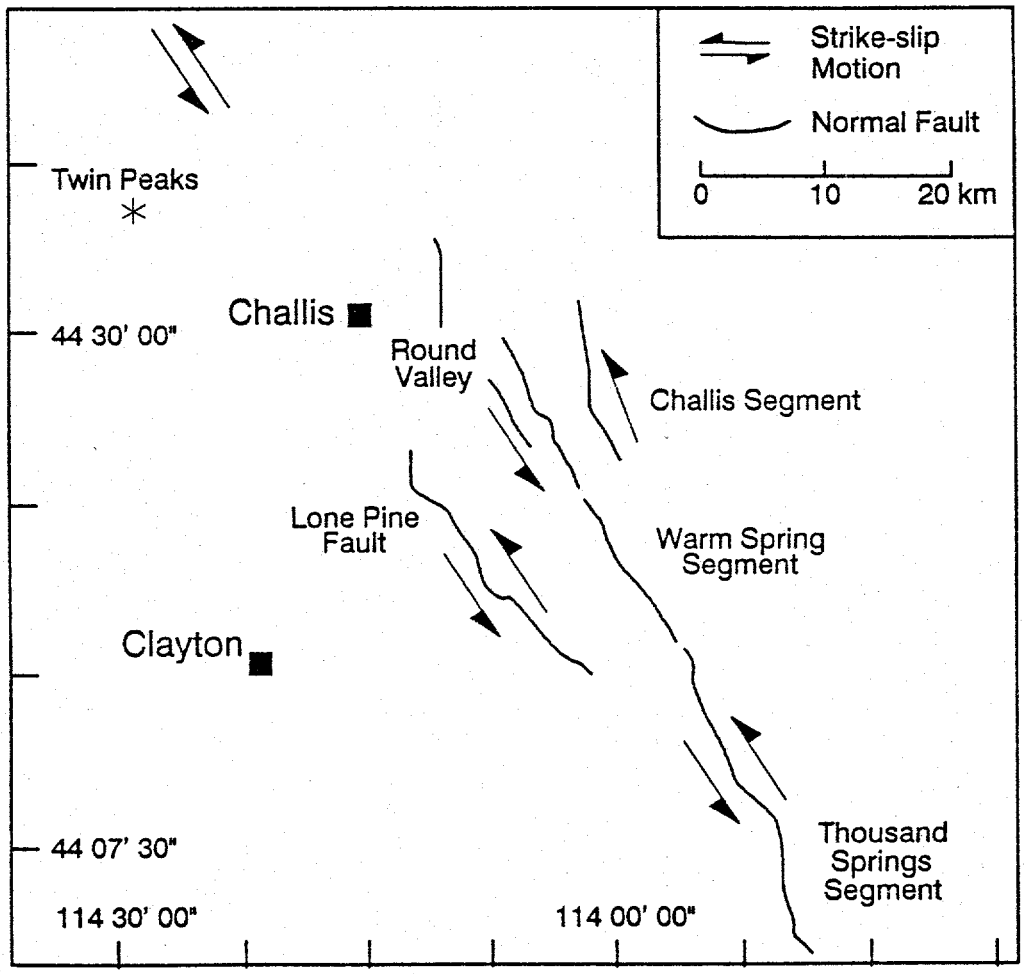

Figure 25. Direction of strike-slip motion along the fault segments of the Lost River fault from focal mechanisms (this study; Zollweg and Richins, 1985; Richins et al., 1987).

A static stress drop of 1.4 MPa or 14 bars was estimated for the M_L 5.8 mainshock using the width-dependent relationship for static stress drop, since $L \leq 2W$ (Starr, 1928; Scholz, 1982):

$$\Delta\sigma = 8\frac{M_o}{3\pi W^2 L} \qquad [3]$$

where M_o is the seismic moment, 2.4×10^{24} dyne-cm (NEIS, 1984a); W is the fault width (cm); and L is the fault rupture length (cm). The static stress drop of 14 bars for the mainshock is consistent with the Borah Peak earthquake suggesting it may also be a low stress drop event. Doser and Smith (1985) estimated static stress drops of 12 to 17 bars for the Borah Peak earthquake. Boatwright and Choy (1985) estimated a static stress drop of 17 bars and dynamic stress drop of 28 bars for the Borah Peak mainshock. Boatwright (1985) estimated an average of 36 bars from a range of 2 to 189 bars for 57 Borah Peak aftershocks. Doser and Smith (1985) suggested that the Borah Peak earthquake was a low stress drop event and, considering the errors in stress drop measurements, concluded the Borah Peak earthquake did not exceed 75 bars.

Rupture Mechanics

The rupture along the Challis segment appears to have induced rupture along the Lone Pine fault, initially at depth and later in the form of a M_L 5.0 earthquake and its shallower aftershocks. Figure 26 (a) shows the inferred orientation of the faults before the M_L 5.8 earthquake and Figure 26 (b) shows their orientation after the mainshock. Fault slip along the Challis segment may have caused the

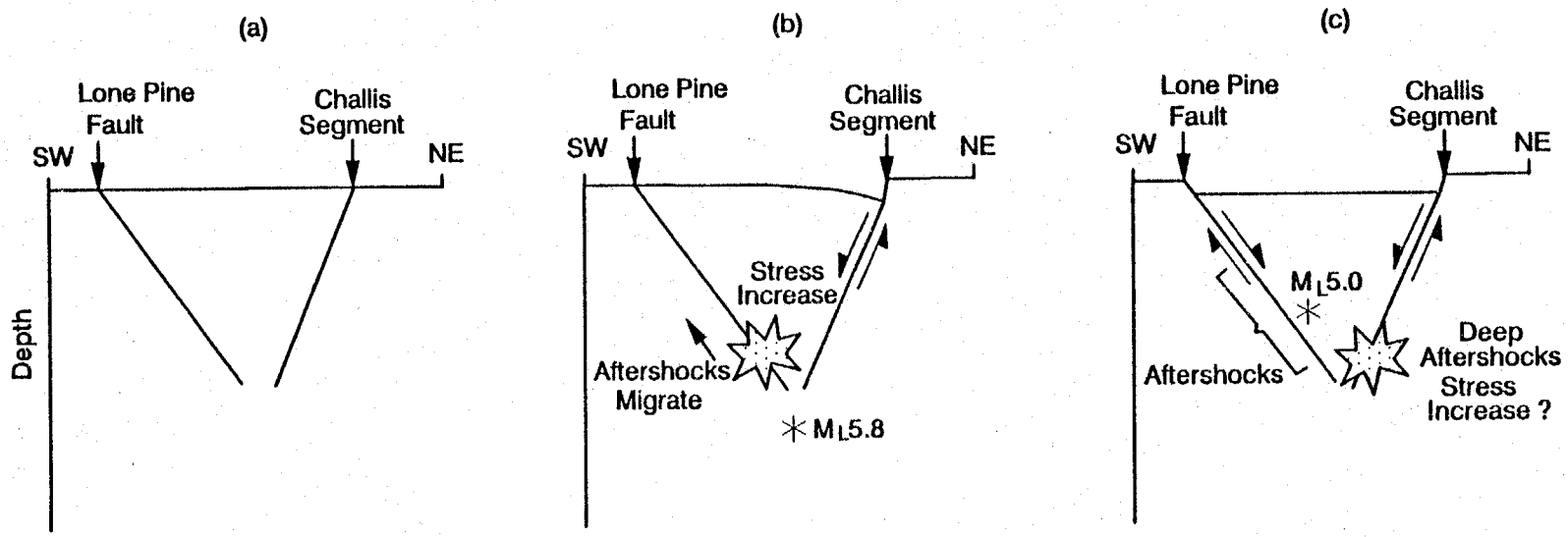

Figure 26. Diagrams showing the conjugate normal faulting process for the Devil Canyon sequence: (a) prior to the M_L 5.8 mainshock; (b) following the M_L 5.8 event and prior to the M_L 5.0 primary aftershock; and (c) following the M_L 5.0 primary aftershock. Shaded star indicates area for increased shear stress.

Lone Pine fault to become active near the intersection with the Challis segment, reflecting a concentration of stresses at this location (Figure 14 b).

On the Lone Pine fault, earthquakes migrated up dip from the intersection of the faults to the region of the M_L 5.0 hypocenter prior to its occurrence. Perhaps the concentration of earthquakes at these locations on the Lone Pine fault reflects increased shear stress caused by movement along the Challis segment. Das and Scholz (1981) estimated changes in the static shear stress field due to a two-dimensional, in-plane, Griffith shear crack of half-length unity representing a strike-slip fault. Their results show increased shear stress near the crack tips and in broad zones off the crack in the normal direction. Stein and Lisowski (1983) calculated a similar pattern of stress increases for the 1979 Homestead Valley, California earthquakes. In their analysis, they calculated postearthquake changes for shear and normal stresses acting on a vertical plane oriented parallel to the strike of the Homestead Valley coseismic strike-slip fault plane. When compared to earthquake sequences, both analyses show off-fault clusters of aftershocks located normal to the fault plane in regions of increased shear stress (Das and Scholz, 1981; Stein and Lisowski, 1983). Furthermore, Yamashina (1980) showed examples of off-fault aftershocks occurring on the plane conjugate to the mainshock. By analogy with the results of Das and Scholz (1981) and Stein and Lisowski (1983), off-fault increases in shear stress normal to the fault plane should be expected for normal faults.

When off-fault aftershocks are observed, Das and Scholz (1981) suggested that either the rocks in this region are at a prestress level very close to that at which slip occurs or the mainshock has a high stress drop, because the increase in shear stress in the off-fault region is about 10% of the stress drop on the crack for the mainshock. Most likely the Lone Pine fault was at a prestressed level near its yield strength for rupture to occur, since the M_L 5.8 mainshock had a low stress drop.

Following the M_L 5.0, few earthquakes occurred near the base of the Lone Pine fault. While the majority of earthquake activity shifted to the central portion of the Lone Pine fault, some earthquakes occurred along the Challis segment near the intersection between the faults (Figures 16 b and 26 c). Possibly, the slip along the Lone Pine fault then caused an increase in shear stress on the Challis segment. However, the stress level along the Challis segment would have been lower than it was prior to the M_L 5.8 mainshock and subsequent aftershocks, and therefore few aftershocks would be associated with it, as observed. Based on these observations, the faults appear to be mechanically coupled and slip along one fault induces slip along the other, possibly due to increased shear stress.

Conjugate Normal Faulting

Davis (1984) defines conjugate faults as faults which occur in two intersecting sets and are coordinated kinematically, with each set distinctive in orientation and sense of shear. An alternative interpretation for similar faults is that the faults reflect antithetic

faulting, which Mandl (1988) defines as a fault that adjusts to slip on the dominating fault, and is located near abrupt changes in the main fault geometry. The interpretation of the Devil Canyon earthquake sequence seems more consistent with the definition for conjugate faults proposed by Davis (1984). The Devil Canyon sequence involves normal faults that have their own orientations and sense of slip, but are mechanically coupled, leading to a cause-and-effect relationship for contemporaneous slip along each fault. Observations supporting conjugate normal faulting during the Devil Canyon sequence are: 1) the northwest-striking normal faults dip in opposite directions and have a conjugate orientation (Figure 21); 2) temporal patterns of aftershocks on both faults indicate that the faults were active contemporaneously (Figures 14, 15, and 16); and 3) the Challis fault segment and Lone Pine fault both show evidence of Quaternary offset (Hobbs et al., 1991; C. Waag, personal communication, 1993) which may suggest that one fault does not dominate over the other.

Conjugate normal faulting as observed in the 1984 Devil Canyon sequence may be a possible mechanism for the style of faulting at the fault terminations near the northwestern ends of the Lost River, Lemhi, and Beaverhead faults where they intersect with the trans-Challis fault system. A focal mechanism from a M_L 4.0 earthquake suggests the presence of a west-valley bounding fault opposite the main Beaverhead fault near its northwestern termination (Figure 24) (Stickney, 1993). Contemporaneous activity along these conjugate normal faults provides a way of distributing slip along two faults, thus decreasing the topography near the northwestern ends of the ranges.

Comparison to Other Conjugate Faulting Earthquake Sequences Worldwide

Normal Conjugate Faulting

Two other conjugate normal faulting sequences have been seismologically observed worldwide. These are the 1980 Irpinia, Italy and 1982 North Yemen, Arabian Peninsula earthquake sequences. For comparison, the fault geometries and rupture processes of these two sequences and Devil Canyon are summarized in Table 4. The 1980 and 1982 sequences both have teleseismic waveform analyses to indicate the style of faulting by the mainshock. These indicate that the Irpinia M_s 6.9 mainshock coseismically ruptured both conjugate faults (Bernard and Zollo, 1989), and the North Yemen M_s 6.0 mainshock ruptured one of the conjugate faults and the other conjugate fault was active during the aftershock sequence (Choy and Kind, 1987).

Without the benefit of the information that might result if teleseismic waveform modeling of the mainshock were available, the Devil Canyon sequence is more similar to the North Yemen sequence. Teleseismic waveform modeling has not been done because of the low magnitudes, M_s 5.1 and 4.4 (NEIS, 1984a; 1984b), and poor recordings at telseismic distances of the Devil Canyon mainshock and largest aftershock, respectively. In the North Yemen sequence, the mainshock initially ruptured an east-dipping fault (Choy and Kind, 1987), but aftershocks for the time period of detailed earthquake monitoring indicated activity primarily occurred along a conjugate west-dipping fault (Langer et al., 1987). Following this activity, a m_b 4.6 earthquake and subsequent aftershocks occurred on the east-dipping fault (Langer et al., 1987). The North Yemen sequence shows contemporaneous

TABLE 4.

Seismologically observed conjugate normal faulting sequences.

Earthquake Sequence Date/Location	Fault Geometry Strike, Dip, Fault	Rupture Process	Data Analyses	Source
1984 Devil Canyon, Idaho, USA.	N 25° W, 75° SW on central strand of Challis segment of the Lost River fault; N 39° W, 58° NE on Lone Pine fault.	M_L 5.8 mainshock nucleates at a depth of 12.8 km near the intersection of the conjugate faults. It ruptures the Challis segment (central strand) of the Lost River fault unilaterally upward to the northwest. It induces a M_L 5.0 event on the Lone Pine fault which nucleates at a depth of 7.1 km and may have ruptured unilaterally upward to the northwest. Aftershock depths range 6 to 11 km.	Aftershock hypocenters and depth phases.	1
1980 Irpinia, southern Italy.	N 53° W, 60° NE on Carpineta, Marzano, Picentini, and San Gregorio faults; N 53° W, 20° NE on deeper portion of Marzano fault; N 53 W, 60-70° SW, unnamed fault.	M_s 6.9 mainshock nucleates at 16 km depth and is composed of multiple subevents. Initial subevents rupture bilaterally; to the northwest on the Carpineta, Marzano, and Picentini faults, and to the southeast on the San Gregorio fault. A subevent at 20 s is interpreted to rupture a deeper portion of the Marzano fault. A subevent at 40 s ruptures unilaterally to the southeast on an unnamed conjugate fault parallel to the Marzano fault.	Aftershock hypocenters, teleseismic waveform modeling, strong motion data, and leveling.	2 3 4
1982 North Yemen, southern Arabian Peninsula.	NNW, 65° E; NNW, 35° W; both on unnamed faults.	M_s 6.0 mainshock is composed of two subevents that both rupture portions of the E-dipping fault. Aftershocks 16-26 days later are associated with activity along the W-dipping fault. Aftershocks (including a m_b 4.6) 28-29 days later are associated with E-dipping fault. Mainshock nucleates at 7 km depth and rupture extends to a depth of 13 km. Most aftershocks are less than 8 km depth.	Aftershock hypocenters and teleseismic waveform modeling of broadband data.	5 6

Sources: (1) This study; (2) Crosson et al., 1986; (3) Bernard and Zollo, 1989; (4) Westaway, 1992; (5) Langer et al., 1987; (6) Choy and Kind, 1987

and alternating activity on the conjugate faults. Choy and Kind (1987) suggested that since the North Yemen earthquake occurred in a horst-graben setting, and where the normal faults are assumed to have nearly of equal strength, the state of stress on each fault segment is dependent on the state of stress of adjacent faults. As the region becomes critically loaded, rupture along one fault would cause rupture along other critically stressed faults. A similar relationship is suggested for the Devil Canyon sequence: changes in stress due to slip along the Challis segment caused the Lone Pine fault, which was already close to its yield stress, to slip.

The coseismic rupture of the Irpinia mainshock on conjugate faults suggests a possible cause-and-effect relationship between the faults. The initial subevents of the mainshock bilaterally ruptured northeast-dipping faults to the northwest on the Carpineta, Marzano, and Picentini faults and to the southeast on the San Gregorio fault. A subevent at 20 s is speculated to have ruptured a deeper portion of the Marzano fault. A subevent at 40 s ruptured a conjugate southwest-dipping unnamed fault parallel to the Marzano fault (Bernard and Zollo, 1989; Westaway, 1992). The rupture dimensions along the Marzano fault exceeded the dimensions of the conjugate fault (Crosson et al., 1986; Bernard and Zollo, 1989), similar to the relationship of rupture dimensions observed for the Challis segment and Lone Pine faults. Unfortunately, no details of the temporal patterns were available for the Irpinia aftershock analysis. Aftershock hypocenters show activity along both normal faults for the time period analyzed (Crosson et al., 1986).

Observations for the Irpinia and North Yemen sequences are consistent with the conjugate normal faulting observed during the Devil Canyon sequence. For all three conjugate normal faulting sequences, the results suggest a cause-and-effect temporal relationship between the faults. Slip along one of the conjugate faults may have caused slip along the other. In the Devil Canyon and Irpinia sequences, the dimensions of the fault associated with initial slip exceed those of the conjugate fault. It is speculated for both these sequences that stress changes resulting from slip along one fault caused slip to occur on the conjugate fault. For the Devil Canyon and North Yemen sequences, temporal patterns of aftershocks indicate alternating activity between the conjugate faults.

Strike-Slip and Thrust Conjugate Faulting

The results of four strike-slip and three thrust conjugate faulting sequences show both similarities and differences with the conjugate normal faulting observed in this study. Tables 5 and 6 summarize the seismologically observed results for the strike-slip and thrust conjugate sequences, respectively. All the strike-slip and thrust conjugate faulting sequences shown in Tables 5 and 6, share a cause-and-effect relationship between the conjugate faults and temporal earthquake patterns that indicate alternating activity between conjugate faults. The 1947 Manix, 1984 Round Valley, 1986 Chalfant, and 1987 Superstition Hills, California earthquake sequences had mainshocks or initiating foreshocks that were located at the intersection of the conjugate strike-slip faults (Priestly et al., 1988; Smith and Priestly,

TABLE 5.

Seismologically observed conjugate strike-slip faulting sequences.

Earthquake Sequence Date/Location	Fault Geometry Strike, Dip, Fault	Rupture Process	Data Analyses	Source
1947 Manix, California, USA	N 70° E, dip unknown on Manix fault; N 30° W, dip unknown on unnamed fault.	M_L 6.2 mainshock consisted of two subevents located at 5 km depth. The mainshock may have initiated near the intersection of the Manix and conjugate faults and is suggested to have ruptured to the southwest on the Manix fault. Largest aftershocks are interpreted to form a N 30° W trend, suggesting the presence of a conjugate fault.	Inversion of bodywave forms, surface rupture, and aftershock hypocenters.	7 8 9
1984 Round Valley, California, USA.	N 30° E, 90° on Round Valley fault; N 40° W, 55° NE on Hilton Creek fault.	M_L 5.8 mainshock and largest aftershock (M_L 5.2) rupture NE-striking fault. Within a few hours aftershocks occur on the NW-striking fault. Mainshock located at 13.4 km depth between conjugate faults. Focal mechanisms suggest brecciation of crustal volume between conjugate faults.	Aftershock hypocenters, moment tensor inversion, and surface wave modeling.	10
1986 Chalfant, California, USA.	N 30° E, 60° NW; N 25° W, 70° SW; both on unnamed faults.	M_L 5.7 foreshock ruptures downward and to the southwest on the NE-striking fault and occurs at the intersection of the two faults at depth of 6.7 km. The M_L 6.4 mainshock nucleates at a deeper depth than the foreshock and ruptures upward on the NW-striking fault.	Aftershock hypocenters and moment tensor inversion.	11

TABLE 5 Continued.

Seismologically observed conjugate strike-slip faulting sequences.

Earthquake Sequence Date/Location	Fault Geometry Strike, Dip, Fault	Rupture Process	Data Analyses	Source
1987 Superstition Hills, California, USA.	N 45° W, vertical on Superstition Hills fault; N 40° E, vertical on Elmore Ranch fault.	M_s 6.2 foreshock nucleates at 10 km depth and bilaterally ruptures to the northeast and southwest on the Elmore Ranch fault. The M_s 6.6 mainshock nucleates at a shallower depth near the intersection of the conjugate faults and ruptures southeast on the Superstition Hills fault.	Aftershock hypocenters and surface rupture mapping.	12 13
1992 Big Bear, California, USA. Aftershocks to Landers M_w 7.2 earthquake.	N 40° W, vertical; N 50° E, vertical; both on unnamed faults.	M_w 6.6 mainshock nucleates near the intersection of the conjugate faults. The first subevent ruptures primarily to the northwest and a few km to the southeast on the NW-striking fault. The second subevent 4-5 s later bilaterally ruptures to the northeast and southwest on the NE-striking fault.	Strong motion and broadband data.	14 15 16

Sources: (7) Richter and Nordquist, 1951; (8) Richter, 1958; (9) Doser, 1990; (10) Priestly et al., 1988; (11) Smith and Priestly, 1988; (12) Hudnut et al., 1989a 1989b; (13) Magistrale et al., 1989; (14) Hough and Jones, 1993; (15) Jones and Hough, 1993; (16) Jones and Hough, 1994.

TABLE 6.

Seismologically observed conjugate thrust faulting sequences.

Earthquake Sequence Date/Location	Fault Geometry Strike, Dip, Fault	Rupture Process	Data Analyses	Source
1982 Miramichi, New Brunswick, Canada.	S 15° W, 50° W; S 15° W, ~50° E; both on unnamed faults.	The m_b 5.7 mainshock nucleated at 7 km depth and ruptured upward and to the east on the W-dipping fault. Two large aftershocks m_b 5.1 and 5.0 also occurred on the W-dipping fault. The largest aftershock, m_b 5.4, was associated with the E-dipping fault. Mainshock and aftershocks less than 7 km depth and few earthquakes located within V-shaped block between faults.	Aftershock hypocenters and teleseismic waveform modeling.	17 18
1988 Tennant Creek, Australia.	N 65° W, 45° SSW on Kunayungku fault; N 65° W, 35° SSW on eastern Lake Surprise fault; N 15° E, ~40° SSW on western Lake Surprise fault; N 15° E, 55° NNW on unnamed fault.	The first M_s 6.3 mainshock nucleates at 6.5 km depth and ruptures upward to the northwest on the NW-striking, SSW-dipping Kunayungku fault. The second M_s 6.4 mainshock nucleates at 3.5 km depth, and its first two subevents rupture to the south on the SW-striking, SSW-dipping portion of the western Lake Surprise fault and its third subevent ruptures the SW-striking, NNW-dipping fault conjugate to the Lake Surprise fault. The third M_s 6.7 mainshock nucleates at 4.5 km depth and ruptures southeast on the NW-striking, SSW dipping eastern Lake Surprise fault.	Aftershock hypocenters, broadband teleseismic waveform modeling, and leveling.	19 20 21
1990 Nooksack Forks, Washington, USA	N ~40° E, ~45° NW; N ~40° E, ~45° SE; both on unnamed faults.	M_L 5.2 mainshock nucleated at a depth of 3 km. Aftershocks cluster about both the SE- and NW-dipping faults.	Aftershock hypocenters.	22 23

Sources: (17) Wetmiller et al., 1984; (18) Choy et al., 1983; (19) Choy and Bowman, 1990; (20) Bowman et al., 1990; (21) Bowman, 1991; (22) Amadi, 1992; (23) Qamar and Zollweg, 1990.

1988; Hudnut et al., 1989a, 1989b; Magistrale et al., 1989; Doser, 1990). The rupture directions in the 1984 Round Valley, 1986 Chalfant, and 1987 Superstition Hills sequences appeared to influence the point of rupture along the conjugate faults. The nucleating depths of their mainshocks and depths of the aftershocks extended as deep as 16 km (Priestly et al., 1988; Smith and Priestly, 1988; Hudnut et al., 1989a, 1989b; Magistrale et al., 1989). The 1982 Miramichi, New Brunswick, Canada, 1988 Tennant Creek, Australia, and 1990 Nooksack Forks, Washington conjugate thrust sequences showed a lack of aftershocks within the V-shaped region between the conjugate faults (Choy et al., 1983; Wetmiller et al., 1984; Choy and Bowman, 1990; Bowman et al., 1990; Amadi, 1992). The Tennant Creek and Nooksack Forks sequences had rupture dimensions for the mainshock faults that exceeded those for the conjugate faults (Bowman et al., 1990; Amadi, 1992).

There are a few differences between the strike-slip and thrust conjugate sequences and the conjugate normal faulting observed in the Devil Canyon sequence. The Round Valley, Chalfant, and Superstition Hills conjugate strike-slip sequences, and the Miramichi conjugate thrust sequence have conjugate faults with similar rupture dimensions (Wetmiller et al., 1984; Priestly et al., 1988; Smith and Priestly, 1988; Magistrale et al., 1989). The Round Valley sequence showed diffuse aftershocks between the conjugate faults suggesting brecciation of the rock between the faults (Priestly et al., 1988). The conjugate thrust sequences had mainshocks and aftershocks that occurred at depths less than 7 km.

In summary, the conjugate normal faulting sequences and the conjugate strike-slip and thrust sequences have three characteristics in common: 1) contemporaneous and alternating activity between the conjugate faults; 2) a cause-and-effect relationship suggesting the faults are mechanically coupled; and 3) changes in stress resulting from slip along one fault that cause increased stress and subsequent slip along the conjugate fault. Future conjugate faulting sequences can be expected to include these three characteristics. The conjugate normal and strike-slip faulting sequences had earthquakes nucleating at depths as deep at 16 km whereas those associated with the thrust conjugate faulting sequences were confined to depths less than 7 km. These differences may be related to the tectonic setting of the earthquake sequences and the small number of seismologically observed examples rather than the mechanics of conjugate faulting. Factors that may determine whether a conjugate fault becomes active include the rupture direction, location of the initiating event (mainshock or foreshock), and the stress level on pre-existing faults within the surrounding region.

CHAPTER 6. CONCLUSIONS

Detailed results of microearthquake monitoring by a temporary array south of Challis, Idaho indicate that the 1984 Devil Canyon earthquake sequence was associated with conjugate normal faulting. Well-determined hypocenters and focal mechanisms make it the best observed conjugate normal faulting sequence worldwide to date. Observed characteristics of the Devil Canyon sequence form the basis for a conceptual model of conjugate normal faulting that may have applications to future conjugate faulting sequences in various tectonic settings.

The distribution of hypocenters and focal mechanisms indicate that the southwest-dipping fault is associated with the central fault strand of the Challis segment and the northeast-dipping fault is associated with the Lone Pine fault. The Challis central fault strand is interpreted to be a planar fault that strikes N 25° W and dips 75° SW. The Lone Pine fault is also interpreted to be a planar fault that strikes N 39° W and dips 58° NE.

The temporal pattern of aftershocks indicates that the M_L 5.8 mainshock ruptured upward and to the northwest along the Challis segment and induced the M_L 5.0 primary aftershock along the Lone Pine fault. The rupture on the Lone Pine fault may also have been upward and to the northwest. The northwest rupture direction along both faults may have been influenced by: 1) a low stress region along the Warm Spring segment and southern portion of the Lone Pine fault; 2) short northwest-striking

normal faults near the segment boundary between the Challis and Warm Spring segments and near the bend where the Lone Pine fault strike changes direction. These short normal faults may have arrested the spread of rupture to the southeast by rupture branching or interlocking of subsidiary faults. The temporal patterns also suggest the faults were active contemporaneously, although the locus of the aftershock activity changed from the Challis segment to the Lone Pine fault.

Focal mechanisms indicate that the Challis segment and Lone Pine faults experienced predominantly normal faulting with minor components of left-lateral strike-slip. The T-axes for focal mechanisms along both faults are consistent with the northeast-southwest extensional direction, indicating a uniform stress field.

Finally, rupture dimensions indicate the M_L 5.8 mainshock may have been a low stress drop event (14 bars). It is suggested that stress changes resulting from the rupture of the M_L 5.8 mainshock along the Challis segment increased shear stresses on the Lone Pine fault, which was already close to its yield stress. This increase is inferred to have caused the M_L 5.0 primary aftershock and subsequent aftershocks to occur along the Lone Pine fault.

The conjugate normal faulting environment observed in the Devil Canyon sequence consists of normal faults that have their own orientations and sense of slip, but are mechanically coupled, leading to a cause-and-effect relationship for contemporaneous slip along each fault. This interpretation is supported by the following observations:

(1) The Challis segment and Lone Pine fault dip in opposite directions and have a conjugate orientation.

(2) The temporal pattern of aftershocks indicates the faults had alternating activity.

(3) The Challis segment and Lone Pine fault both show evidence of Quaternary offset which may suggest that one fault does not dominate over the other.

Conjugate normal faulting may be a mechanism for the style of faulting at the fault terminations near the northwestern ends of the Lost River, Lemhi, and Beaverhead faults where they intersect with the trans-Challis fault system. Contemporaneous activity along conjugate normal faults provides a way of distributing slip along two faults, thus decreasing the topography near the northwestern ends of the ranges.

Comparisons of the conjugate normal faulting observed for the 1984 Devil Canyon sequence with two other normal faulting sequences, as well as other reported conjugate strike-slip and thrust sequences suggest that future conjugate faulting sequences will include these three characteristics: 1) contemporaneous and alternating activity between the conjugate faults; 2) a cause-and-effect relationship suggesting the faults are mechanically coupled; and 3) changes in stress resulting from slip along one fault that cause increased stress and subsequent slip along the conjugate fault. Factors that may determine whether a conjugate fault becomes active include the rupture direction, location of the initiating event, and the stress level on nearby pre-existing faults.

REFERENCES

Amadi, E.E. (1992). *The 1990 Nooksack Forks, Washington, earthquake sequence: Sequence geometry and temporal characteristics*, M.S. Thesis, Boise State University, Boise, Idaho, 103 p.

Anders, M.H., J.W. Geissman, L.A. Piety, and J.T. Sullivan (1989). Parabolic distribution of circumeastern Snake River Plain seismicity and latest Quaternary faulting: Migratory pattern and association with the Yellowstone hotspot, *J. Geophys. Res.* **94**, 1589-1621.

Arabasz, W.J., R.B. Smith, and W.D. Richins (1979). Earthquake studies along the Wasatch Front, Utah: Network monitoring, seismicity, and seismic hazards, *Earthquake Studies in Utah - 1850 to 1978*, W.J. Arabasz, R.B. Smith, and W.D. Richins, editors, University of Utah, 253-286.

Baldwin, E.M. (1951). Faulting in the Lost River Range area of Idaho, *Am. J. Sci.* **249**, 884-902.

Barrientos, S.E., R.S. Stein, and S.N. Ward (1987). Comparison of the 1959 Hebgen Lake, Montana and the 1983 Borah Peak, Idaho earthquakes form geodetic observations, *Bull. Seis. Soc. Am.* **77**, 784-808.

Bennett, E.H. (1986). Relationship of the trans-Challis system in central Idaho to Eocene and Basin and Range extensions, *Geology* **14**, 481-484.

Bernard, P. and A. Zollo (1989). The Irpinia (Italy) 1980 Earthquake: Detailed analysis of a complex normal faulting, *J. Geophys. Res.* **94**, 1631-1647.

Blackwell, D. D., S. Kelley, and J.L. Steele (1992). *Heat flow modeling of the Snake River Plain*, EG&G Idaho, Inc., Idaho Falls, Idaho Informal Report **EGG-C91-103450**, 109 p.

Boatwright, J. (1985). Characteristics of the aftershock sequence of the Borah Peak, Idaho earthquake determined from digital recordings of the events, *Bull. Seis. Soc. Am.* **75**, 1265-1284.

Boatwright, J. and G.L. Choy (1985). Teleseismic estimates of the energy radiated by shallow earthquakes, in *Proceedings of Conference XXVIII on the Borah Peak, Idaho Earthquake*, U. S. Geol. Surv. Open-File Rept. **85-290**, 408-448.

Bowman, J.R. (1991). Geodetic evidence for conjugate faulting during the 1988 Tennant Creek, Australia earthquake sequence, *Geophys. J. Int.* 107, 47-56.

Bowman, J.R., G. Gibson, and T. Jones (1990). Aftershocks of the 1988 January 22 Tennant Creek, Australia intraplate earthquakes: Evidence for a complex thrust fault geometry, *Geophys. J. Int.* 100, 87-97.

Bruhn, R.L., P.R. Gibler, and W.T. Parry (1987). Rupture characteristics of normal faults: An example from the Wasatch fault zone, Utah, *Geol. Soc. Spec. Publ. London* 28, 337-353.

Bruhn, R.L., Z. Yang, D. Wu, and W.A. Yonkee (1991). Structure of the Warm Spring and northern Thousand Springs fault segments, Lost River fault zone, Idaho: Possible effects on rupturing during the 1983 Borah Peak earthquake, *Tectonophysics* 200, 33-49.

Bruhn, R.L., W.A. Yonkee, and W.T. Parry (1990). Structural and fluid-chemical properties of seismogenic normal faults, *Tectonophysics* 175, 139-157.

Bullen, K.E. and B.A. Bolt (1985). *An Introduction to the Theory of Seismology*, Cambridge University Press, New York, 499 pp.

Chen, W.P. and P. Molnar (1983). Focal depths of intracontinental and intraplate earthquakes and their implications for the thermal and mechanical properties of the lithosphere, *J. Geophys. Res.* 88, 4183-4214.

Choy, G.L., J. Boatwright, J.W. Dewey, and S.A. Sipkin (1983). A teleseismic analysis of the New Brunswick earthquake of January 9, 1982, *J. Geophys. Res.* 88, 2199-2212.

Choy, G.L. and J.R. Bowman (1990). Rupture process of a multiple main shock sequence: Analysis of teleseismic, local, and field observations of the Tennant Creek, Australia, earthquakes of January 22, 1998, *J. Geophys. Res.* 95, 6867-6882.

Choy G.L. and R. Kind (1987). Rupture complexity of a moderate-sized (m_b 6.0) earthquake: Broadband body-wave analysis of the North Yemen earthquake of 13 December 1982, *Bull. Seis. Soc. Am.* 77, 28-46.

Corbett, E.J. (1984). *Seismicity and crustal structure studies of southern California: Tectonic implications from improved earthquake locations*, Ph.D. Thesis, California Institute of Technology, Pasadena, California.

Crone, A.J. and K.M. Haller (1991). Segmentation and coseismic behavior of Basin and Range normal faults: Example from east-central Idaho and southwestern Montana, *J. Struct. Geol.* 13, 151-164.

Crone, A. J., M. N. Machette, M. G. Bonilla, J. J. Lienkaemper, K. L. Pierce, W. E. Scott, and R. C. Bucknam (1987). Surface faulting accompanying the Borah Peak earthquake and segmentation of the Lost River fault, central Idaho, *Bull. Seis. Soc. Am.* 77, 739-770.

Crosson R.S., M. Martini, R. Scarpa, and S.C. Key (1986). The southern Italy earthquake of 23 November 1980: An unusual pattern of faulting, *Bull. Seis. Soc. Am.* 76, 381-394.

Davis, G.H. (1984). *Structural geology of rocks and regions*, John Wiley and Sons, New York.

Das, S. and C. Scholz (1981). Off-fault aftershock clusters caused by shear stress increase?, *Bull. Seis. Soc. Am.* 71, 1699-1675.

Das, S. and C. Scholz (1983). Why large earthquakes do not nucleate at shallow depths, *Nature* 305, 621-623.

Dietz, L.D. and W.L. Ellsworth (1990). The October 17, 1989 Loma Prieta, California, earthquake and its aftershocks: Geometry of the sequence form high-resolution locations, *Geophys. Res. Letters* 17, 1417-1420.

Dobrin, M.B. (1976). *Introduction to geophysical prospecting*, McGraw Hill, New York.

Doser, D.I. (1990). A re-examination of the 1947 Manix, California, earthquake sequence and comparison to other sequences within the Mojave block, *Bull. Seis. Soc. Am.* 80, 267-277.

Doser, D. I. and R. B. Smith (1985). Source parameters of the 28 October 1983 Borah Peak, Idaho earthquake from body wave analysis, *Bull. Seis. Soc. Am.* 75, 1041-1051.

Doser, D.I. and R.B. Smith (1989). An assessment of source parameters of earthquakes in the Cordillera of the western United States, *Bull. Seis. Soc. Am.* 79, 1383-1409.

Fisher, F.S., D.H. McIntyre, and K.M. Johnson (1983). Geologic Map of the Challis 1° x 2° quadrangle, Idaho, *U.S. Geol. Surv. Open-File Rept.* 83-523, scale 1:250,000.

Freund, R. (1974). Kinematics of transform and transcurrent faults, *Tectonophysics* 21, 93-134.

Gephart, J.W. and D.D. Forsyth (1985). On the state of stress in New England as determined from earthquake focal mechanisms, *Geology* 13, 70-72.

Hait, M.H. Jr. and W.E. Scott (1978). Holocene faulting, Lost River Range, Idaho, *Geol. Soc. Am., Abs. with Prog.* 10, 217.

Herrin, E. (1968). Time of P, *Bull. Seis. Soc. Am.* 58, 1196-1219.

Hobbs, S.W., W.H. Hays, and D.H. McIntyre (1991). Geologic map of the Bayhorse area, central Custer county, Idaho, *U.S. Geol. Surv. Misc. Invest. Ser. Map* I-1882, scale 1:62,500.

Horsfield, W.T. (1980). Contemporaneous movement along crossing conjugate normal faults, *J. Struct. Geol.* 2, 305-310.

Hough, S.E. and L.E. Jones (1993). The 1992 Landers Sequence: Putting the pieces together, *EOS Trans. Am. Geophys. Union* 74, 429.

Hudnut, K., L. Seeber, and J. Pacheco (1989a). Cross-fault triggering in the November 1987 Superstition Hills earthquake sequence, southern California, *Geophys. Res. Lett.* 16, 199-202.

Hudnut, K., L. Seeber, T. Rockwell, J. Goodmacher, R. Klinger, S. Lindvall, and R. McElwain (1989b). Surface ruptures on cross-faults in the 24 November 1987 Superstition Hills, California earthquake sequence, *Bull. Seis. Soc. Am.* 79, 282-296.

Jackson, S.M., Wong, I.G., Carpenter, G.S., Anderson, D.M., and Martin, S.M. (1993). Contemporary seismicity in the eastern Snake River Plain, Idaho based on microearthquake monitoring, *Bull. Seis. Soc. Am.* 83, 680-695.

Janecke, S. (1993). Structures in segment boundary zones of the Lost River and Lemhi faults, east central Idaho, *J. Geophys. Res.* 98, 16223-16238.

Johnson, C.E. and D.M. Hadley (1976). Tectonic implications of the Brawley earthquake swarm, Imperial Valley, California, January 1975, *Bull. Seis. Soc. Am.* 66, 1133-1144.

Jones, L.E. and S.E. Hough (1993). Rupture characteristics of the June 28, 1992 Big Bear sequence from TERRAscope records, *EOS Trans. Am. Geophys. Union* 74, 429.

Jones, L.E. and S.E. Hough (1994). Analysis of broadband records from the June 28, 1992 Big Bear earthquake: Evidence of a multiple-event source, *Bull. Seis. Soc. Am.* (in press).

King, G. (1983). The accommodation of large strains in the upper lithosphere of the earth and other solids by self-similar fault systems: The geometrical origin of b-value, *Pageoph* 121, 761-815.

Klein, F. W. (1989). User's Guide to HYPOINVERSE, a program for VAX computers to solve for earthquake locations and magnitudes, *U.S. Geol. Surv. Open-File Rept.* 89-314, 58 pp.

Langer, C.J., G.A. Bollinger, and H.M. Merghelani (1987). Aftershocks of the 13 December 1982 North Yemen earthquake: Conjugate normal faulting in an extensional setting, *Bull. Seis. Soc. Am.* **77**, 2038-2055.

Machette, M.N., S.F. Personius, A.R. Nelson, D.P. Schwartz, and W.R. Lund (1991). The Wasatch fault zone, Utah: Segmentation and history of Holocene earthquakes, *J. Struct. Geol.* **13**, 137-150.

Magistrale, H., L. Jones, and H. Kanamori (1989). The Superstition Hills, California earthquakes of 24 November 1987, *Bull. Seis. Soc. Am.* **79**, 239-251.

McIntyre, D.H., E.B. Ekren, and R.F. Hardyman (1982). Stratigraphic and structural framework of the Challis volcanics in the eastern half of the Challis 1° x 2° quadrangle, Idaho, in *Cenozoic Geology of Idaho*, B. Bonnichsen and R.M. Breckenridge, editors, Idaho Department of Lands Bureau of Mines and Geology Bulletin **26**, 3-22.

Mandl, G. (1988). *Mechanics of Tectonic Faulting*, Elsevier Science Publishers, New York, 407 p.

Mendoza, C. and S.H. Hartzell (1988). Aftershock patterns and mainshock faulting, *Bull. Seis. Soc. Am.* **78**, 1438-1449.

NEIS (1984a). National Earthquake Information Service preliminary determination of epicenters, *U.S. Geol. Surv.*, August.

NEIS (1984b). National Earthquake Information Service preliminary determination of epicenters, *U.S. Geol. Surv.*, September.

Pho, H. and L. Behe (1972). Extended distances and angles of incidence of P waves, *Bull. Seis. Soc. Am.* **62**, 885-902.

Pierce, K. L. and L. A. Morgan (1992). The track of the Yellowstone hotspot: Volcanism, faulting, and uplift, in *Regional Geology of Eastern Idaho and Western Wyoming*, Link, P. K., Kuntz, M. A., and Platt, L. B. editors, Geol. Soc. Am. Memoir **179**, 1-53.

Priestly, K.F., K.D. Smith, and R.S. Cockerham (1988). The 1984 Round Valley, California earthquake sequence, *Geophys. J.* **95**, 215-235.

Qamar, A., and J. Zollweg (1990). The 1990 Deming, Washington earthquakes: A sequence of shallow thrust earthquakes in the Pacific Northwest, *EOS Trans. Am. Geophys. Union* **71**, 1145.

Reasenberg, P. A. and D. Oppenheimer (1985). FPFIT, FPPLOT, and FPPAGE: FORTRAN computer programs for calculating and displaying earthquake fault plane solutions, *U.S. Geol. Surv. Open-File Rept.* **85-739**, 109 p.

Rember, W.C. and E.H. Bennett (1979). Geologic map of the Dubois quadrangle, Idaho, *U.S. Geol. Open-file Rept.*, scale 1:250,000.

Richins, W. D., J. C. Pechmann, R. B. Smith, C. J. Langer, S. K. Goter, J. E. Zollweg, and J. J. King (1987). The 1983 Borah Peak, Idaho earthquake and its aftershocks, *Bull. Seis. Soc. Am.* **77**, 694-723.

Richter, C.F. (1958). *Elementary Seismology*, Freeman and Company, San Francisco, California, 768 p.

Richter, C.F. and J.M. Nordquist (1951). Instrumental study of the Manix earthquakes, *Bull. Seis. Soc. Am.* **41**, 347-388.

Ruppel, E. T. (1982). Cenozoic block uplifts in east-central Idaho and southwest Montana, *U.S. Geol. Surv. Prof. Paper* 1224, 24 p.

Scholz, C. (1982). Scaling laws for large earthquakes: Consequences of physical models, *Bull. Seis. Soc. Am.* **72**, 1-14.

Scholz, C. (1990). *The mechanics of earthquakes and faulting*, Cambridge University Press, 439 p.

Schwartz, D.P. and A.J. Crone (1988). Paleoseismicity of the Lost River fault zone, Idaho: Earthquake recurrence and segmentation, *Geol. Soc. Am., Abs. with Prog.* 20, 228.

Scott, W. E., K. L. Pierce, and M. H. Hait, Jr. (1985). Quaternary tectonic setting of the 1983 Borah Peak earthquake, central Idaho, *Bull. Seis. Soc. Am.* **75**, 1053-1066.

Shemeta, J.E. (1989). *New analyses of three-component digital data for aftershocks of the 1983 Borah Peak, Idaho, earthquake: Source parameters and refined hypocenters*, M.S. Thesis, University of Utah, Salt Lake City, Utah, 126 p.

Sibson, R.H. (1982). Fault zone models, heat flow, and the depth distribution of earthquake in the continental crust of the United States, *Bull. Seis. Soc. Am.* **72**, 151-163.

Sibson, R.H. (1987). Effects of fault heterogeneity on rupture propagation, in *Directions in Paleoseismology*, A.J. Crone and E.M. Omdahl, editors, U.S. Geol. Surv. Open-file Rept. **87-673**, 362-373.

Sibson, R.H. (1989). Earthquake faulting as a structural process, *J. Struct. Geol.* **11**, 1-14.

Smith, R.B. and R.L. Bruhn (1984). Intraplate extensional tectonics of the eastern Basin-Range: Inferences on structural style from seismic reflection data, regional tectonics, and thermal-mechanical models of brittle-ductile deformation, *J. Geophys. Res.* **89**, 5733-5762.

Smith, R.B., W.D. Richins, and D.I. Doser (1985). The 1983 Borah Peak, Idaho earthquake: Regional seismicity, kinematics of faulting, and tectonic mechanism, in *Proceedings of Conference XXVIII on the Borah Peak, Idaho Earthquake*, U. S. Geol. Surv. Open-File Rept. 85-290, 236-263.

Smith, K.D. and K.F. Priestly (1988). The foreshock sequence of the 1986 Chalfant, California earthquake, *Bull. Seis. Soc. Am.* 78, 172-187.

Stein, R.S. and M. Lisowski (1983). The 1979 Homestead Valley earthquake sequence, California: Control of aftershocks and postseismic deformation, *J. Geophys. Res.* 88, 6477-6490.

Stickney, M.J. (1993). Seismicity and focal mechanisms of the central Centennial Tectonic belt, southwestern Montana and east-central Idaho, *Geol. Soc. Am., Abs. with Prog.* 25, 151.

Starr, A.T. (1928). Slip in a crystal and rupture in a solid due to shear, *Proc. Cambridge Philos. Soc.* 24, 489-500.

Susong, D.D., S.U. Janecke, and R.L. Bruhn (1990). Structure of a fault segment boundary in the Lost River fault zone, Idaho, and possible effect on the 1983 Borah Peak earthquake rupture, *Bull. Seis. Soc. Am.* 80, 57-68.

Ward, S.N. and S.E. Barrientos (1986). An inversion for slip distribution and fault shape from geodetic observations of the 1983, Borah Peak, Idaho earthquake, *J. Geophys. Res.* 91, 4909-4919.

Wells, D.L. and Coppersmith, K.J. (1994). Empirical relationships among magnitude, rupture length, rupture area, and surface displacement, *Bull. Seis. Soc. Am* (in press).

Westaway, R. (1992). Revised hypocentre and fault rupture geometry for the 1980 November 23 Campania-Basilicata earthquake in southern Italy, *Geophys. J. Int.* 109, 376-390.

Wetmiller, R.J., J. Adams, F.M. Anglin, H.S. Hagsegawa, and A.E. Stevens (1984). Aftershock sequences of the 1982 Miramichi, New Brunswick, earthquakes, *Bull. Seis. Soc. Am.* 74, 621-653.

Witkind, I. J. (1975). Preliminary map showing known and suspected active faults in Wyoming, *U.S. Geol. Surv. Open-file Rept.* 75-279, 36 p.

Yamashina, K. (1980). Induced earthquakes caused by preceding earthquakes, *EOS Trans. Am. Geophys. Union* 61, 292-293.

Zhang, P., D.B. Slemmons, and F. Mao (1991). Geometric pattern rupture, termination, and fault segmentation of the Dixie Valley-Pleasant Valley active normal fault system, Nevada, U.S.A, *J. Struct. Geol.* **13**, 165-176.

Zoback, M. L. and M. D. Zoback (1989). Tectonic stress field of the continental United States, in *Geophysical framework of the Continental United States*, Pakiser, L. C., and Mooney, W. D., editors, Geol. Soc. Am. Memoir **172**, 523-539.

Zollweg, J.E. and W.D. Richins (1985). Later aftershocks of the 1983 Borah Peak, Idaho earthquake and related activity in central Idaho, in *Proceedings of Workshop XXVIII on the 1983 Borah Peak, Idaho earthquake*, U.S. Geol. Surv. Open-File Rept. **85-290**, 345-367.

APPENDIX A

Tables

Tables contained in this appendix list: 1) time differences; 2) polarities, elevation corrections, and station delays; and 3) dates of seismograms analyzed in this study. Time differences (Δt_1 & Δt_2) for the University of Utah Seismograph Stations and Idaho National Engineering Laboratory stations were measured from the seismograms and calculated using:

$$\Delta t_i = t_{WWV} - t_{clock}$$

where Δt_i is the time difference (s) and i = 1 or 2; t_{WWV} is the WWV reference time (s); and t_{clock} is the time of seismograph clock (s). The sign of the time differences for the U.S. Geological Survey (USGS) stations (see Table 1 in text) are opposite those noted on the seismograms because personnel noted the error observed between the time of the seismograph clock and the WWV reference time. Errors different from the reading error 0.001 s for USGS stations are the standard deviation from the mean of the estimated time difference. They were derived from using an average drift rate (see text, page 17).

Time Differences

Station Code	Date (yr-mn-dy)	Time (hr-min)	Δt_i (s)	Reading Error (s)
AIL	840826	1802	-0.051	0.001
AIL	840828	1554	-0.220	0.001
AIL	840828	1558	-0.055	0.001
AIL	840830	1515	-0.068	0.001
AIL	840901	1444	-0.079	0.001
AIL	840903	1434	-0.105	0.001
AIL	840905	1426	-0.120	0.001
AIL	840905	2110	-0.123	0.011
AIL	840907	1901	-0.100	0.001
AIL	840908	0400	-0.104	0.012
AIL	840909	1524	-0.100	0.001
AIL	840911	1509	-0.128	0.001
AIL	840911	1512	-0.128	0.001
AIL	840911	1720	-0.129	0.001
AND	840826	1713	-0.289	0.036
AND	840828	1509	-0.235	0.001
AND	840828	1512	-0.072	0.001
AND	840830	1439	-0.055	0.001
AND	840830	1443	-0.100	0.001
AND	840901	1400	-0.005	0.001
AND	840901	1414	-0.140	0.001
AND	840903	1401	-0.058	0.001
AND	840903	1405	-0.120	0.001
AND	840905	1357	-0.062	0.001
AND	840905	1401	-0.120	0.001
AND	840907	1506	-0.060	0.001
AND	840907	1510	-0.100	0.001
AND	840909	1430	-0.070	0.001
AND	840909	1434	-0.125	0.001
AND	840911	1431	-0.060	0.001
AND	840911	1434	-0.125	0.001
AND	840911	1438	-0.100	0.001
AND	840914	1751	-0.019	0.001
ANT	840825	2106	-0.060	0.001
ANT	840827	1906	-0.275	0.001
ANT	840827	1918	-0.058	0.001
ANT	840829	1746	-0.110	0.001
ANT	840831	1638	-0.175	0.001
ANT	840831	1643	-0.070	0.001
ANT	840902	1749	-0.130	0.001
ANT	840902	1752	-0.080	0.001
ANT	840904	1558	-0.124	0.001
ANT	840904	1602	-0.096	0.001
ANT	840906	1911	-0.149	0.001
ANT	840906	1915	-0.099	0.001

Time Differences

Station Code	Date (yr-mn-dy)	Time (hr-min)	Δt_i (s)	Reading Error (s)
ANT	840908	1648	-0.165	0.001
ANT	840908	1651	-0.115	0.001
ANT	840910	1520	-0.171	0.001
ANT	840910	1531	-0.104	0.001
ANT	840912	1436	-0.161	0.001
ANT	840912	1440	-0.111	0.001
ANT	840914	1417	-0.164	0.001
BAH	840830	0131	-0.500	0.020
BAH	840830	2358	-0.500	0.020
BAH	840831	0011	-0.290	0.020
BAH	840901	1927	-0.300	0.020
BAH	840903	1818	-0.320	0.020
BAH	840905	1709	-0.390	0.020
BAH	840907	1641	-0.410	0.020
BAH	840909	2208	-0.430	0.020
BAH	840911	1619	-0.500	0.020
BAH	840912	1737	-0.500	0.020
BRA	840825	2303	-0.052	0.001
BRA	840827	1825	-0.220	0.001
BRA	840827	1832	-0.064	0.001
BRA	840829	1632	-0.080	0.001
BRA	840831	1528	-0.110	0.001
BRA	840831	1533	-0.060	0.001
BRA	840902	1546	-0.078	0.001
BRA	840904	1440	-0.100	0.001
BRA	840906	1446	-0.110	0.001
BRA	840908	1451	-0.130	0.001
BRA	840910	1411	-0.108	0.001
BRA	840912	1325	-0.170	0.001
BRA	840912	1333	-0.085	0.001
BRA	840914	1322	-0.110	0.001
BSG	840826	2128	2.900	0.020
BSG	840827	2355	2.800	0.020
BSG	840828	0019	-0.250	0.020
BSG	840829	0007	-0.400	0.020
BSG	840831	2256	-0.380	0.020
BSG	840901	1826	-0.350	0.020
BSG	840903	1644	-0.300	0.020
BSG	840905	1633	-0.250	0.020
BSG	840907	1558	-0.200	0.020
BSG	840909	1742	-0.180	0.020
BSG	840911	1703	-0.400	0.020
BSG	840912	1647	-0.400	0.020

Time Differences

Station Code	Date (yr-mn-dy)	Time (hr-min)	Δt_i (s)	Reading Error (s)
CNF	840829	2203	-0.072	0.001
CNF	840831	1917	-0.080	0.001
CNF	840902	1502	-0.100	0.001
CHS	840825	1912	-0.052	0.001
CHS	840827	1752	-0.275	0.001
CHS	840827	1758	-0.080	0.001
CHS	840829	1703	-0.140	0.001
CHS	840829	1707	-0.060	0.001
CHS	840831	1557	-0.118	0.001
CHS	840831	1602	-0.070	0.001
CHS	840902	1631	-0.125	0.001
CHS	840902	1638	-0.077	0.001
CHS	840904	1513	-0.160	0.001
CHS	840904	1517	-0.080	0.001
CHS	840906	1638	-0.124	0.001
CHS	840906	1634	-0.090	0.001
CHS	840908	1523	-0.147	0.001
CHS	840908	1527	-0.097	0.001
CHS	840910	1437	-0.175	0.001
CHS	840910	1443	-0.108	0.001
CHS	840912	1354	-0.197	0.001
CHS	840912	1402	-0.081	0.001
CHS	840914	1556	-0.220	0.001
DAG	840828	1948	-0.410	0.020
DAG	840901	0019	-0.600	0.020
DAG	840903	2312	-0.670	0.020
DAG	840905	2005	-0.720	0.020
DAG	840907	1907	-0.800	0.020
DAG	840909	2005	-0.880	0.020
DAG	840911	1520	-0.500	0.020
DAG	840912	1558	-0.550	0.020
DBS	840826	2032	-0.062	0.001
DBS	840828	1752	-0.072	0.001
DBS	840830	1626	-0.100	0.001
DBS	840901	1558	-0.100	0.001
ELK	840829	1946	-0.070	0.001
ELK	840830	1728	-0.135	0.001
ELK	840830	1732	-0.070	0.001
ELK	840901	1655	-0.055	0.001
GVC	840902	1933	1.600	0.020
GVC	840903	2206	1.620	0.020
GVC	840903	2218	2.400	0.020

Time Differences

Station Code	Date (yr-mn-dy)	Time (hr-min)	Δt_i (s)	Reading Error (s)
GVC	840904	1821	2.420	0.020
GVC	840904	1837	3.280	0.020
GVC	840906	1747	3.380	0.020
GVC	840908	1750	3.350	0.020
GVC	840908	1756	3.200	0.020
GVC	840909	2038	3.240	0.020
GVC	840910	2122	3.260	0.020
GVC	840911	2109	3.290	0.020
LEG	840902	2110	2.520	0.020
LEG	840904	2015	2.500	0.020
LEG	840906	1911	2.500	0.020
LEG	840908	2032	2.490	0.020
LEG	840909	1913	2.460	0.020
LEG	840910	1522	2.450	0.020
LEG	840911	1542	2.450	0.020
LPP	840826	2348	2.620	0.020
LPP	840827	1721	2.680	0.020
LPP	840828	2003	2.690	0.020
LPP	840830	1840	2.500	0.020
LPP	840831	2305	2.450	0.020
LPP	840902	2011	2.370	0.020
LPP	840904	1918	2.270	0.020
LPP	840906	1836	2.150	0.020
LPP	840908	1858	2.060	0.020
LPP	840909	2144	2.040	0.020
LPP	840910	2221	1.960	0.020
LPP	840911	2204	1.960	0.020
MAL	840912	2226	-0.075	0.001
MAL	840914	1514	-0.050	0.001
MCG	840828	1913	2.280	0.020
MCG	840830	1731	2.350	0.020
MCG	840831	0900	2.370	0.025
MCP	840829	2201	3.600	0.020
MCP	840830	1929	3.560	0.020
MCP	840901	2203	3.500	0.020
MCP	840903	1958	3.480	0.020
MCP	840905	1849	3.410	0.020
MCP	840907	1743	3.370	0.020
MCP	840909	1644	3.310	0.020
MCP	840912	0033	3.200	0.020

Time Differences

Station Code	Date (yr-mn-dy)	Time (hr-min)	Δt_i (s)	Reading Error (s)
MIL	840826	1939	-0.060	0.001
MIL	840828	1631	-0.019	0.016
MIL	840828	2303	-0.070	0.001
MIL	840830	1553	-0.040	0.001
MIL	840830	1556	-0.080	0.001
MIL	840901	1527	-0.030	0.001
MIL	840901	1530	-0.100	0.001
MIL	840903	1515	-0.055	0.001
MIL	840903	1519	-0.120	0.001
MIL	840905	1459	-0.078	0.001
MIL	840905	1502	-0.120	0.001
MIL	840907	1615	-0.075	0.001
MIL	840907	1617	-0.125	0.001
MIL	840909	1614	-0.087	0.001
MIL	840909	1618	-0.120	0.001
MIL	840911	1550	-0.066	0.001
MIL	840911	1551	-0.116	0.001
MIL	840914	1716	-0.048	0.001
MOR	840827	1649	-0.082	0.001
MOR	840829	1531	-0.064	0.001
MOR	840831	1425	-0.068	0.001
MOR	840902	1400	-0.045	0.001
MOR	840902	1406	-0.082	0.001
MOR	840904	1331	-0.060	0.001
MOR	840904	1338	-0.080	0.001
MOR	840905	1841	-0.075	0.001
MOR	840907	1414	-0.060	0.001
MOR	840907	1418	-0.110	0.001
MOR	840909	1335	-0.083	0.001
MOR	840909	1340	0.900	0.001
MOR	840911	1342	0.923	0.001
MOR	840911	1345	0.890	0.001
MOR	840912	1959	0.898	0.001
RCI	840826	1929	-0.300	0.020
RCI	840827	1902	-0.300	0.020
RCI	840827	1907	-0.380	0.020
RCI	840828	2317	-0.340	0.020
RCI	840830	2211	-0.320	0.020
RCI	840901	1716	-0.370	0.020
RCI	840903	1601	-0.400	0.020
RCI	840905	1600	-0.410	0.020
RCI	840907	1519	-0.420	0.020
RCI	840909	1652	-0.430	0.020
RCI	840911	1812	-0.480	0.020

Time Differences

Station Code	Date (yr-mn-dy)	Time (hr-min)	Δt_i (s)	Reading Error (s)
RED	840901	2130	-0.095	0.001
RED	840903	1948	-0.108	0.001
SCG	840828	2216	2.900	0.020
SCG	840829	2016	2.930	0.020
SCG	840829	2030	2.600	0.020
SCG	840831	1952	2.660	0.023
SCG	840901	2241	2.320	0.020
SCG	840903	2033	2.400	0.020
SCG	840905	1920	2.430	0.020
SCG	840907	1812	2.500	0.020
SCG	840909	1815	2.600	0.020
SCG	840911	1701	2.620	0.020
SHE	840910	1820	-0.102	0.001
SHE	840912	1516	-0.109	0.001
SHE	840914	1428	-0.107	0.001
SPB	840904	1805	-0.105	0.001
SPB	840905	1532	-0.120	0.001
SPB	840907	1647	-0.130	0.001
SPB	840907	1657	-0.080	0.001
SPB	840909	1657	-0.105	0.001
SPB	840909	1704	-0.080	0.001
SPB	840911	1622	-0.080	0.001
SPB	840914	1644	-0.110	0.001
SPC	840828	1816	2.350	0.020
SPC	840829	1749	2.400	0.020
SPC	840831	1828	2.510	0.020
SPC	840902	1628	2.600	0.020
SPC	840904	1747	2.680	0.020
SPC	840906	1621	2.780	0.020
SPC	840908	1706	2.800	0.020
SPC	840910	2015	2.920	0.020
SPC	840911	1911	2.950	0.020
SPR	840902	1953	-0.105	0.001
SPR	840904	1633	-0.125	0.001
SPR	840904	1636	-0.080	0.001
SPR	840906	1950	-0.097	0.001
SPR	840908	1603	-0.144	0.001
SPR	840908	1606	-0.110	0.001
SPR	840910	1630	-0.145	0.001
SPR	840910	1633	-0.094	0.001
SPR	840912	1604	-0.131	0.001
SPR	840914	1359	-0.151	0.001

Time Differences

Station Code	Date (yr-mn-dy)	Time (hr-min)	Δt_i (s)	Reading Error (s)
SUB	840823	0340	0.000	0.020
SUB	840824	1722	-0.200	0.020
SUB	840827	2246	-0.890	0.020
SUB	840829	1652	-1.200	0.020
SUB	840829	1704	-0.080	0.020
SUB	840831	1733	-0.310	0.020
SUB	840903	1638	-0.900	0.020
SUB	840905	1747	-1.310	0.020
SUB	840907	1753	-0.280	0.020
SUB	840910	1852	-0.900	0.020
SUB	840912	1743	-1.300	0.020
SUB	840914	1852	-1.700	0.020
THO	840825	2025	2.580	0.020
THO	840826	1658	2.560	0.020
THO	840827	1941	2.510	0.020
THO	840828	1618	2.500	0.020
THO	840830	1558	2.490	0.020
THO	840831	2035	2.480	0.020
THO	840902	1540	2.420	0.020
THO	840904	1701	2.380	0.020
THO	840906	1544	2.310	0.020
THO	840910	1903	2.270	0.020
THO	840912	2014	2.200	0.020
WGR	840901	1854	-0.100	0.001
WGR	840903	1911	-0.105	0.001
WGR	840905	1916	-0.095	0.001
WGR	840906	1409	-0.082	0.001
WGR	840908	1339	-0.098	0.001
WGR	840910	1335	-0.108	0.001
WMS	840824	2025	-0.100	0.020
WMS	840827	2320	-0.310	0.020
WMS	840829	1733	-0.600	0.020
WMS	840831	1818	-0.850	0.020
WMS	840903	1551	-1.230	0.020
WMS	840905	1823	-1.510	0.020
WMS	840907	1829	-1.710	0.020
WMS	840907	1839	-0.200	0.020
WMS	840910	1940	-0.190	0.020
WMS	840912	1822	-0.500	0.020
WMS	840914	1936	-0.720	0.020

Polarities, Elevation Corrections, and Station Delays

Station Code	Polarity	Elevation Corrections[a] (s)	Station Delays[b] (s)
AIL	Normal	0.09	0.09 ± 0.02
AND	Normal	0.13	0.14 ± 0.04
ANT	Normal	0.03	0.00 ± 0.05
BAH	Normal	-0.02	0.08 ± 0.06
BRA	Normal	0.12	0.05 ± 0.04
BSG	Normal	0.11	-0.05 ± 0.03
CHS	Normal	0.14	-0.13 ± 0.02
CNF	Normal	0.13	0.02 ± 0.04
DAG	Normal	-0.04	0.09 ± 0.03
DBS	Normal	0.00	-0.07 ± 0.03
ELK	Normal	-0.03	0.00 ± 0.03
GVC	Reversed	0.04	-0.01 ± 0.04
LEG	Reversed	0.10	-0.07 ± 0.05
LPP	Reversed	0.07	0.04 ± 0.06
MAL	Normal	0.10	0.01 ± 0.04
MCP	Reversed	0.14	-0.07 ± 0.02
MCG	Reversed	-0.04	0.03 ± 0.03
MIL	Normal	0.05	0.00 ± 0.03
MOR	Normal	0.06	0.05 ± 0.04
RED	Normal	0.04	-0.05 ± 0.04
RCI	Reversed	0.07	-0.08 ± 0.04
SCG	Normal	0.14	-0.07 ± 0.02
SHE	Normal	-0.08	0.06 ± 0.04
SPB	Normal	-0.06	0.01 ± 0.02
SPC	Reversed	0.00	0.10 ± 0.03
SPR	Normal	0.00	0.09 ± 0.02
SUB	Normal	0.08	-0.03 ± 0.04
THO	Reversed	-0.01	-0.05 ± 0.05
WGR	Normal	0.08	-0.07 ± 0.07
WMS	Normal	0.11	-0.02 ± 0.03

a - Elevation delay determined using a datum elevation of 2000 m and a surface velocity of 3.38 km/s.
b - Mean and 1 standard deviation.

Dates of Seismograms Analyzed in this Study

Station	August									September													
Code	23	24	25	26	27	28	29	30	31	1	2	3	4	5	6	7	8	9	10	11	12	13	14
AIL				X	X	X	X	X	X	X	X	X	X	X		X		X	X	X			
AND				X	X	X	X	X	X	X	X	X	X	X	X	X	X	X	X	X	X	X	X
ANT			X	X	X	X	X	X	X	X	X	X	X	X	X	X	X	X	X	X	X	X	X
BAH								X	X	X	X	X	X	X		X	X	X	X	X	X		
BSG				X	X	X	X	X	X	X	X	X	X	X	X	X	X	X		X	X		
BRA			X	X	X	X	X	X	X	X	X	X	X	X	X	X	X	X	X	X	X	X	X
CHS			X	X	X	X	X	X	X	X	X	X	X	X	X	X	X	X	X	X	X	X	X
CNF							X	X	X	X	X												
DAG						X	X	X		X	X	X	X			X	X	X		X	X		
DBS				X	X	X	X	X	X	X													
ELK							X	X	X	X													
GVC											X	X	X	X	X	X	X	X	X	X			
LEG								X	X		X	X	X	X	X	X	X	X	X	X			
LPP				X	X	X	X	X	X	X	X	X	X		X	X	X	X	X	X			
MAL																					X	X	X
MCG			X	X		X	X	X	X														
MCP							X	X	X	X	X	X	X	X	X	X	X	X	X	X			
MIL				X	X	X	X	X	X	X	X	X	X	X	X	X	X	X	X	X	X	X	X
MOR					X	X	X	X	X	X	X	X	X	X	X	X	X	X	X	X	X		
RCI				X	X	X	X	X	X	X	X	X	X	X	X	X	X	X	X	X			

Dates of Seismograms Analyzed in this Study

Station	August									September													
Code	23	24	25	26	27	28	29	30	31	1	2	3	4	5	6	7	8	9	10	11	12	13	14
RED										X	X	X											
SCG						X	X	X	X	X	X	X	X	X	X	X	X	X	X	X			
SHE																			X	X	X	X	X
SPB													X	X	X	X	X	X	X	X	X	X	X
SPC						X	X	X	X	X	X	X	X	X	X	X	X	X	X	X			
SPR											X	X	X	X	X	X	X	X	X	X	X	X	X
SUB	X	X	X	X	X	X	X	X	X	X	X	X	X	X		X	X	X	X	X	X	X	X
THO			X	X	X	X	X	X	X	X	X	X	X	X	X		X	X	X	X			
WGR										X	X	X	X	X	X	X	X	X	X				
WMS		X	X	X	X	X	X	X	X	X	X	X	X	X	X	X	X	X	X	X	X	X	X

APPENDIX B

Velocity Model

Initially, the 1-D Borah Peak velocity model developed by Richins et al. (1987) was used to locate the earthquakes. A 1-D velocity model developed by Shemeta (1989) from inverting travel times of digitally recorded Borah Peak aftershocks was also used to locate the earthquakes. The boundary of the second layer in both these velocity models occurs at 6.95 km depth which extends through the center of the Devil Canyon hypocenters (see Figure 6 in text). Use of these models resulted in larger RMS errors than the model finally adopted, and caused P-wave arrivals that appeared as refracted waves to be calculated as direct waves on focal mechanisms. Thus, two complementary methods using blast and earthquake data were employed to examine the location of this boundary. The overall low resolution of the data only permitted evaluation of 1-D velocity models.

Blast Data

The first method used recordings of Thompson Creek Cyprus mine blasts located about 19 km southwest of Clayton, Idaho. P-wave arrival times were recorded by temporary seismic stations operated near the Devil Canyon epicentral area in 1988 and 1992 by the U. S. Geological Survey (USGS) and Boise State University (BSU), respectively (Figure B-1). Figure B-2 shows the arrival times of one 1988 and six 1992 Cyprus mine blasts. The surface velocity (V_o) was determined from evaluating arrival times recorded on four temporary seismographs located in a northeast-trending linear network shown in Figure B-1. In 1988, a seismograph (PIT) was placed within 30 m of the blast in the Cyprus mine pit to record the origin time. The next closest station (PHC) was

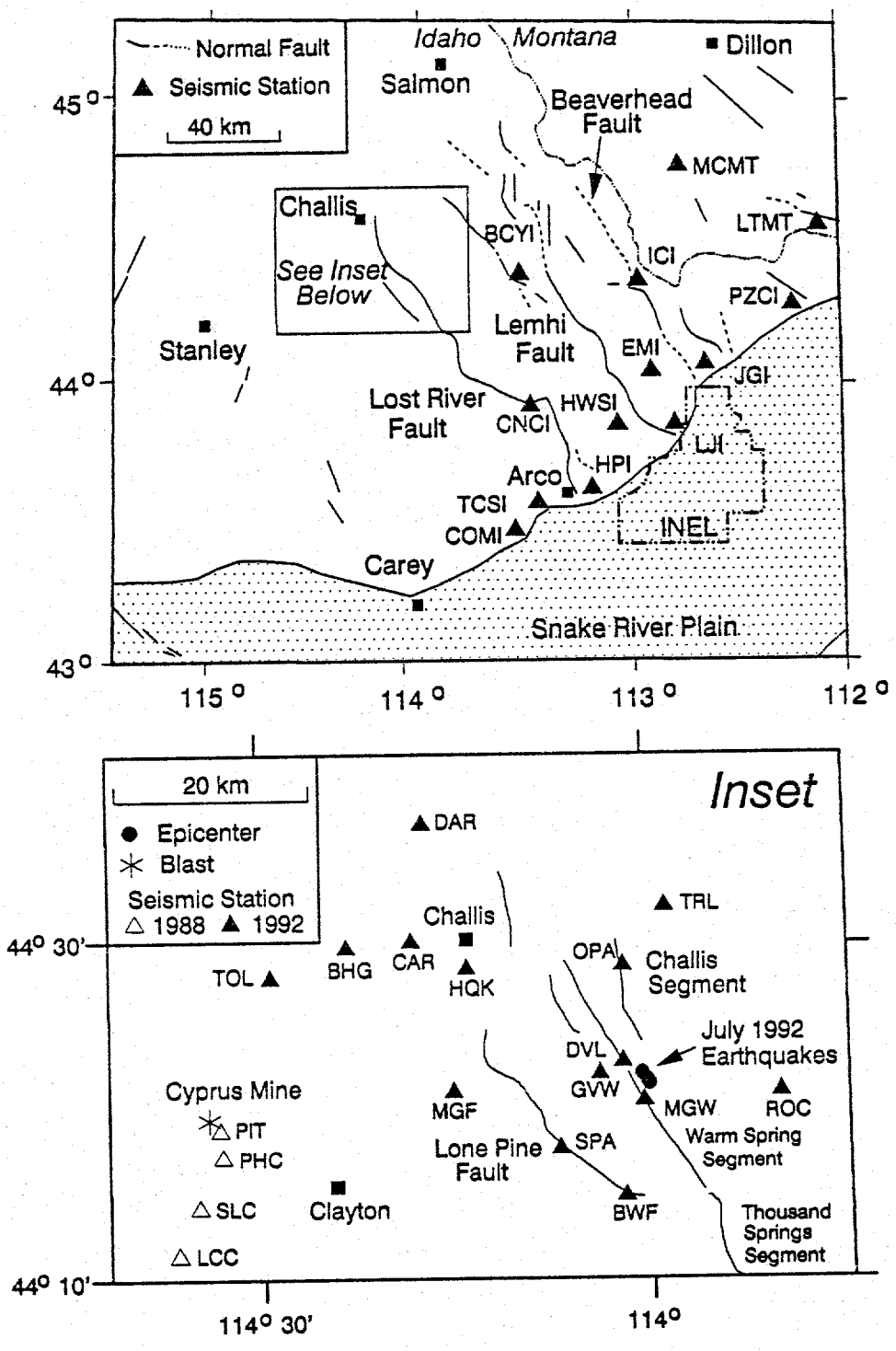

Figure B-1. Locations of seismic stations for: 1) Idaho National Engineering Laboratory and Montana Bureau of Mines and Geology (MBMG) seismic networks; 2) 1988 USGS temporary network; and 3) 1992 BSU network. Also shown is the location of the October 1988 and July 1992 Cyprus mine blasts, and July 1992 earthquakes. Locations for MBMG stations, BGMT, HBMT, and LRM (noted in Figure B-4) are not shown.

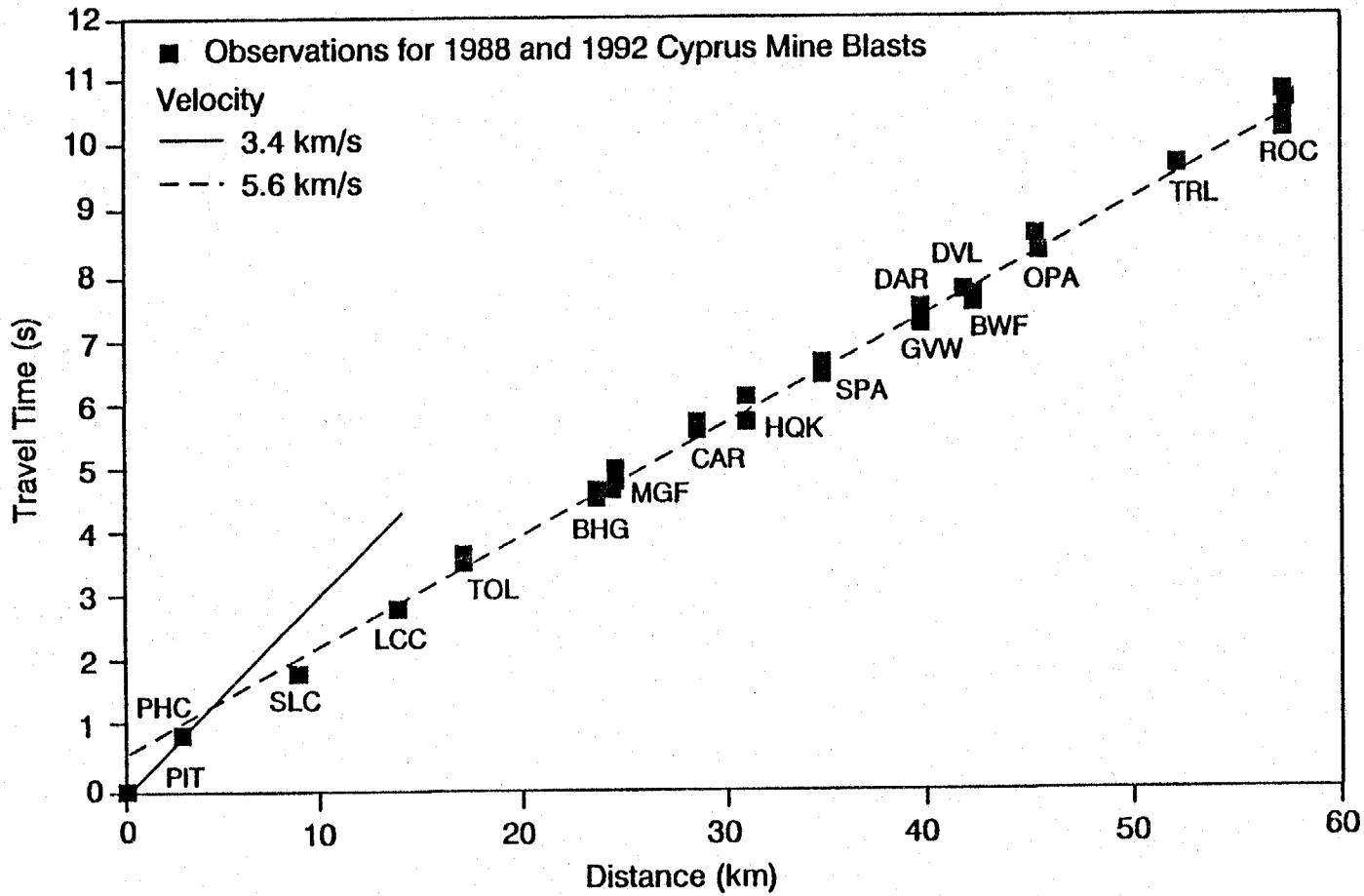

Figure B-2. Travel times of Cyprus mine blasts observed for the USGS 1988 and BSU 1992 temporary seismic stations. Travel times for the 1992 blasts were computed from estimating an origin time by fixing the location and restricting the depth to the surface. Lines for velocities 3.4 and 5.6 km/s were computed using a standard linear regression of the P-wave arrival times corrected for timing errors and elevation differences.

located about 3 km away and recorded a direct compressional wave. The other two stations, at distances of 9 and 14 km recorded a refracted wave (Figure B-2). Using the origin and arrival times of the stations in the pit and within 3 km, the surface velocity, V_o, was determined to be 3.4 $\pm$ 0.2 km/s.

The location for the blasts observed in 1992 is assumed to be the same as in 1988 since exact details of locations and elevations were unavailable from Cyprus mine personnel. It is estimated from 1988 to 1992 the elevation of blasts decreased from about 2200 to 2000 m. An average elevation of 2100 m was used to determine elevation corrections for seismographs observing blasts in both years. Elevation corrections for both 1988 and 1992 P-wave arrival times were determined using the surface velocity 3.4 km/s.

In 1992, a temporary network was installed close to the temporary network for the 1984 Devil Canyon sequence (Figure B-1). Good impulsive P-wave arrival times from refracted waves of the Cyprus mine blasts were observed on the 1988 and 1992 seismograms recorded at stations at distances of 17 to 52 km. Assuming a horizontal refractor, a linear regression applied to the arrival times for these stations resulted in a velocity of 5.6 $\pm$ 0.1 km/s for the second layer, V_1 (Figure B-2). Using V_o and V_1, an intercept time of 0.45 s, and a cross-over distance of 3.8 km (Figure B-2), Equations 1 and 2 (Dobrin, 1976) both result in 0.9 km for the thickness of the near-surface layer (Z_0).

$$Z_0 = \frac{T_i}{2} \frac{V_1 V_0}{\sqrt{V_1^2 - V_0^2}} \qquad [1]$$

$$Z_0 = \frac{X_c}{2}\sqrt{\frac{V_1 - V_0}{V_1 + V_0}} \qquad [2]$$

where Z_0 is the thickness of the first layer (km); T_i is the time (s) where the straight line of slope $1/V_1$ intercepts the time axis at a distance equal to zero; V_0 is the velocity of first layer (km/s); V_1 is the velocity of second layer (km/s); and X_c is the distance (km) where straight lines of slopes $1/V_0$ and $1/V_1$ cross (see Figure B-2).

An emergent arrival was observed on the ROC seismogram at a distance of 57.5 km indicating a cross-over may occur near this distance (Figure B-2). P-wave arrival times were obtained from the Idaho National Engineering Laboratory (INEL) and Montana Bureau of Mines and Geology (MBMG) regional seismic stations for the 1992 blasts. Their emergent arrivals made it difficult to estimate the velocity of the next layer.

Earthquake Data

For the second method, travel-time curves for direct and refracted waves were computed and compared to P-wave arrival times for three well-recorded earthquakes. P-wave arrival times were selected from a temporary local network operated by BSU during July 1992, and permanent stations of the INEL and MBMG seismic networks for the following earthquakes (Figure B-1): 1) M_L 4.1 on July 4, 1992 at 16:53 UTC; 2) M_L 3.4 on July 10, 1992 at 03:51 UTC; and 3) M_c 2.4 on July 11 at 04:00 UTC (M_L - MBMG station BUT; M_c - coda magnitude; M. Stickney, personal communications, 1994). Since the 1992 temporary network was well-balanced with four stations roughly equidistant from and surrounding the

epicenters, focal depths of the earthquakes at 16:53, 03:51, and 04:00 UTC were determined to be 7.7, 8.9, and 9.0 km, respectively, with little effect from the velocity model used in the location program.

The velocity of the third layer was determined by a linear regression of observed P-wave arrival times for distances of 27 to 110 km which resulted in a velocity (V_2) of 5.9 $\pm$ 0.2 km/s. To determine the thickness of the third layer, travel-time curves were computed for various direct and refracted wave paths originating at the earthquake hypocenters keeping Z_0 fixed at 0.9 km, V_0 at 3.4 km/s, and V_1 at 5.6 km/s (for equations see Dobrin, 1976). The depths of the lower boundary for the second (Z_1) and third (Z_2) layers, focal depths of the earthquakes (Z_e), V_2, and velocity of the fourth layer (V_3) were varied to determine the best fit to the observed P-wave arrival times. The best visual fit to the observations for direct waves resulted when: Z_e = 9.0 km; Z_1 = 8.5 km; and V_2 = 5.9 km/s (Figure B-3). The best visual fit to the observations for refracted waves occurred when: Z_e = 9.0 km; Z_1 = 8.5 km; Z_2 = 11.5 km; and V_3 = 6.16 km/s (Figure B-4). Although V_3 was varied, 6.16 km/s was the preferred velocity based on refraction studies used to develop the Borah Peak velocity model (Richins et al., 1987). For comparison, travel-time curves were computed for direct waves using the Borah Peak velocity models developed by Richins et al. (1987) and Shemeta (1989) (see Figure 6 in text). Figure B-3 shows that these velocity models do not match the observed arrival times at distances of 3 to 10 km.

To determine whether the third layer exists, travel-time curves for direct waves without Z_1 above and refracted waves with Z_1 below Z_e

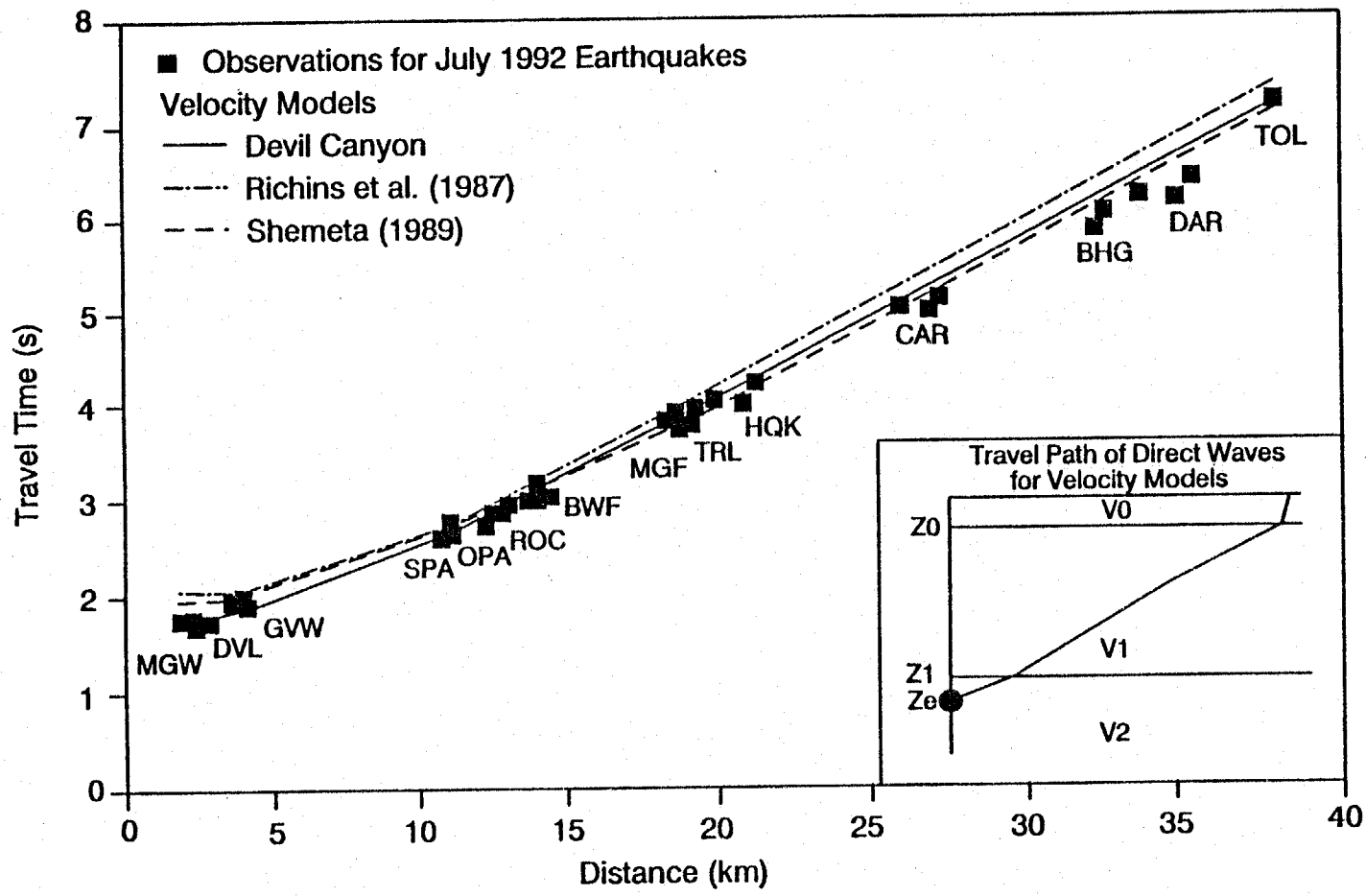

Figure B-3. Travel times of direct waves computed for the Devil Canyon and Borah Peak velocity models, and compared to the travel times observed at the BSU 1992 temporary seismic stations for earthquakes: 1) M_L 4.5 on July 4, 1992 at 16:53 UTC; 2) M_L 3.9 on July 10, 1992 at 03:51 UTC; and 3) M_L 3.2 on July 11 at 04:00 UTC.

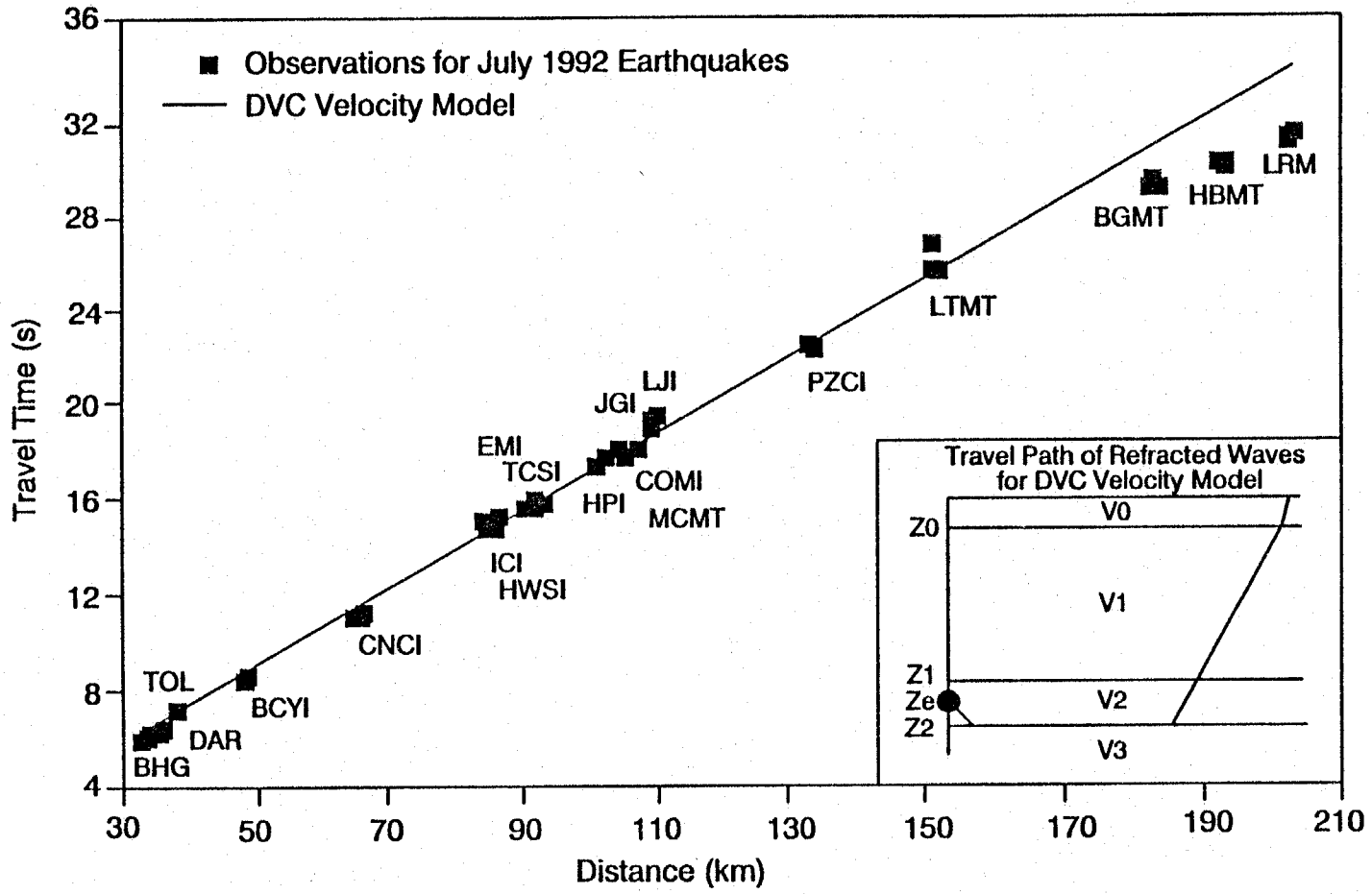

Figure B-4. Travel times of refracted waves computed for the Devil Canyon velocity model, and compared to the travel times observed at the BSU 1992 temporary and INEL regional seismic stations for earthquakes: 1) M_L 4.5 on July 4, 1992 at 16:53 UTC; 2) M_L 3.9 on July 10, 1992 at 03:51 UTC; and 3) M_L 3.2 on July 11 at 04:00 UTC.

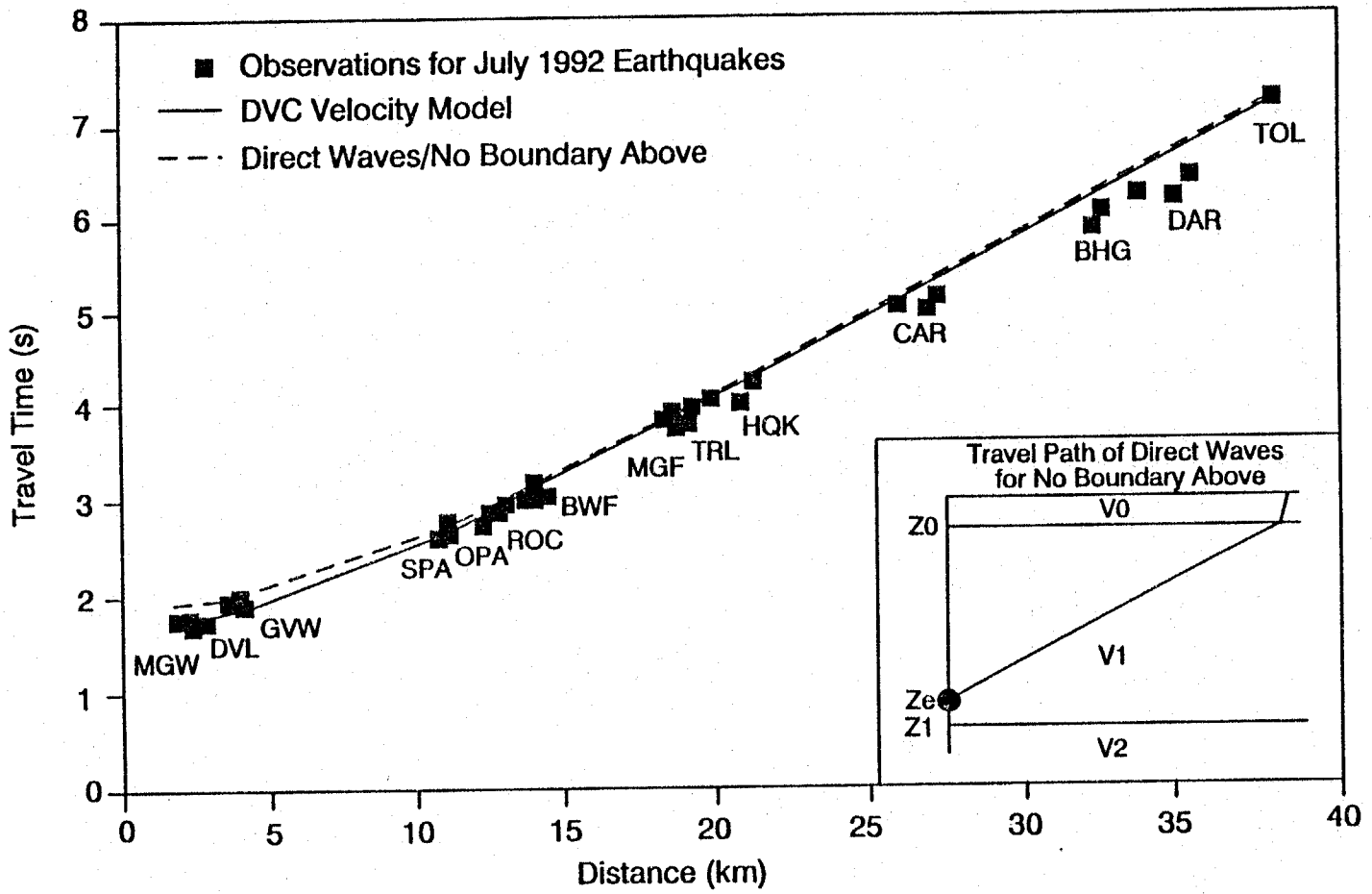

Figure B-5. Travel times of direct waves without the 5.6 and 5.9 km/s interface above the earthquake focal depth. Computed for the Devil Canyon and Borah Peak velocity models, and compared to the travel times observed at the BSU 1992 temporary seismic stations for earthquakes: 1) M_L 4.5 on July 4, 1992 at 16:53 UTC; 2) M_L 3.9 on July 10, 1992 at 03:51 UTC; and 3) M_L 3.2 on July 11 at 04:00 UTC.

were computed using the velocities and layer depths of the Devil Canyon velocity model. Figure B-5 shows that the travel times computed for the direct waves do not fit the observations at distances of 3 to 10 km. Figure B-6 shows that the travel times computed for the refracted waves do not fit the observations from 30 to 160 km. Significant changes have to be made to V_0 and V_1 to compute travel times that match the observations using the models without Z_1 above and with Z_1 below the focal depth of the earthquake.

In summary, the Devil Canyon velocity model developed from using the 1988 and 1992 blast data, and July 1992 earthquakes was chosen to locate the 1984 Devil Canyon earthquakes. The Borah Peak velocity models (Richins et al., 1987; Shemeta, 1989) were not used because they: 1) resulted in higher RMS errors when compared to the Devil Canyon velocity model; 2) calculated P-wave arrivals that had the characteristics of refracted waves as direct-wave ray paths, which had profound effects on focal mechanisms; and 3) did not fit the July 1992 earthquake P-wave arrival times computed for direct waves (Figure B-3).

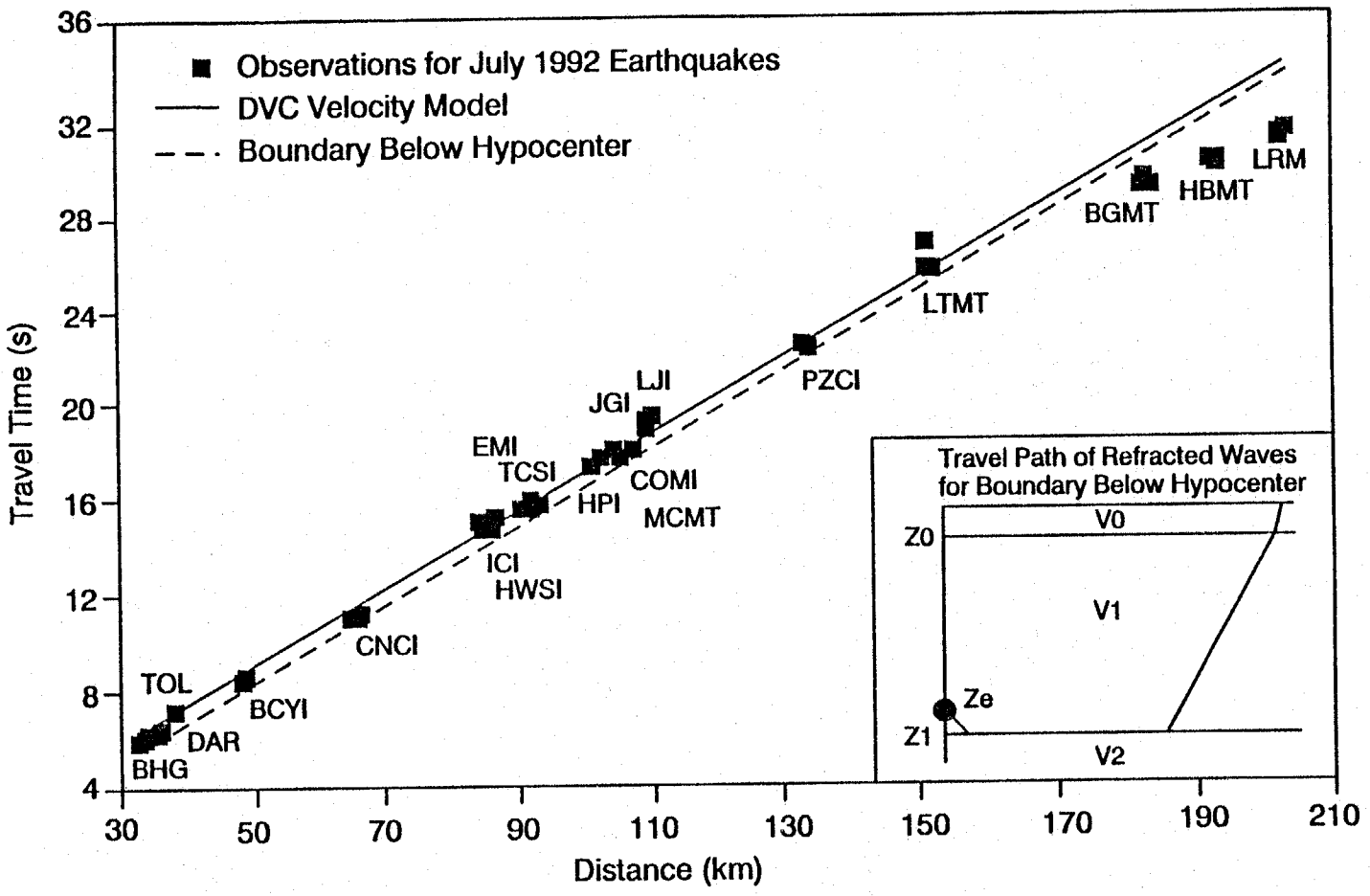

Figure B-6. Travel times of refracted waves without the 5.9 and 6.16 km/s interface below the earthquake focal depth. Computed for the Devil Canyon and Borah Peak velocity models, and compared to the travel times observed at the BSU 1992 temporary and INEL regional seismic stations for earthquakes: 1) M_L 4.5 on July 4, 1992 at 16:53 UTC; 2) M_L 3.9 on July 10, 1992 at 03:51 UTC; and 3) M_L 3.2 on July 11 at 04:00 UTC.

APPENDIX C

Summary List of 1984 Devil Canyon Earthquakes

Explanation of Earthquake List Headings

Heading	Example	Explanation
DATE	840827	Date of the earthquake: year (84), month (08), day (27).
ORIGIN	0133 37.71	Origin time of the earthquake: hour (01), minute (33), and seconds (37.71).
LAT N	44 22.16	Latitude of epicenter in degrees and minutes North.
LONG W	114 3.41	Longitude of epicenter in degrees and minutes West.
Z	10.72	Calculated focal depth (km).
MAG	1.13	Coda magnitude (M_c) of the earthquake as determined by HYPOINVERSE using the relation of Arabasz et al. (1979): $M_c = -3.13 + 2.74 \log \tau + 0.0012 \Delta$ where τ is the total signal duration (s) and Δ is the epicentral distance (km) from each station. M_L or m_b magnitudes were obtained from NEIS (1984a; 1984b).

Heading	Example	Explanation
NO	10	Number of station readings used in locating the
GAP	100	Largest azimuthal separation between stations (degrees).
DMIN	3.7	Distance (km) from the epicenter to the nearest station.
RMS	0.05	Root mean square error of time residuals (s) using all weights as calculated by: $$RMS=\sqrt{\frac{R_i^2}{NO}}$$ where R_i is the time residual (s) for the ith station.
ERH	0.7	Standard horizontal error of the epicenter (km).
ERZ	1.7	Standard vertical error of the focal depth (km).

DATE	ORIGIN	LAT N	LONG W	Z	MAG	NO	GAP	DMIN	RMS	ERH	ERZ
84 827	133 37.71	44 22.16	114 3.41	10.72	1.13	10	100	3.7	0.05	0.7	1.7
84 827	212 9.23	44 23.20	114 5.80	9.83	3.1 M_L	10	59	3.7	0.04	0.6	1.3
84 827	1629 38.65	44 19.75	114 3.63	11.54	1.65	9	120	8.2	0.09	0.7	2.2
84 828	2 8 41.51	44 24.77	114 5.17	9.28	1.16	12	73	2.7	0.06	0.5	0.9
84 828	1114 7.94	44 25.48	114 5.82	9.23	1.35	12	70	2.0	0.08	0.5	1.0
84 828	1119 43.44	44 25.55	114 5.86	9.72	3.1 M_L	12	70	1.8	0.08	0.6	1.0
84 828	1541 5.83	44 23.12	114 5.54	10.13	1.32	13	60	3.5	0.07	0.5	1.1
84 828	2040 30.15	44 25.76	114 5.68	8.58	3.4 M_L	16	71	1.6	0.06	0.4	0.8
84 828	21 2 15.28	44 25.58	114 5.56	9.31	1.54	15	72	4.0	0.08	0.5	1.0
84 828	2349 6.85	44 24.78	114 5.20	9.16	0.82	17	73	2.7	0.06	0.5	0.8
84 828	2353 29.11	44 25.47	114 5.68	9.23	0.43	11	120	5.8	0.10	0.7	1.5
84 829	3 4 25.80	44 23.87	114 5.10	10.41	1.33	17	47	2.4	0.06	0.5	0.9
84 829	452 13.34	44 23.16	114 5.50	10.47	1.27	18	36	3.4	0.06	0.4	0.9
84 829	553 2.37	44 25.40	114 5.42	8.68	0.72	17	42	2.3	0.07	0.4	0.8
84 829	627 42.98	44 25.50	114 5.47	8.95	1.74	18	43	2.1	0.06	0.4	0.8
84 829	632 12.00	44 25.39	114 5.62	9.12	0.76	17	71	2.2	0.07	0.4	0.8
84 829	730 40.80	44 23.38	114 5.78	10.06	2.02	18	35	3.6	0.06	0.4	0.9
84 829	936 10.85	44 23.18	114 4.68	10.87	1.01	17	55	2.6	0.07	0.5	1.0
84 829	947 51.13	44 20.10	114 5.46	7.91	3.3 M_L	14	66	4.2	0.09	0.6	1.4
84 829	951 14.11	44 20.03	114 5.17	8.57	1.78	18	62	4.2	0.09	0.5	0.9
84 829	15 9 18.18	44 23.80	114 4.44	9.06	1.70	17	58	1.6	0.05	0.4	0.8
84 829	1541 28.16	44 24.13	114 5.53	10.15	0.71	17	60	2.9	0.07	0.5	0.9
84 829	2012 57.27	44 23.25	114 4.68	10.46	0.89	17	54	2.5	0.08	0.5	0.9
84 829	23 5 7.78	44 26.54	114 6.29	8.23	0.92	20	70	0.2	0.06	0.4	0.8
84 830	0 6 56.87	44 25.96	114 5.48	7.92	0.00	20	70	1.5	0.07	0.4	0.8
84 830	010 32.21	44 25.78	114 5.72	7.29	0.86	19	68	1.5	0.04	0.4	0.9
84 830	017 25.50	44 23.26	114 4.44	10.46	1.43	18	59	2.2	0.07	0.6	0.9
84 830	338 6.96	44 20.00	114 5.44	7.45	0.93	21	58	4.0	0.09	0.4	1.2
84 830	611 35.23	44 23.85	114 5.92	9.24	1.34	20	60	3.5	0.08	0.4	0.8
84 830	8 0 3.67	44 23.72	114 5.09	8.14	0.70	18	60	2.5	0.07	0.4	1.0
84 830	823 43.80	44 23.80	114 5.24	8.63	1.73	20	59	2.6	0.06	0.4	0.7
84 830	1022 6.85	44 23.79	114 5.14	8.31	0.83	20	60	2.5	0.06	0.4	0.8
84 830	1111 53.28	44 25.67	114 5.79	7.83	0.30	20	67	1.6	0.07	0.4	0.8
84 830	1430 16.11	44 23.99	114 6.57	9.14	1.23	19	69	3.8	0.06	0.5	0.8
84 830	1514 23.64	44 24.59	114 6.53	9.11	1.40	20	61	3.5	0.05	0.4	0.8
84 830	1546 7.89	44 25.44	114 5.67	7.92	0.58	20	42	2.1	0.07	0.4	1.0
84 830	1842 27.34	44 23.93	114 6.68	9.22	3.5 M_L	20	57	3.6	0.05	0.4	0.8
84 830	21 6 20.87	44 23.85	114 6.59	9.81	3.9 M_L	20	37	3.7	0.06	0.4	0.8
84 830	2221 18.52	44 24.04	114 6.93	8.74	0.44	19	65	3.4	0.06	0.4	0.8
84 831	232 16.82	44 23.73	114 6.59	9.65	0.85	20	37	3.7	0.08	0.4	0.9
84 831	610 38.39	44 23.41	114 5.72	9.93	0.60	20	36	3.5	0.06	0.4	0.9
84 831	651 33.40	44 26.17	114 5.09	7.30	0.82	19	50	1.8	0.09	0.4	1.0
84 831	934 42.91	44 23.55	114 7.42	7.11	0.00	19	45	2.5	0.08	0.4	1.0
84 831	1451 38.59	44 23.03	114 4.48	9.69	1.03	17	95	2.6	0.06	0.5	1.0
84 831	1528 43.65	44 24.38	114 4.79	9.04	0.99	15	55	2.0	0.04	0.4	0.8
84 831	1536 5.31	44 24.28	114 6.56	8.11	0.47	17	55	4.0	0.08	0.4	1.0
84 831	1947 7.61	44 23.47	114 5.96	9.16	0.57	18	47	3.7	0.07	0.4	0.9
84 831	2041 46.00	44 23.58	114 4.17	8.61	0.62	18	48	1.5	0.07	0.4	0.8
84 831	2046 16.24	44 20.22	114 3.25	9.31	1.43	18	72	6.0	0.07	0.4	1.1
84 831	23 5 44.36	44 25.28	114 5.87	9.04	0.47	15	87	2.3	0.07	0.5	0.9
84 9 1	427 55.49	44 25.68	114 5.77	8.32	0.50	16	45	1.6	0.07	0.4	0.8
84 9 1	440 24.54	44 25.73	114 6.31	7.46	0.61	18	41	1.4	0.05	0.4	0.9
84 9 1	455 23.80	44 25.92	114 5.83	8.70	1.28	19	43	1.2	0.04	0.4	0.7
84 9 1	634 44.85	44 23.57	114 6.70	9.43	1.67	19	46	3.5	0.04	0.4	0.8
84 9 1	1040 40.44	44 25.30	114 5.27	8.53	0.72	18	43	2.6	0.09	0.4	0.8
84 9 1	11 1 7.52	44 23.65	114 6.57	9.51	0.86	19	47	3.7	0.04	0.4	0.8
84 9 1	1147 41.26	44 20.37	114 3.26	8.97	0.85	18	69	6.2	0.06	0.4	1.1
84 9 1	1411 18.22	44 24.64	114 5.21	10.46	3.1 M_L	19	42	2.6	0.04	0.4	0.8

DATE	ORIGIN	LAT N	LONG W	Z	MAG	NO	GAP	DMIN	RMS	ERH	ERZ
84 9 1	1716 17.50	44 23.55	114 6.10	9.45	0.55	15	80	3.8	0.04	0.5	0.9
84 9 1	1740 49.78	44 23.40	114 5.75	9.54	0.51	16	85	3.5	0.06	0.5	0.9
84 9 1	1817 40.40	44 23.26	114 3.67	7.31	0.94	17	95	1.7	0.07	0.5	1.1
84 9 1	2137 21.26	44 25.45	114 5.91	9.09	0.43	17	45	2.0	0.06	0.5	0.8
84 9 2	0 8 25.21	44 24.20	114 4.41	8.20	0.67	20	65	1.4	0.06	0.4	1.0
84 9 2	1012 6.13	44 23.44	114 3.68	6.82	0.82	20	94	1.4	0.05	0.4	1.0
84 9 2	21 1 21.91	44 24.69	114 5.35	8.75	0.57	20	53	2.9	0.04	0.4	0.8
84 9 2	1132 37.95	44 24.89	114 4.80	9.26	0.72	20	49	2.4	0.06	0.5	0.9
84 9 2	1513 44.92	44 24.03	114 4.11	5.54	0.58	19	83	1.1	0.05	0.4	1.0
84 9 2	1522 50.58	44 22.40	114 3.82	11.29	0.46	19	97	3.3	0.07	0.5	0.9
84 9 2	21 0 1.33	44 24.84	114 5.36	8.40	0.39	21	43	3.0	0.05	0.4	0.9
84 9 2	2133 17.01	44 24.64	114 5.29	8.85	0.50	22	48	2.7	0.06	0.4	0.8
84 9 2	2134 39.63	44 22.95	114 4.88	10.34	1.69	22	69	1.9	0.06	0.5	0.9
84 9 2	2157 47.44	44 23.34	114 5.71	9.36	1.03	20	85	3.5	0.04	0.5	0.9
84 9 2	2327 51.73	44 23.27	114 4.83	9.56	0.51	22	79	2.3	0.07	0.5	0.8
84 9 2	2355 32.99	44 23.18	114 5.65	9.05	0.62	21	61	2.9	0.06	0.5	0.8
84 9 3	322 16.07	44 23.81	114 5.53	8.59	0.64	22	65	3.0	0.05	0.4	0.7
84 9 3	610 40.36	44 20.74	114 3.95	8.12	0.68	20	101	2.8	0.08	0.5	1.1
84 9 3	644 47.52	44 22.42	114 4.11	10.14	0.46	20	72	0.4	0.07	0.5	1.0
84 9 3	947 23.09	44 23.59	114 4.61	9.28	0.92	19	90	2.0	0.05	0.5	0.9
84 9 3	1432 58.84	44 21.96	114 3.66	8.19	0.67	20	100	0.6	0.06	0.5	1.0
84 9 3	2011 28.06	44 20.03	114 3.38	9.42	0.78	20	105	4.2	0.06	0.5	0.9
84 9 3	2028 0.57	44 19.88	114 3.39	9.91	3.2 M_L	19	105	5.4	0.07	0.5	1.1
84 9 3	2040 49.61	44 25.57	114 5.58	8.76	0.44	21	52	1.9	0.04	0.4	0.7
84 9 4	0 0 29.84	44 22.78	114 3.59	8.26	0.71	22	97	1.0	0.06	0.5	0.9
84 9 4	019 51.83	44 23.41	114 6.93	8.28	0.67	22	44	3.2	0.03	0.4	0.9
84 9 4	134 17.57	44 23.28	114 6.85	7.33	0.55	22	45	3.3	0.07	0.4	0.9
84 9 4	236 49.87	44 25.33	114 5.40	8.88	0.49	22	50	2.4	0.07	0.4	0.8
84 9 4	254 16.05	44 23.19	114 4.41	9.09	0.60	22	92	1.9	0.05	0.4	0.8
84 9 4	550 41.04	44 26.13	114 5.06	7.59	3.7 M_L	22	65	1.8	0.04	0.4	0.9
84 9 4	557 21.52	44 26.34	114 5.09	7.58	3.1 M_L	22	66	1.7	0.05	0.4	0.9
84 9 4	6 2 27.10	44 26.26	114 4.98	7.05	0.00	21	67	1.9	0.04	0.4	0.9
84 9 4	611 27.61	44 26.10	114 5.23	7.74	1.25	19	62	4.4	0.07	0.5	1.2
84 9 4	649 13.20	44 26.28	114 5.29	7.16	0.94	22	63	1.4	0.07	0.4	0.9
84 9 4	7 5 0.24	44 26.13	114 5.01	7.07	0.76	22	66	1.9	0.05	0.4	0.9
84 9 4	747 48.56	44 23.34	114 5.03	9.45	1.01	21	75	2.5	0.07	0.5	0.9
84 9 4	8 4 34.95	44 26.30	114 4.96	6.13	0.28	22	68	1.9	0.06	0.4	1.0
84 9 4	845 13.67	44 26.27	114 4.93	6.61	1.12	21	68	1.9	0.04	0.4	0.9
84 9 4	10 5 17.61	44 22.42	114 3.93	10.80	1.19	21	97	0.3	0.04	0.5	0.8
84 9 4	1013 34.92	44 23.38	114 7.44	7.47	0.51	22	38	2.5	0.04	0.4	0.9
84 9 4	1218 38.17	44 26.09	114 5.12	7.31	1.11	21	64	1.8	0.05	0.4	0.9
84 9 4	1231 16.24	44 23.11	114 3.21	9.62	0.46	21	98	1.8	0.06	0.5	0.9
84 9 4	1231 52.84	44 23.27	114 6.75	8.49	0.81	22	47	3.4	0.05	0.4	0.7
84 9 4	1242 52.54	44 25.27	114 5.33	8.92	0.51	22	49	2.6	0.04	0.4	0.7
84 9 4	1340 46.93	44 25.28	114 5.45	8.62	0.66	22	48	2.5	0.04	0.4	0.7
84 9 4	1410 3.50	44 26.18	114 4.89	7.19	2.9 M_L	22	68	2.0	0.04	0.4	0.9
84 9 4	1511 41.54	44 24.70	114 5.36	10.54	1.99	22	46	2.9	0.03	0.4	0.8
84 9 4	1549 53.11	44 25.80	114 6.14	8.03	0.57	22	48	1.3	0.03	0.4	0.9
84 9 4	1629 32.22	44 26.20	114 4.90	7.05	0.60	21	68	2.0	0.05	0.4	0.9
84 9 4	2147 52.48	44 23.41	114 5.05	8.92	0.50	18	76	2.6	0.07	0.5	0.9
84 9 4	2314 33.06	44 23.80	114 4.53	9.55	0.57	22	67	1.7	0.05	0.4	0.8
84 9 5	022 46.87	44 25.82	114 5.85	8.59	1.06	21	68	1.4	0.05	0.4	0.7
84 9 5	033 53.20	44 26.17	114 5.05	7.44	0.79	19	72	1.8	0.04	0.4	0.9
84 9 5	053 33.18	44 26.16	114 5.03	7.36	1.40	22	46	1.8	0.03	0.4	0.9
84 9 5	358 5.23	44 24.11	114 4.70	8.07	0.45	21	65	1.8	0.05	0.4	0.9
84 9 5	436 39.57	44 22.46	114 4.00	8.83	1.42	21	70	0.4	0.04	0.4	0.8
84 9 5	5 0 58.53	44 25.58	114 5.53	7.87	0.52	21	67	2.0	0.07	0.4	0.9
84 9 5	528 36.53	44 25.02	114 5.43	7.87	0.56	21	65	2.9	0.05	0.4	0.9
84 9 5	925 27.99	44 22.49	114 3.93	8.58	0.63	21	97	0.4	0.03	0.4	0.7

DATE	ORIGIN	LAT N	LONG W	Z	MAG	NO	GAP	DMIN	RMS	ERH	ERZ
84 9 5	949 50.15	44 23.47	114 7.20	7.95	0.72	22	36	5.0	0.05	0.4	1.0
84 9 5	953 46.06	44 23.48	114 7.05	7.08	0.52	21	35	4.8	0.06	0.4	1.0
84 9 5	12 8 15.92	44 23.42	114 7.03	7.59	0.74	22	35	4.7	0.06	0.4	1.0
84 9 5	16 7 27.21	44 23.35	114 7.21	7.43	0.43	20	61	5.4	0.08	0.4	1.2
84 9 5	1643 48.61	44 26.10	114 4.92	7.55	1.75	21	46	2.0	0.05	0.4	1.0
84 9 5	1738 58.60	44 23.33	114 6.93	8.20	3.7 M_L	20	62	5.0	0.05	0.4	1.1
84 9 5	18 6 48.54	44 26.42	114 4.90	5.58	0.52	18	48	4.7	0.04	0.4	1.3
84 9 5	2010 2.94	44 23.41	114 6.95	7.77	1.62	17	62	5.0	0.04	0.4	1.2
84 9 6	517 39.20	44 22.11	114 3.68	8.63	1.46	16	78	3.8	0.04	0.5	1.0
84 9 6	751 18.17	44 23.14	114 5.76	9.63	0.45	17	67	3.7	0.04	0.5	1.0
84 9 6	947 30.52	44 21.37	114 4.10	10.36	0.61	15	79	7.1	0.07	0.5	1.5
84 9 6	1440 29.54	44 19.68	114 4.84	7.20	0.48	17	80	3.9	0.07	0.5	1.1
84 9 6	1646 59.72	44 23.51	114 4.07	9.70	0.31	14	85	2.3	0.07	0.5	1.3
84 9 6	1847 15.25	44 22.75	114 4.00	8.88	1.21	15	84	0.9	0.04	0.5	1.0
84 9 6	1950 21.81	44 24.01	114 5.07	7.87	3.0 M_L	16	62	2.3	0.04	0.4	1.1
84 9 6	20 7 57.02	44 23.24	114 7.58	8.15	0.29	16	61	2.3	0.07	0.5	1.1
84 9 6	2056 45.91	44 23.09	114 6.95	7.23	0.92	17	66	3.2	0.04	0.4	1.0
84 9 6	2127 48.14	44 23.78	114 4.79	8.14	0.66	17	66	2.1	0.06	0.5	1.1
84 9 6	2153 28.03	44 23.32	114 6.31	9.30	0.14	17	61	3.8	0.06	0.5	1.0
84 9 6	2234 57.95	44 23.26	114 5.97	10.03	0.46	17	61	3.4	0.05	0.5	1.0
84 9 7	148 30.16	44 24.43	114 6.60	9.00	0.11	17	60	4.1	0.05	0.5	0.9
84 9 7	423 41.27	44 22.30	114 3.93	11.40	0.25	17	71	0.1	0.08	0.5	1.0
84 9 7	622 26.84	44 23.47	114 4.97	9.39	0.39	17	58	2.5	0.07	0.5	1.0
84 9 7	628 37.78	44 23.40	114 5.18	10.97	0.42	16	52	2.7	0.04	0.5	0.9
84 9 7	718 15.32	44 24.85	114 5.26	9.74	0.30	17	65	2.9	0.09	0.5	1.1
84 9 7	742 20.17	44 23.63	114 8.42	6.18	0.45	17	59	1.3	0.08	0.5	1.1
84 9 7	830 41.14	44 22.87	114 4.17	7.98	0.58	16	76	1.2	0.05	0.5	1.1
84 9 7	926 28.66	44 22.47	114 3.89	8.17	0.45	16	91	0.4	0.05	0.5	1.0
84 9 7	2345 2.65	44 23.80	114 6.51	9.30	0.39	21	50	3.8	0.08	0.4	0.9
84 9 8	134 46.40	44 26.19	114 5.19	7.02	0.99	21	45	1.6	0.04	0.4	1.0
84 9 8	311 18.03	44 24.94	114 5.53	7.64	0.45	20	41	3.0	0.07	0.4	1.0
84 9 8	313 12.99	44 25.83	114 5.56	8.50	0.90	20	43	1.6	0.05	0.4	0.7
84 9 8	430 54.71	44 23.06	114 4.32	7.80	1.29	20	71	1.6	0.06	0.4	1.0
84 9 8	616 39.92	44 23.17	114 6.80	7.12	5.0 m_b	16	90	5.0	0.07	0.4	1.4
84 9 8	753 15.55	44 22.36	114 6.91	5.63	2.58	20	83	3.8	0.08	0.4	1.1
84 9 8	820 39.51	44 22.21	114 6.89	6.41	0.00	19	87	4.0	0.05	0.4	1.2
84 9 8	832 9.77	44 23.38	114 8.26	4.86	1.25	19	57	1.4	0.09	0.4	1.1
84 9 8	835 2.70	44 22.76	114 6.58	7.00	3.1 M_L	17	75	3.7	0.06	0.5	1.1
84 9 8	922 25.67	44 23.21	114 7.06	7.94	3.0 M_L	19	64	3.0	0.05	0.4	1.0
84 9 8	1033 54.36	44 27.00	114 6.37	8.52	0.51	19	72	1.0	0.05	0.4	0.8
84 9 8	1048 38.30	44 23.19	114 6.50	8.42	1.34	18	63	3.9	0.05	0.4	0.9
84 9 8	1139 36.45	44 23.46	114 7.56	7.31	0.00	18	62	5.4	0.09	0.5	1.3
84 9 8	1146 5.01	44 23.38	114 7.26	7.63	0.84	16	60	5.0	0.05	0.4	1.2
84 9 8	1222 3.11	44 21.79	114 6.76	5.60	1.00	19	96	3.9	0.10	0.5	1.2
84 9 8	1243 22.14	44 23.46	114 7.70	7.51	0.56	20	57	2.2	0.08	0.4	1.0
84 9 8	1333 1.48	44 23.30	114 7.51	6.52	0.73	20	61	2.4	0.07	0.4	1.0
84 9 8	14 4 33.39	44 23.30	114 6.78	7.56	1.87	19	61	4.3	0.05	0.4	1.1
84 9 8	14 5 52.32	44 22.17	114 7.27	5.53	1.12	16	107	3.6	0.08	0.5	1.3
84 9 8	1431 8.07	44 23.50	114 7.41	8.58	1.29	19	57	2.5	0.07	0.4	0.9
84 9 8	1452 38.86	44 23.17	114 7.75	6.77	1.47	19	62	2.2	0.02	0.4	1.0
84 9 8	15 2 11.58	44 22.63	114 7.55	5.87	0.85	19	73	2.8	0.06	0.4	1.1
84 9 8	1554 42.14	44 23.49	114 7.49	7.25	1.66	18	84	2.4	0.04	0.4	1.1
84 9 8	1623 3.92	44 21.94	114 7.21	5.26	0.82	20	64	3.9	0.04	0.4	1.0
84 9 8	1631 34.20	44 23.51	114 7.61	6.65	0.77	20	54	2.3	0.07	0.4	1.0
84 9 8	1710 30.79	44 22.14	114 7.73	3.91	1.46	20	58	3.2	0.10	0.4	1.4
84 9 8	1735 8.38	44 23.54	114 7.62	6.96	0.97	20	54	2.3	0.06	0.4	0.9
84 9 8	1854 33.21	44 23.24	114 6.86	7.70	1.47	20	56	4.4	0.04	0.4	1.0
84 9 8	19 0 37.10	44 23.59	114 8.05	6.92	1.33	20	50	5.8	0.03	0.4	1.1
84 9 8	1918 19.01	44 23.25	114 7.28	6.75	1.18	21	54	2.7	0.03	0.4	0.9
84 9 8	1930 3.27	44 23.06	114 6.03	7.02	1.04	21	49	3.2	0.05	0.4	0.9

DATE	ORIGIN	LAT N	LONG W	Z	MAG	NO	GAP	DMIN	RMS	ERH	ERZ
84 9 8	20 9 2.48	44 23.23	114 6.75	8.14	1.34	19	56	3.4	0.04	0.4	0.9
84 9 8	2157 48.05	44 23.40	114 7.15	7.57	0.97	20	56	2.9	0.04	0.4	0.9
84 9 8	2241 57.51	44 23.30	114 8.03	6.28	1.06	21	50	1.7	0.07	0.4	1.0
84 9 8	23 9 21.65	44 21.81	114 6.46	6.62	0.66	21	68	3.5	0.06	0.4	1.0
84 9 8	2336 59.82	44 21.88	114 6.39	6.86	0.74	21	68	3.4	0.04	0.4	0.9
84 9 9	0 8 54.64	44 23.13	114 5.46	9.73	1.02	21	45	2.7	0.05	0.4	0.8
84 9 9	021 33.46	44 23.36	114 8.13	6.49	1.13	21	49	1.6	0.05	0.4	0.9
84 9 9	039 45.47	44 22.35	114 6.43	7.92	1.01	21	57	3.4	0.06	0.4	0.9
84 9 9	047 32.14	44 22.13	114 6.84	6.69	1.21	21	62	4.0	0.04	0.4	0.9
84 9 9	1 8 16.63	44 22.38	114 6.55	6.54	0.98	21	56	3.6	0.06	0.4	1.0
84 9 9	250 38.35	44 23.43	114 7.54	7.09	1.36	21	55	2.4	0.04	0.4	0.9
84 9 9	437 18.94	44 23.64	114 7.18	8.23	1.12	21	56	2.9	0.03	0.4	0.9
84 9 9	442 58.59	44 22.76	114 6.50	7.83	1.36	21	46	3.6	0.04	0.4	0.9
84 9 9	5 1 53.38	44 23.17	114 4.83	8.90	1.48	21	56	2.1	0.05	0.4	0.8
84 9 9	620 27.19	44 22.25	114 8.68	3.56	1.30	21	54	2.3	0.05	0.4	1.2
84 9 9	7 7 10.88	44 23.56	114 6.97	8.20	1.82	21	56	3.1	0.02	0.4	0.9
84 9 9	735 9.29	44 22.91	114 6.88	7.23	1.79	21	50	3.4	0.03	0.4	0.9
84 9 9	738 20.78	44 23.13	114 8.30	6.23	2.03	21	48	1.5	0.04	0.4	0.9
84 9 9	835 36.57	44 21.87	114 7.18	5.25	0.95	21	66	4.1	0.04	0.4	1.0
84 9 9	1056 57.23	44 23.45	114 7.50	7.23	1.71	21	55	2.4	0.05	0.4	0.9
84 9 9	1241 36.67	44 24.13	114 7.52	6.51	0.61	20	55	4.6	0.07	0.4	1.1
84 9 9	1244 50.74	44 24.22	114 7.61	6.59	1.14	21	53	2.7	0.03	0.4	0.9
84 9 9	1339 37.90	44 23.39	114 7.89	6.45	0.80	20	52	1.9	0.06	0.4	0.9
84 9 9	1416 52.40	44 22.53	114 6.94	6.53	0.83	20	52	3.6	0.06	0.4	1.0
84 9 9	16 9 22.57	44 22.39	114 5.48	4.04	0.64	20	94	2.2	0.05	0.4	1.1
84 9 9	1717 39.36	44 22.28	114 6.37	8.09	0.76	21	59	3.3	0.06	0.4	1.0
84 9 9	1837 43.21	44 24.09	114 7.81	6.27	0.93	20	64	2.4	0.06	0.4	0.9
84 9 9	1935 35.69	44 22.63	114 8.47	4.60	0.81	20	105	1.9	0.06	0.4	1.0
84 9 9	2112 2.02	44 23.22	114 7.24	7.11	1.21	17	101	5.5	0.08	0.5	1.3
84 910	1 3 26.82	44 22.60	114 3.57	7.27	0.81	20	76	0.7	0.06	0.4	0.9
84 910	224 3.43	44 22.57	114 6.49	7.44	1.20	19	66	3.5	0.06	0.4	1.0
84 910	226 14.82	44 23.36	114 4.06	8.48	0.94	20	71	1.8	0.05	0.4	0.8
84 910	227 4.56	44 22.50	114 6.63	6.93	0.76	20	67	3.7	0.05	0.4	0.9
84 910	333 38.81	44 22.35	114 6.55	7.49	0.94	19	87	3.6	0.04	0.4	1.0
84 910	5 2 14.29	44 24.23	114 4.52	8.24	1.08	20	64	1.6	0.04	0.4	0.9
84 910	7 9 36.01	44 23.45	114 7.62	7.73	0.93	19	62	2.3	0.04	0.4	1.0
84 910	736 5.89	44 23.39	114 7.16	8.16	0.73	19	63	2.9	0.05	0.4	1.0
84 910	914 7.83	44 21.53	114 7.17	5.97	0.68	19	72	4.5	0.09	0.4	1.1
84 910	920 14.24	44 23.45	114 7.04	8.06	1.04	18	61	3.0	0.03	0.4	1.0
84 910	1055 0.33	44 23.45	114 6.89	7.91	0.51	18	61	3.2	0.04	0.5	1.0
84 910	1149 14.47	44 23.44	114 7.53	6.58	0.52	19	63	2.4	0.06	0.4	1.0
84 910	1238 40.86	44 22.71	114 6.16	7.48	0.65	18	64	3.2	0.04	0.5	1.0
84 910	17 3 36.50	44 23.47	114 8.56	5.50	0.62	16	62	1.0	0.05	0.4	1.1
84 910	1945 23.67	44 22.41	114 6.51	7.44	0.77	19	67	3.5	0.05	0.4	1.0
84 910	2356 9.32	44 23.55	114 7.83	7.21	0.72	21	58	2.0	0.04	0.4	0.9
84 911	2 6 16.46	44 22.20	114 6.80	6.43	0.85	21	69	3.9	0.05	0.4	0.9
84 911	411 1.24	44 22.43	114 6.53	7.37	1.27	21	67	3.6	0.04	0.4	0.9
84 911	945 52.94	44 23.58	114 7.55	8.05	0.65	21	57	2.4	0.06	0.4	0.9
84 911	954 10.51	44 23.39	114 7.40	7.07	1.45	21	64	2.6	0.05	0.4	0.9
84 911	957 56.81	44 23.49	114 7.30	7.81	0.78	21	60	2.7	0.07	0.4	0.9
84 911	1645 46.99	44 22.94	114 6.80	7.93	0.80	19	66	3.5	0.06	0.4	0.9
84 911	1759 48.29	44 22.36	114 8.66	5.42	1.41	19	87	2.2	0.04	0.4	1.0
84 911	1811 20.38	44 25.42	114 3.97	2.67	0.61	19	49	2.5	0.10	0.4	1.6
84 911	2028 41.77	44 23.34	114 7.03	6.14	0.71	15	69	3.1	0.06	0.4	1.1
84 911	2136 5.35	44 22.64	114 4.64	7.23	0.96	15	61	3.3	0.04	0.4	1.2
84 912	135 3.05	44 23.27	114 7.09	6.29	0.62	14	69	5.3	0.05	0.4	1.3
84 912	5 3 5.10	44 26.20	114 4.87	6.32	1.08	13	73	2.0	0.03	0.4	1.1
84 912	622 49.22	44 23.29	114 8.95	4.63	0.93	14	78	6.5	0.08	0.5	1.8
84 912	818 8.67	44 23.87	114 5.09	9.91	1.13	14	61	2.4	0.04	0.5	1.1

DATE	ORIGIN	LAT N	LONG W	Z	MAG	NO	GAP	DMIN	RMS	ERH	ERZ
84 912	911 7.42	44 23.13	114 7.59	6.68	1.02	13	116	6.0	0.08	0.6	1.4
84 912	1814 10.67	44 23.09	114 6.32	7.72	1.01	11	123	4.4	0.02	0.6	1.3
84 912	1833 45.40	44 23.06	114 6.26	7.62	1.20	11	123	4.4	0.03	0.6	1.3
84 912	2148 17.90	44 25.25	114 5.74	8.83	1.09	10	96	2.4	0.04	0.6	1.3
84 913	1112 49.13	44 23.85	114 6.48	8.97	3.9 M_L	11	65	4.2	0.03	0.5	1.2
84 913	1237 54.92	44 23.19	114 6.57	7.37	1.82	10	71	4.6	0.01	0.5	1.6
84 913	1248 48.14	44 23.90	114 6.36	8.78	1.01	10	71	4.0	0.03	0.6	1.4
84 913	22 7 4.65	44 23.43	114 7.82	6.54	1.33	11	76	5.9	0.02	0.5	1.5
84 914	248 27.56	44 25.22	114 5.51	8.96	1.35	11	66	2.6	0.04	0.5	1.2
84 914	318 36.07	44 23.44	114 8.10	8.23	1.61	10	145	6.1	0.04	0.7	1.6
84 914	946 5.56	44 22.05	114 6.37	7.79	1.41	11	79	5.6	0.04	0.5	1.7
84 914	954 3.13	44 22.10	114 6.23	7.80	1.64	11	78	5.4	0.04	0.5	1.7

APPENDIX D

Focal Mechanisms

Focal mechanisms and variations in the T- and P-axes (small circles) as computed by the FPFIT program (Reasenberg and Oppenheimer, 1985). Focal mechanisms categorized by fault location and representative focal mechanisms were computed using the Devil Canyon velocity model (see text, Figure 6). Focal mechanisms categorized by fault location and depths of 8.0 and 9.0 km were computed for variations in the depth of the intermediate layer (5.9 km/s) upper boundary of the Devil Canyon velocity model.

Each focal mechanism is identified by the summary output explained in Appendix C. Open circles represent dilatations, pluses represent compressions, T indicates the position of the tensional axis, and P indicates the position of the compressional axis. A few of the mechanisms are of lesser quality than the majority and if omitted would not change the results very much shown in Table 3 in the text.

CHALLIS SEGMENT

840905 436 39.57 44-22.46 114- 4.00 8.83 1.40 21 70 .0 .04 .4 .8

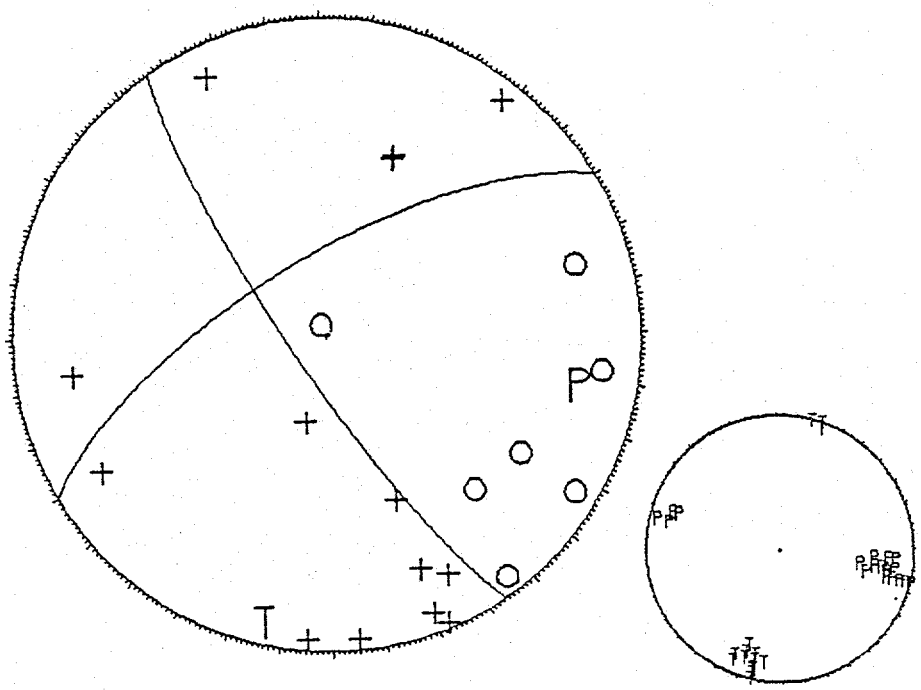

840904 1511 41.54 44-24.70 114- 5.36 10.54 2.00 22 46 3.0 .03 .4 .8

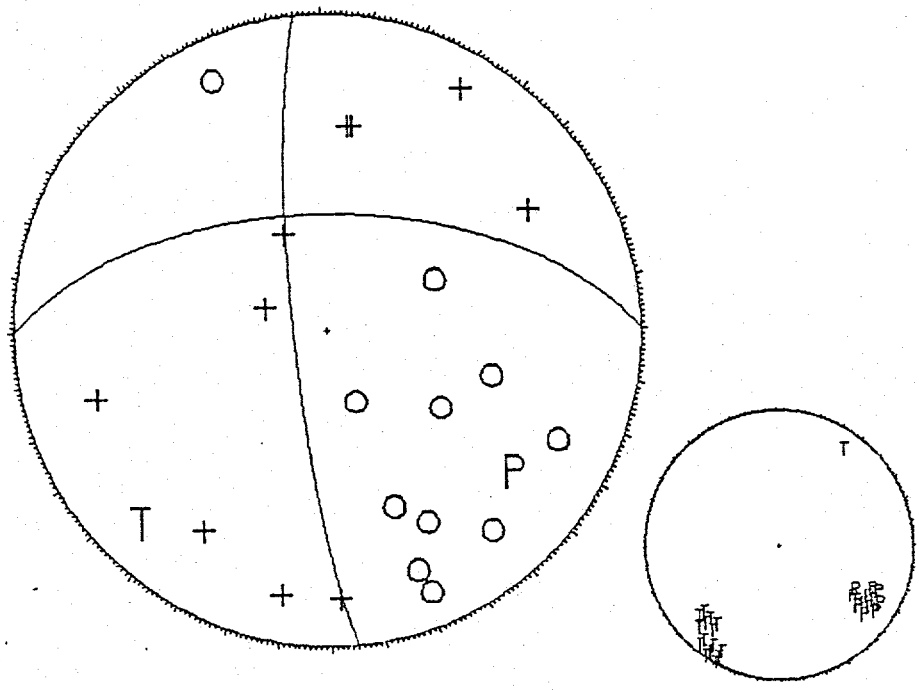

CHALLIS SEGMENT

840909 501 53.38 44-23.17 114- 4.83 8.90 1.50 21 56 2.0 .05 .4 .8

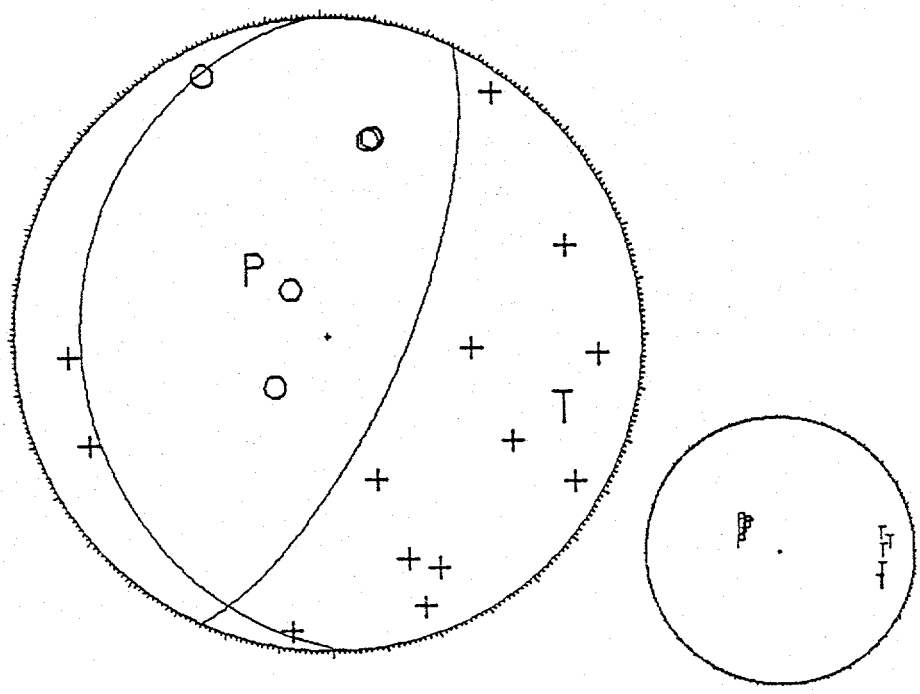

840910 502 14.29 44-24.23 114- 4.52 8.24 1.10 20 64 2.0 .04 .4 .9

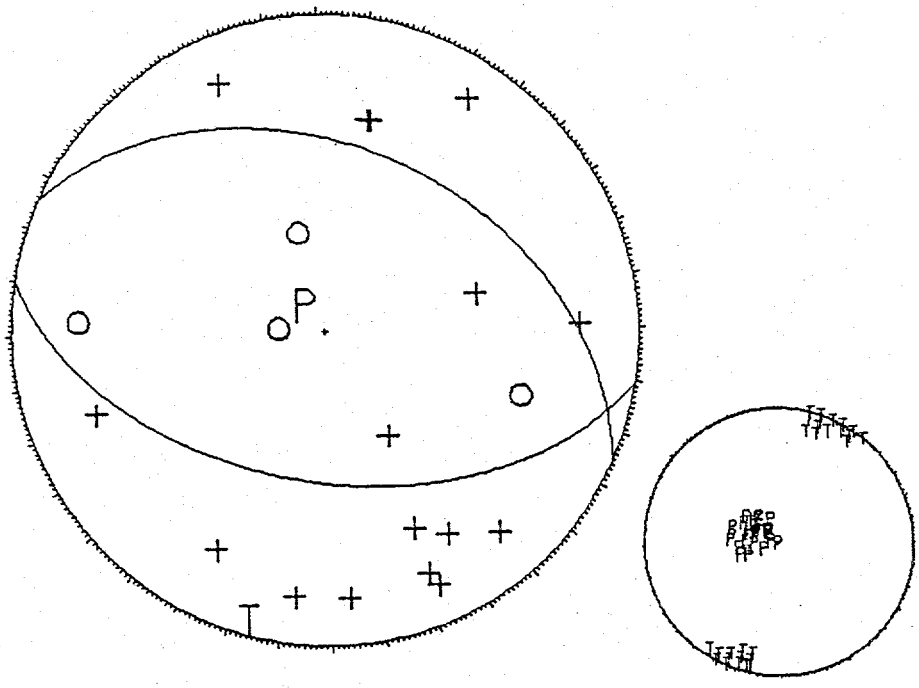

CHALLIS SEGMENT

Representative focal mechanism for the following 8 focal mechanisms:

840904 550 41.04 44-26.13 114- 5.06 7.59 2.40 22 65 2.0 .04 .4 .9

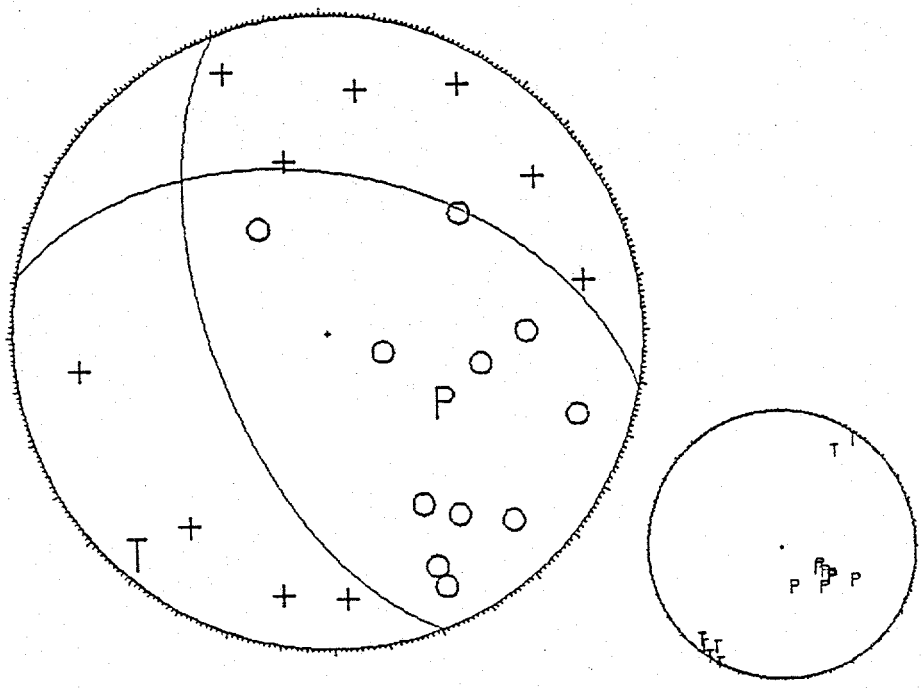

CHALLIS SEGMENT

840901 455 23.80 44-25.92 114- 5.83 8.70 1.30 19 43 1.0 .04 .4 .7

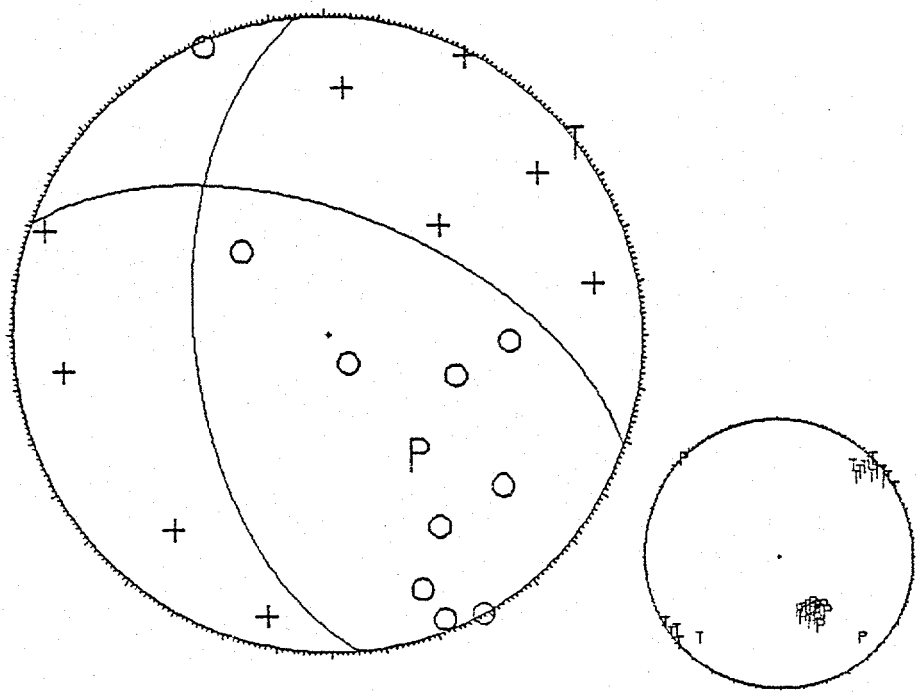

840904 557 21.52 44-26.34 114- 5.09 7.58 2.00 22 66 2.0 .05 .4 .9

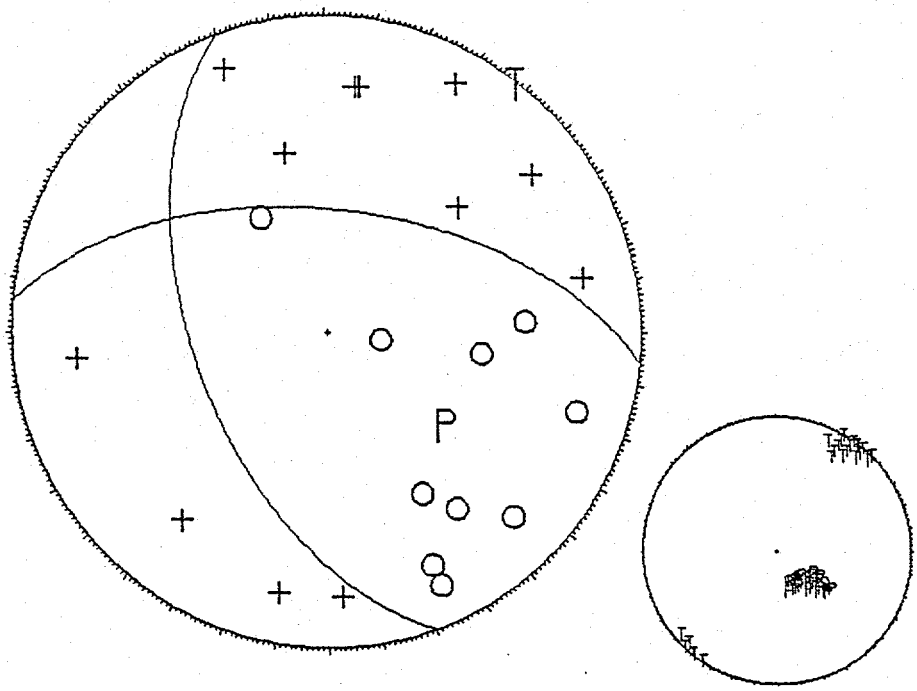

CHALLIS SEGMENT

840904 845 13.67 44-26.27 114- 4.93 6.61 1.10 21 68 2.0 .04 .4 .9

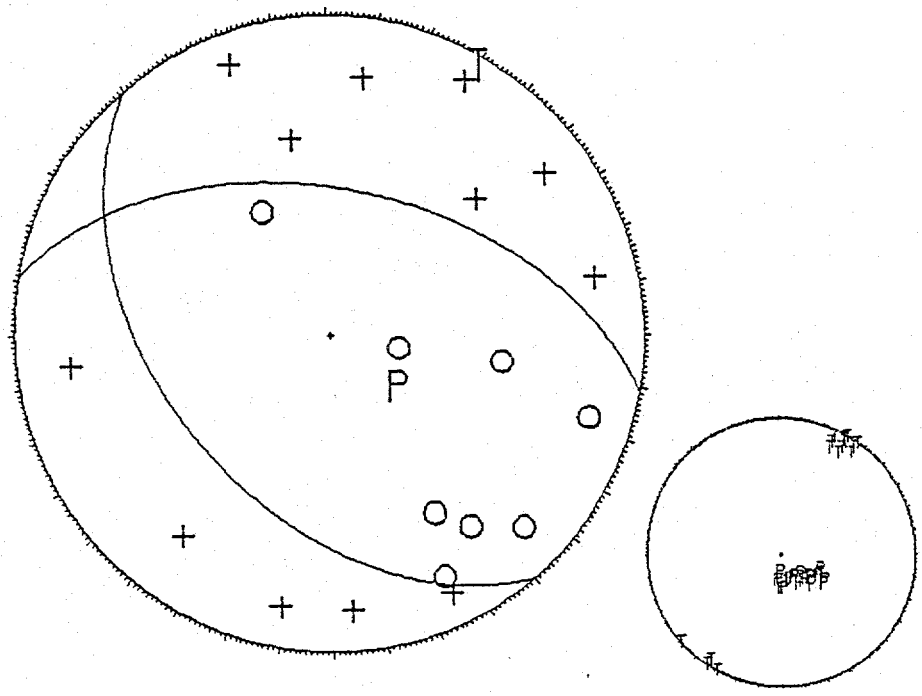

840904 1218 38.17 44-26.09 114- 5.12 7.31 1.10 21 64 2.0 .05 .4 .9

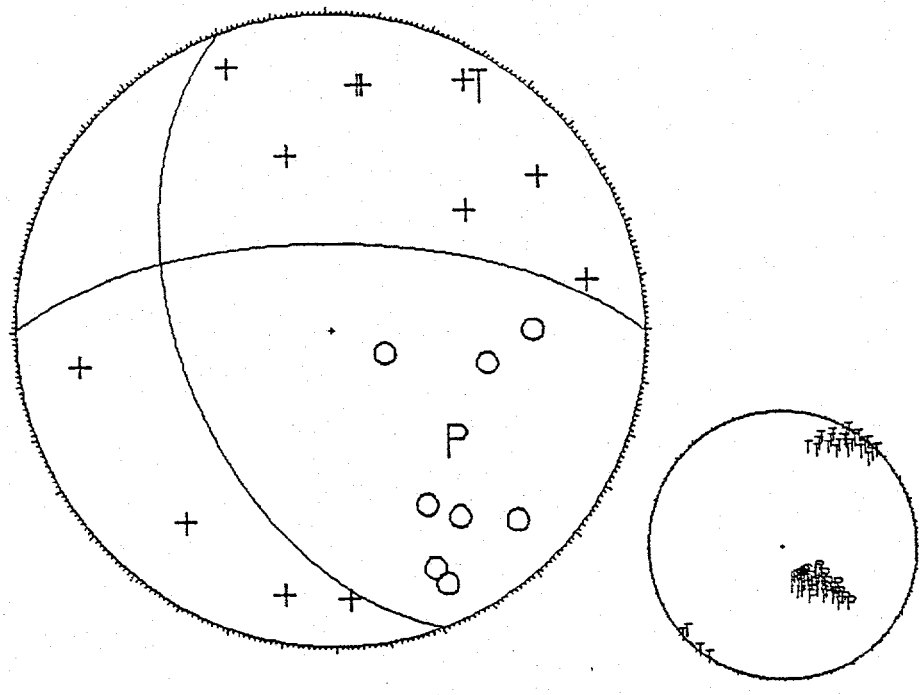

CHALLIS SEGMENT

840904 1410 3.50 44-26.18 114- 4.89 7.19 1.90 22 68 2.0 .04 .4 .9

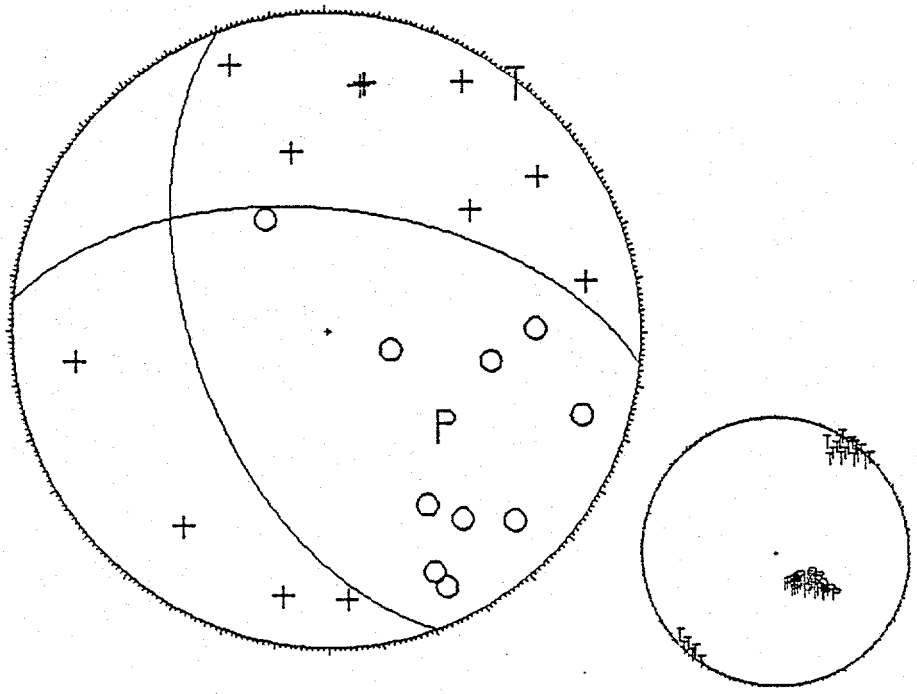

840905 22 46.87 44-25.82 114- 5.85 8.59 1.10 21 68 1.0 .05 .4 .7

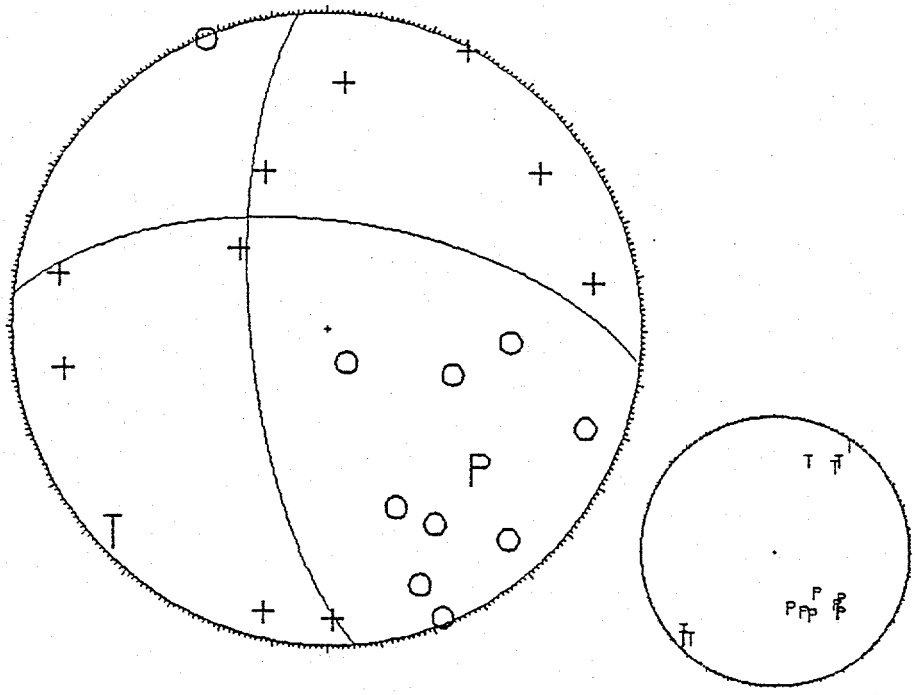

CHALLIS SEGMENT

840905 53 33.18 44-26.16 114- 5.03 7.36 1.40 22 46 2.0 .03 .3 .9

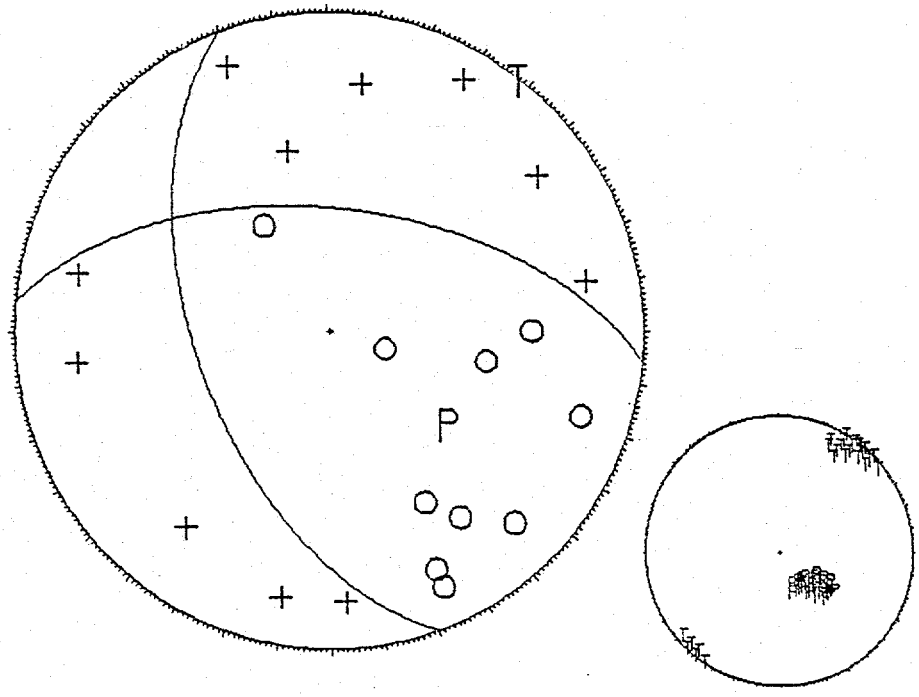

840905 1643 48.61 44-26.10 114- 4.92 7.55 1.80 21 46 2.0 .05 .4 .9

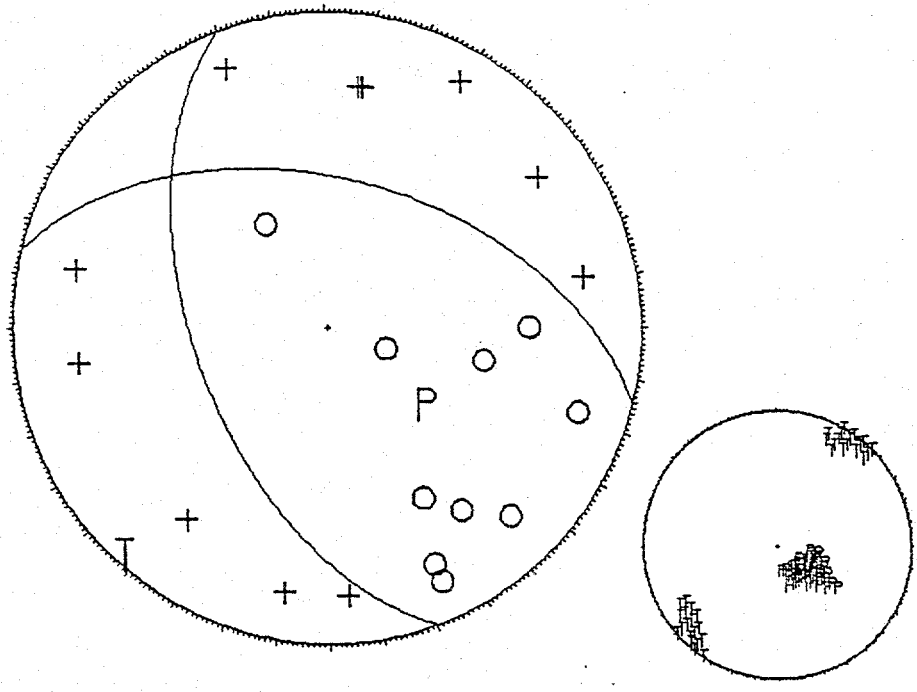

CHALLIS SEGMENT

Reverse Mechanisms:

840901 1411 18.22 44-24.64 114- 5.21 10.46 2.50 19 42 3.0 .04 .4 .8

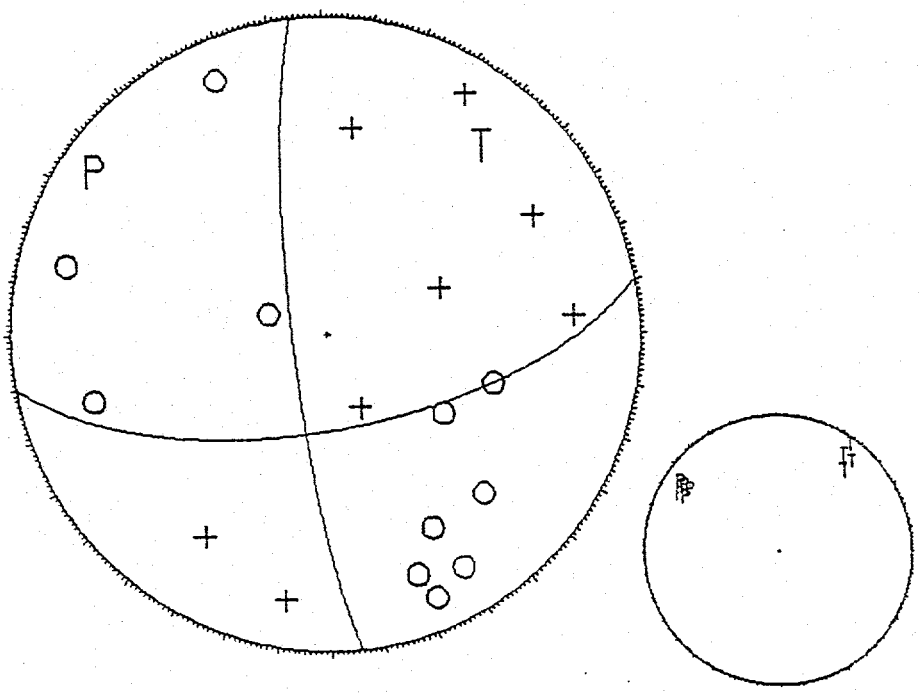

840829 1509 18.18 44-23.80 114- 4.44 9.06 1.70 17 58 2.0 .05 .4 .8

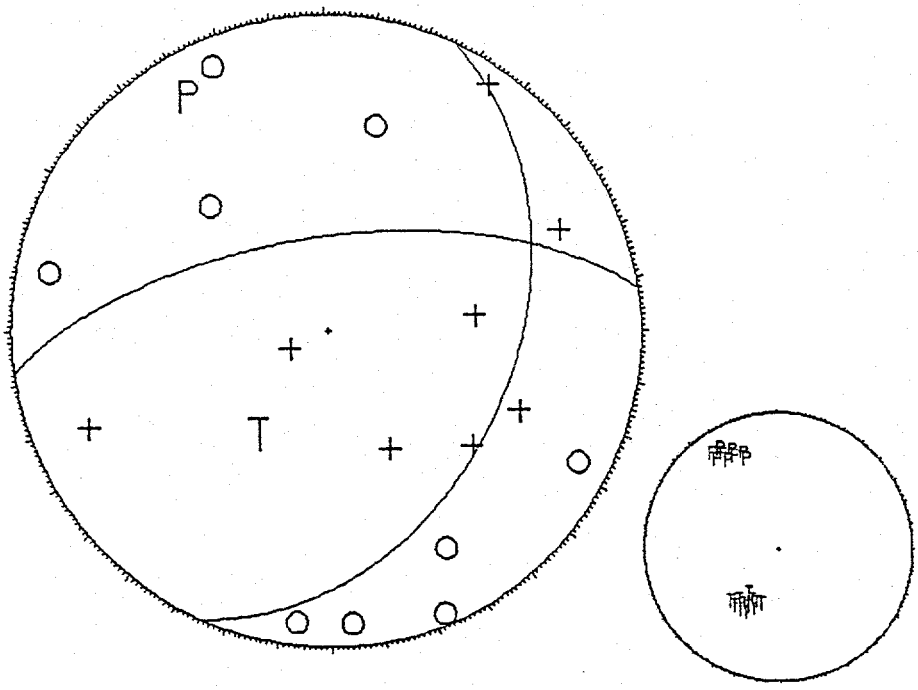

LONE PINE FAULT

840830 1514 23.64 44-24.59 114- 6.53 9.11 1.40 20 61 3.0 .05 .4 .8

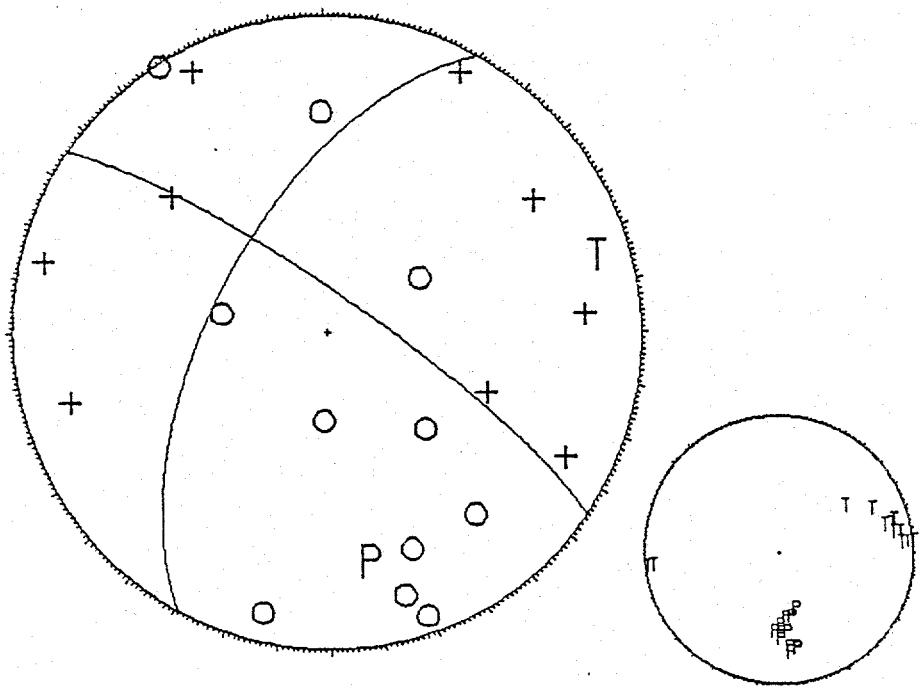

840830 1842 27.34 44-23.93 114- 6.68 9.22 2.60 20 57 4.0 .05 .4 .8

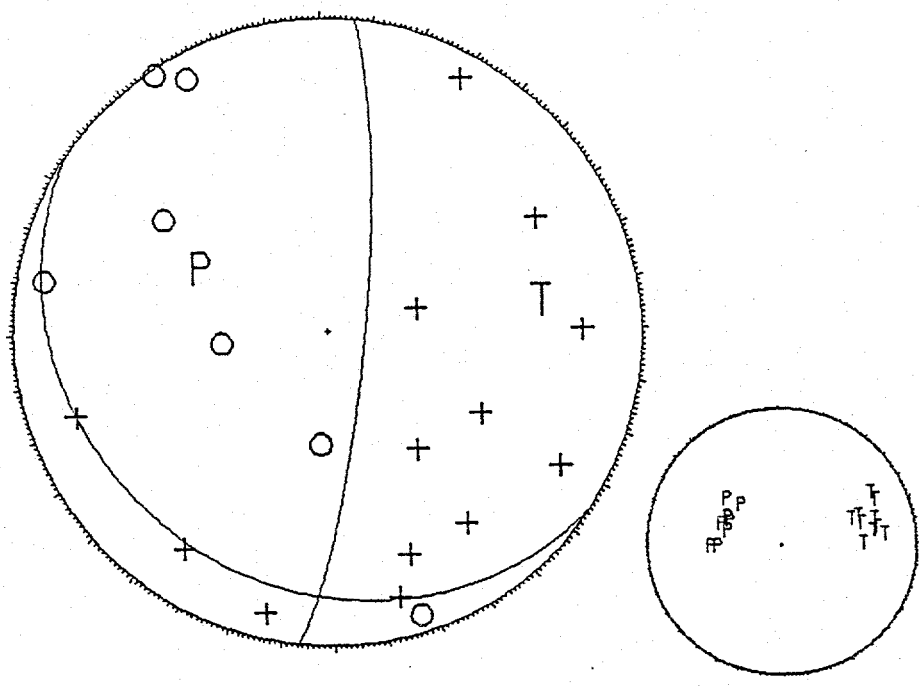

LONE PINE FAULT

840901 634 44.85 44-23.57 114- 6.70 9.43 1.70 19 46 3.0 .04 .4 .8

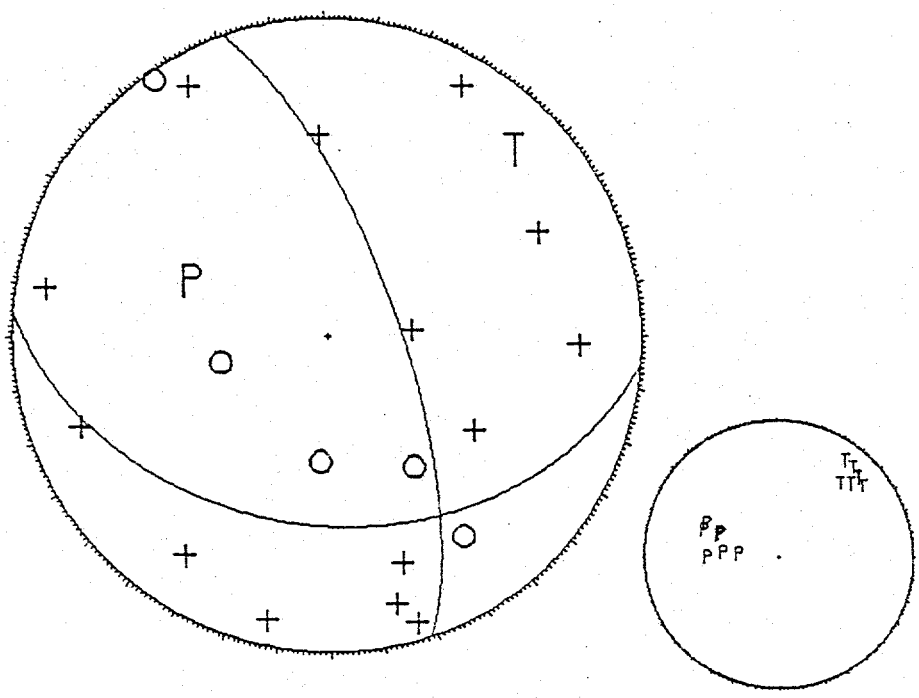

840905 1738 58.60 44-23.33 114- 6.93 8.20 2.70 20 62 5.0 .05 .4 1.1

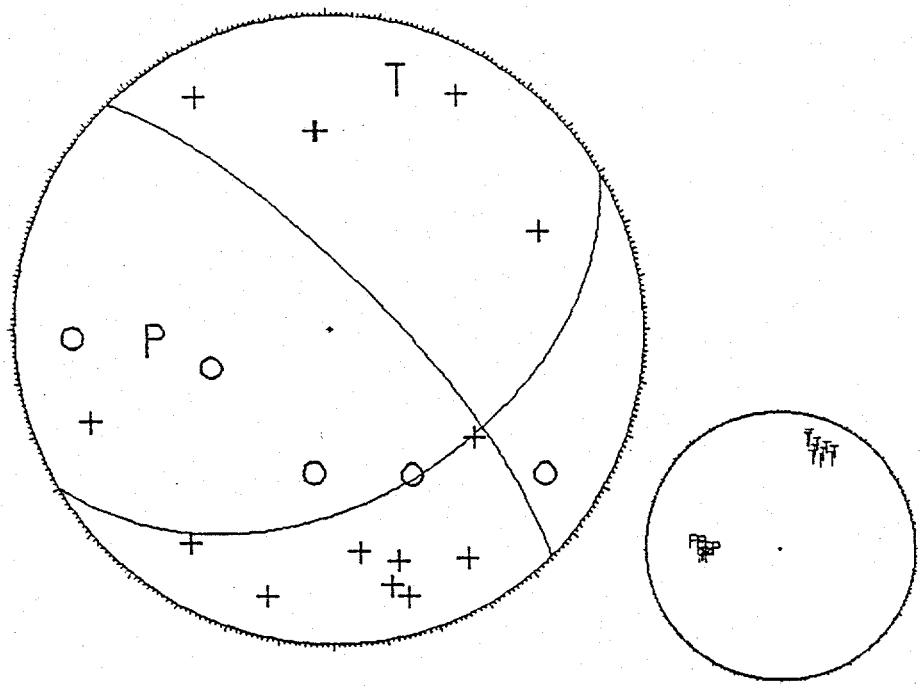

LONE PINE FAULT

840909 8 54.64 44-23.13 114- 5.46 9.73 1.00 21 45 3.0 .05 .4 .8

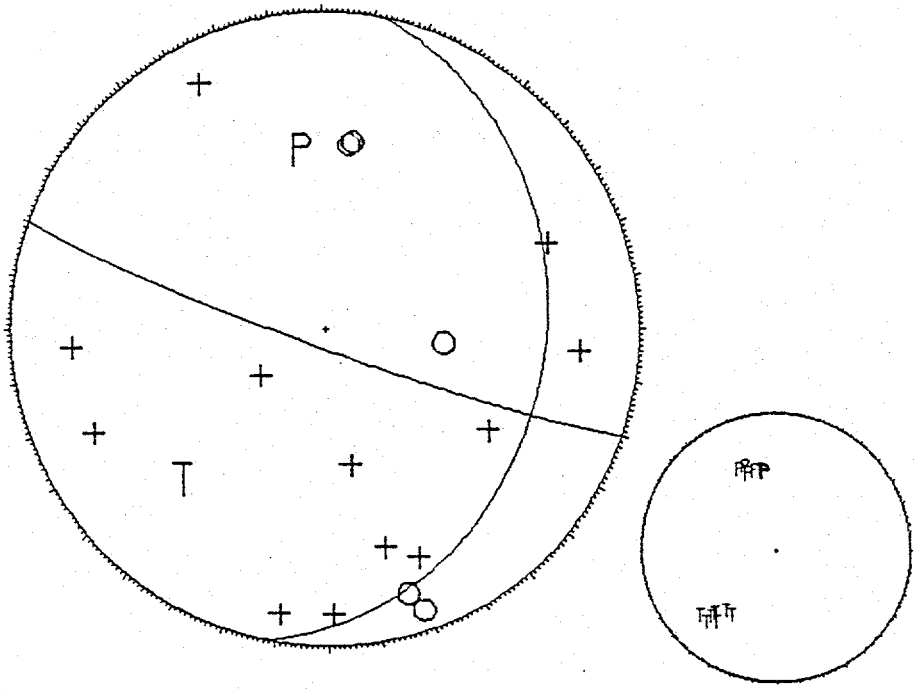

840905 2010 2.94 44-23.41 114- 6.95 7.77 1.60 17 62 5.0 .04 .4 1.2

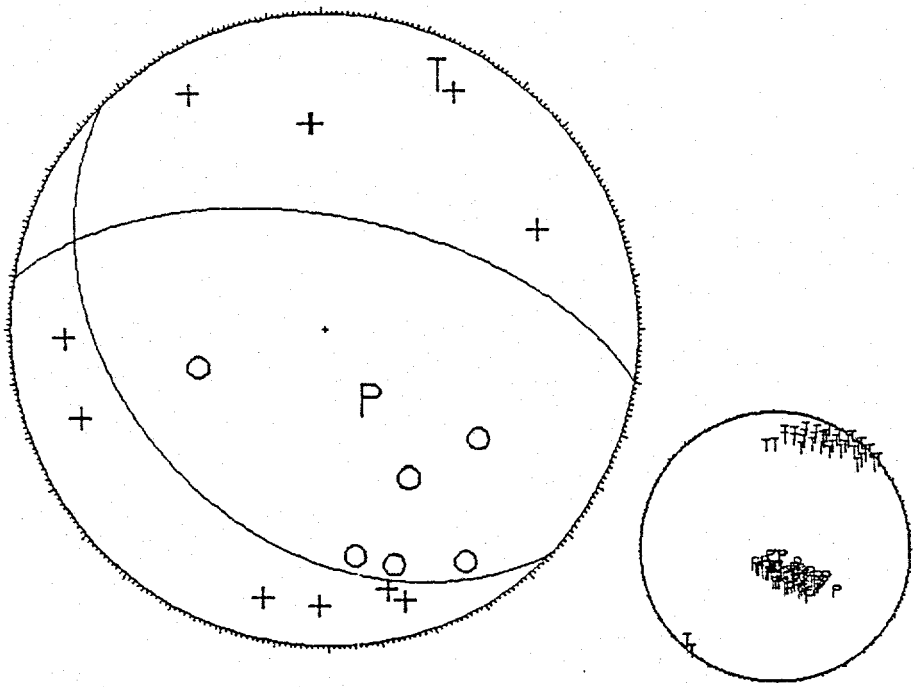

LONE PINE FAULT

September 8, 1984 06:16 M_L 5.0

840908 616 39.92 44-23.17 114- 6.80 7.12 .01 16 90 5.0 .07 .4 1.4

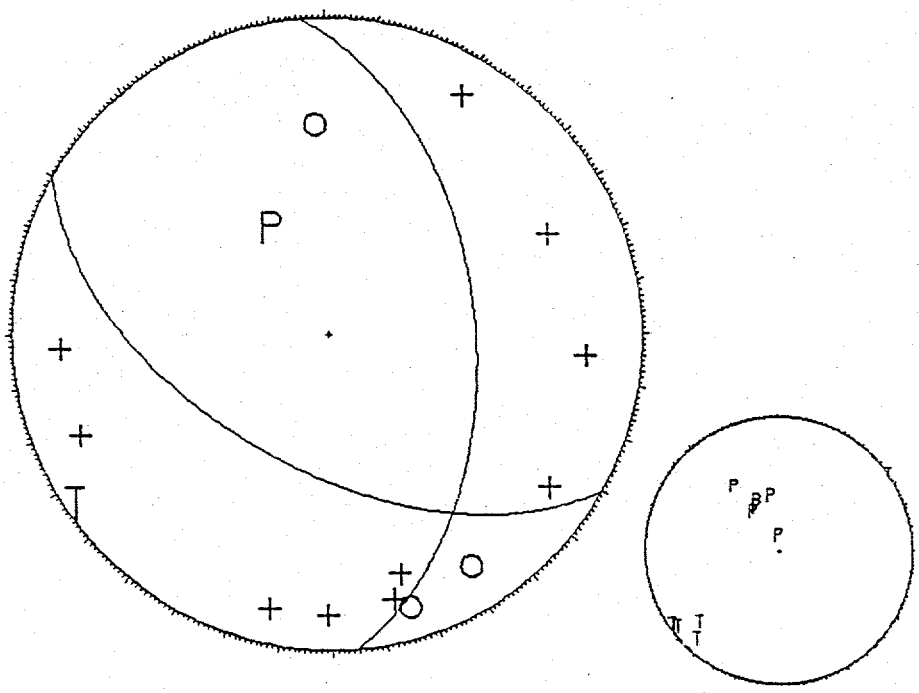

Representative focal mechanism for the following 14 focal mechanisms:

840909 707 10.88 44-23.56 114- 6.97 8.20 1.80 21 56 3.0 .02 .4 .9

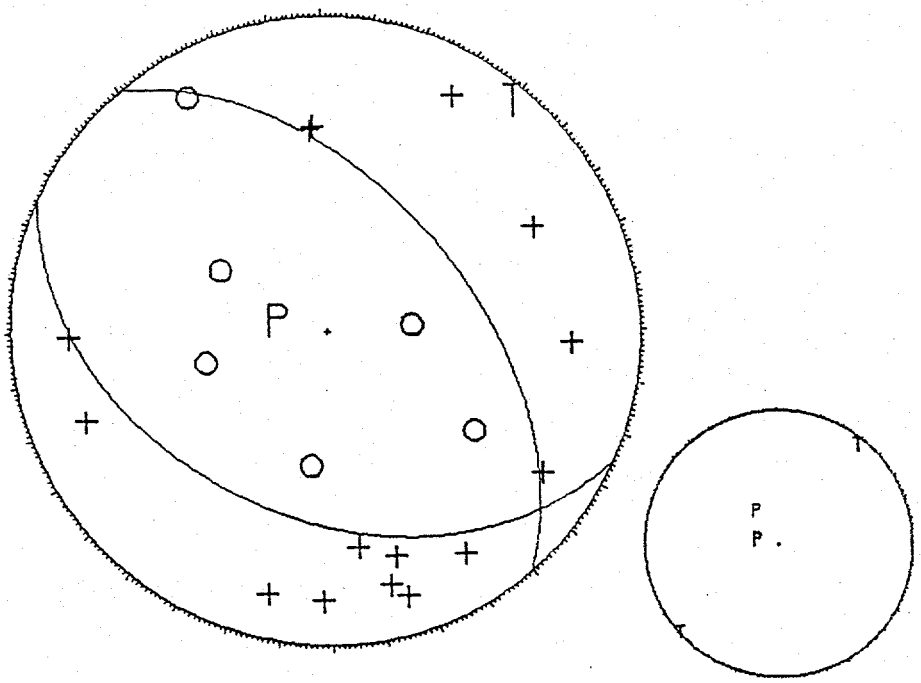

LONE PINE FAULT

840908 922 25.67 44-23.21 114- 7.06 7.94 2.40 19 64 3.0 .05 .4 1.0

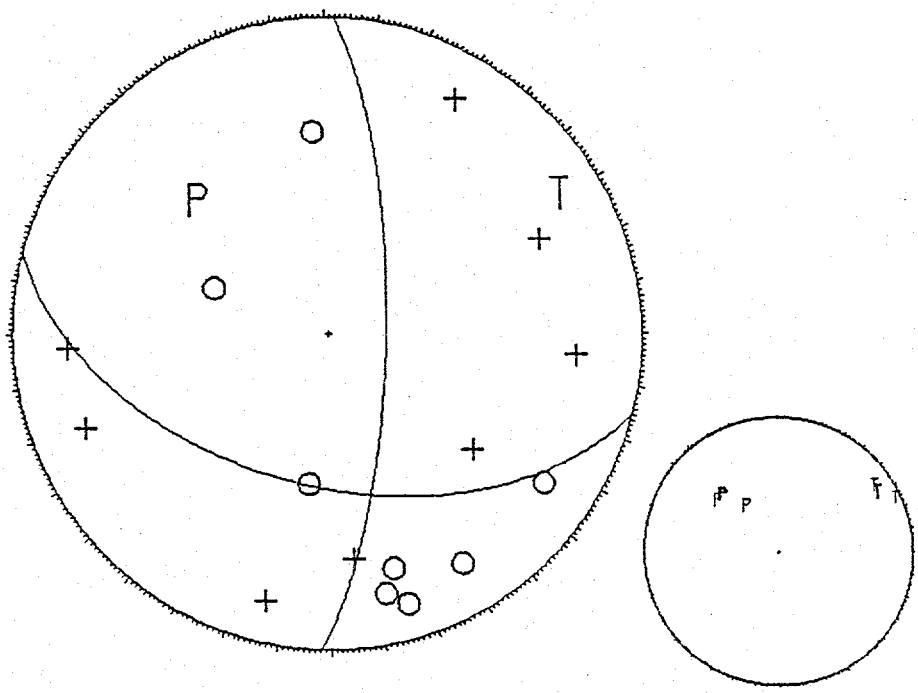

840908 1048 38.30 44-23.19 114- 6.50 8.42 1.30 18 63 4.0 .05 .4 .9

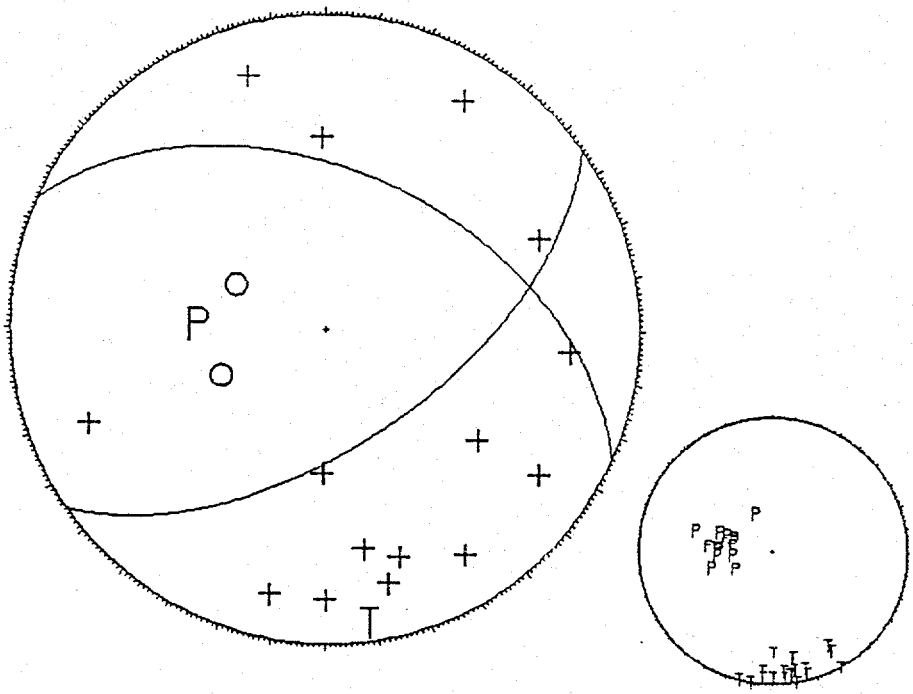

LONE PINE FAULT

840908 1404 33.39 44-23.30 114- 6.78 7.56 1.90 19 61 4.0 .05 .4 1.1

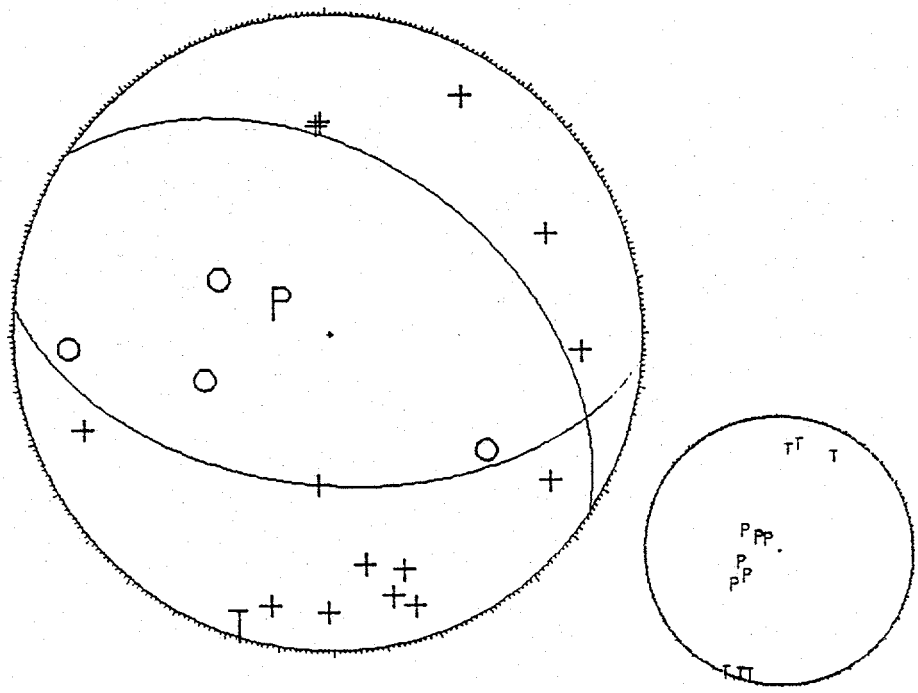

840908 1452 38.86 44-23.17 114- 7.75 6.77 1.50 19 62 2.0 .02 .4 1.0

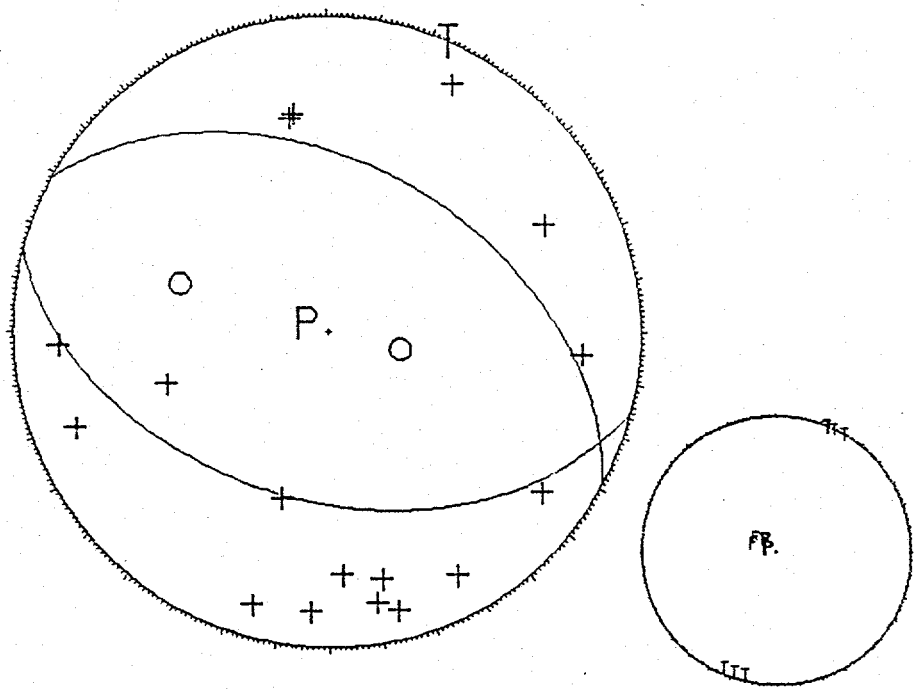

LONE PINE FAULT

840908 1918 19.01 44-23.25 114- 7.28 6.75 1.20 21 54 3.0 .03 .4 .9

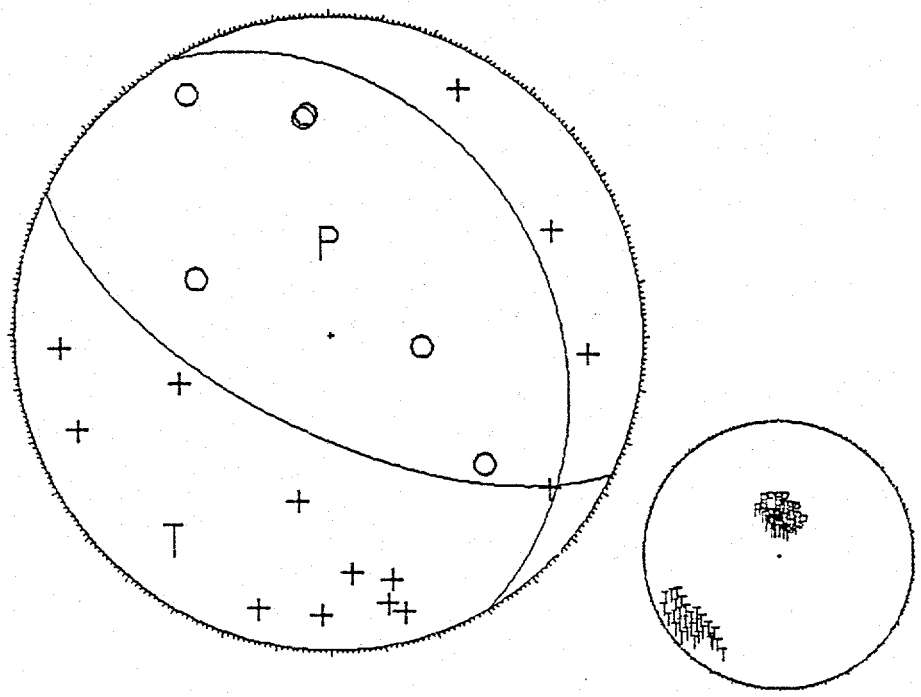

840908 2009 2.48 44-23.23 114- 6.75 8.14 1.30 19 56 3.0 .04 .4 .9

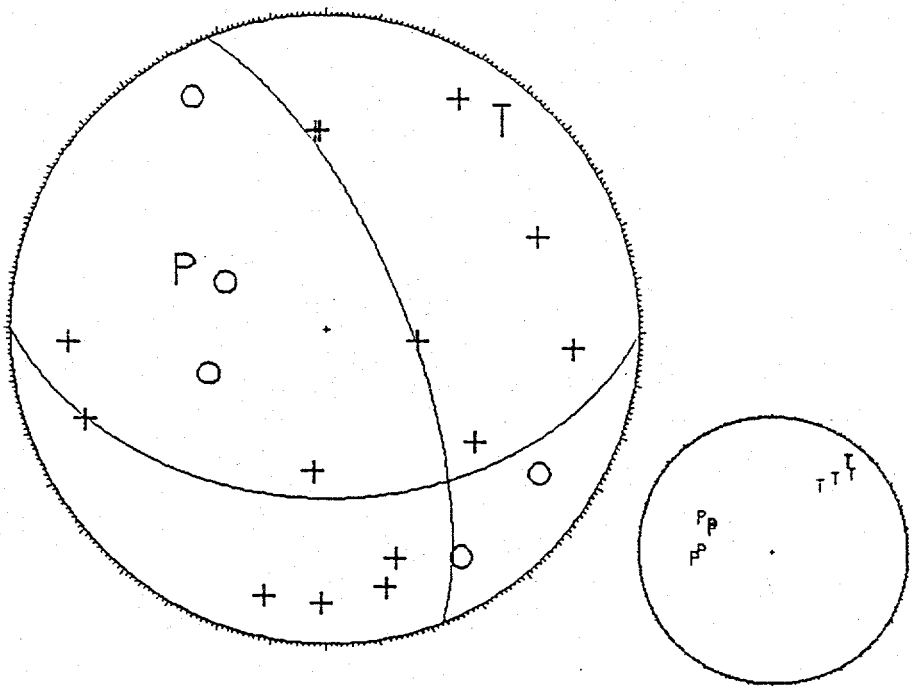

LONE PINE FAULT

840909 47 32.14 44-22.13 114- 6.84 6.69 1.20 21 62 4.0 .04 .4 .9

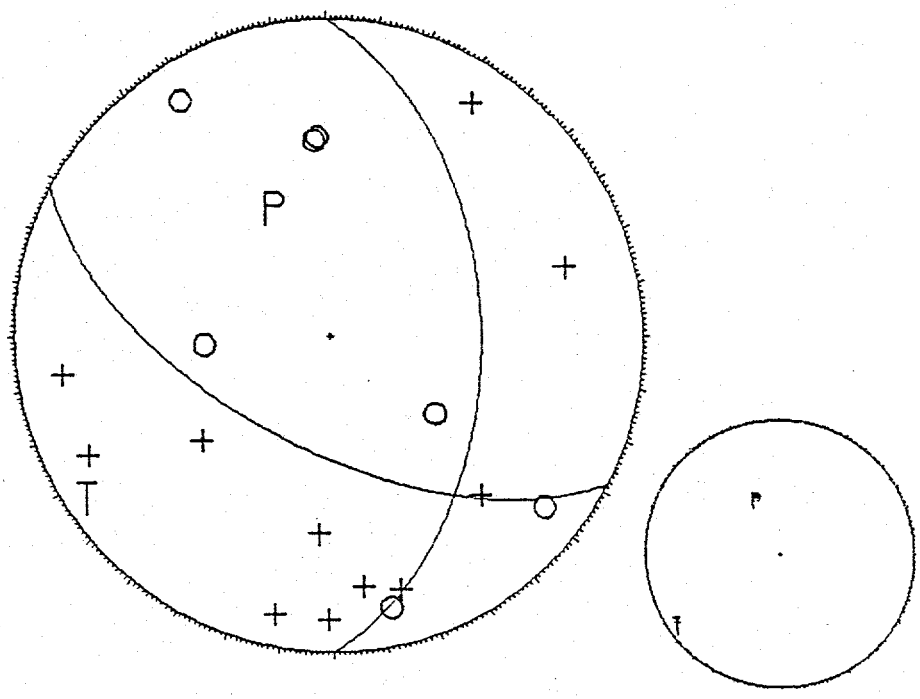

840909 250 38.35 44-23.43 114- 7.54 7.09 1.40 21 55 2.0 .04 .4 .9

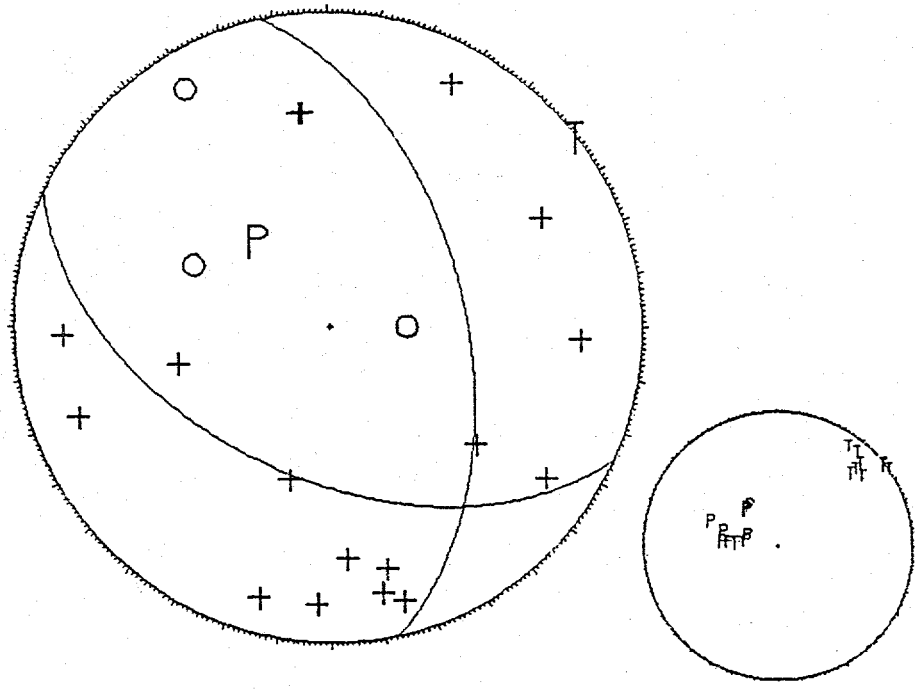

LONE PINE FAULT

840909 437 18.94 44-23.64 114- 7.18 8.23 1.10 21 56 3.0 .03 .4 .9

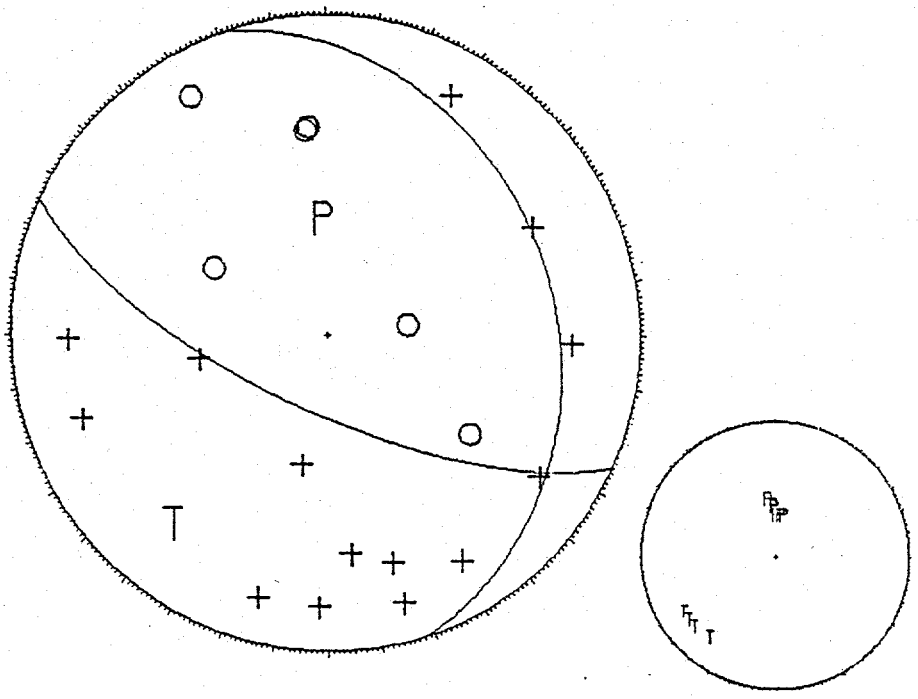

840909 442 58.59 44-22.76 114- 6.50 7.83 1.40 21 46 4.0 .04 .4 .9

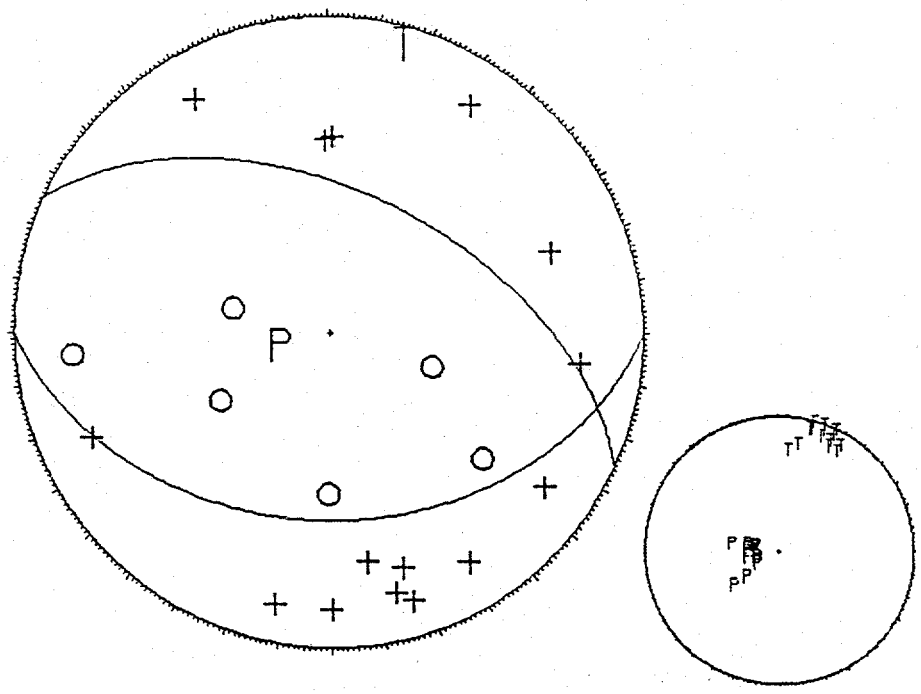

LONE PINE FAULT

840909 735 9.29 44-22.91 114- 6.88 7.23 1.80 21 50 3.0 .03 .4 .9

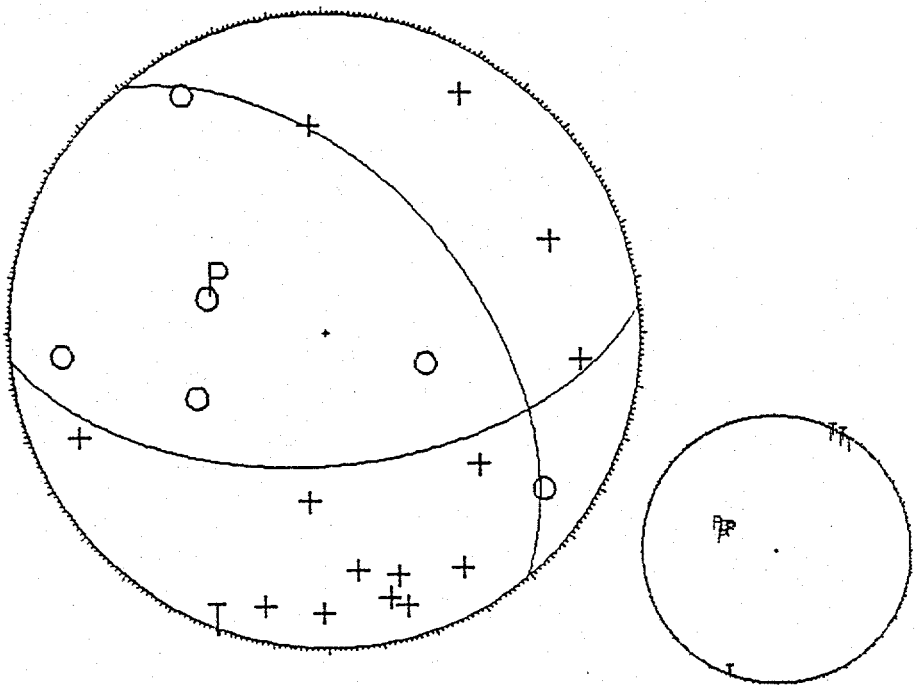

840909 1056 57.23 44-23.45 114- 7.50 7.23 1.70 21 55 2.0 .05 .4 .9

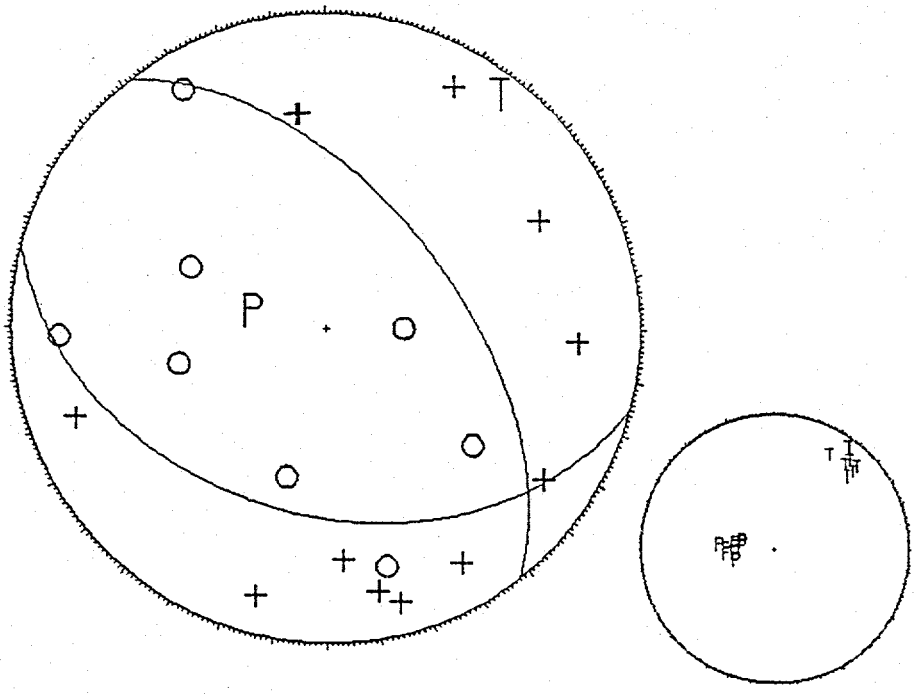

LONE PINE FAULT

840911 411 1.24 44-22.43 114- 6.53 7.37 1.30 21 67 4.0 .04 .4 .9

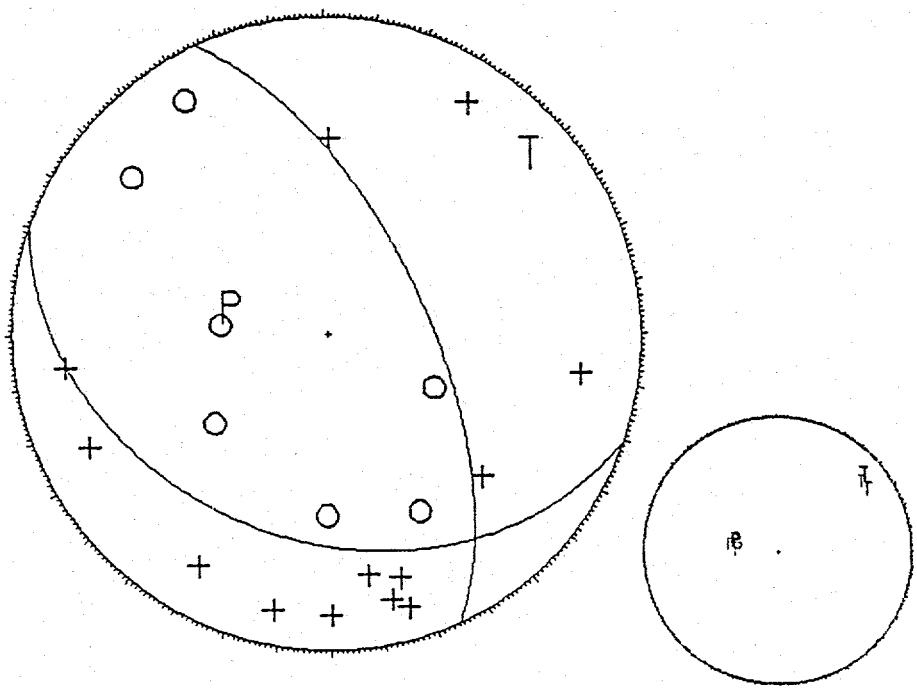

840911 954 10.51 44-23.39 114- 7.40 7.07 1.40 21 64 3.0 .05 .4 .9

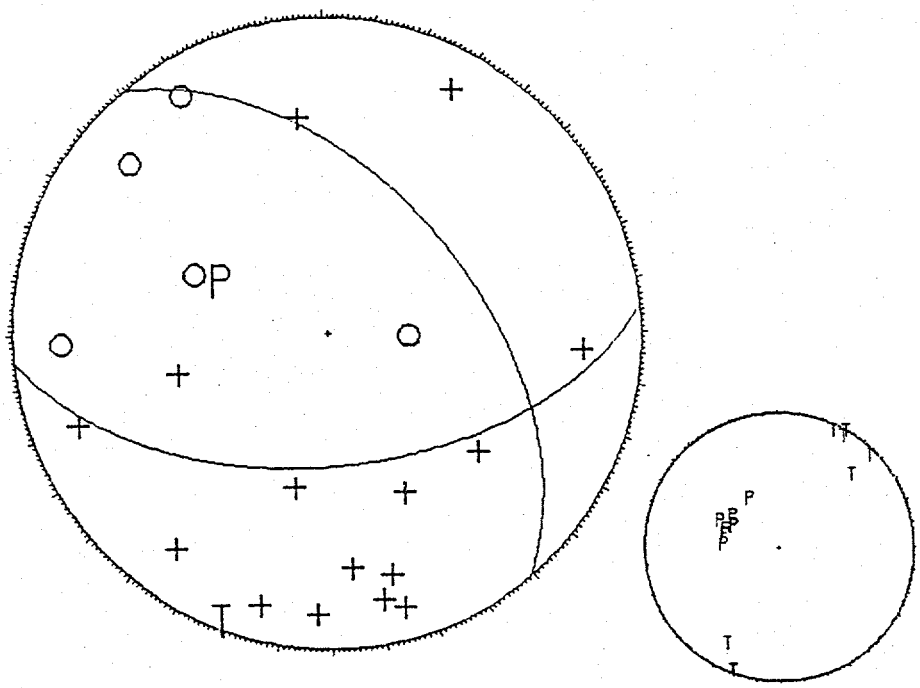

LONE PINE FAULT

Representative focal mechanism for the following 5 focal mechanisms:

840909 1244 50.74 44-24.22 114- 7.61 6.59 1.10 21 53 3.0 .03 .3 .9

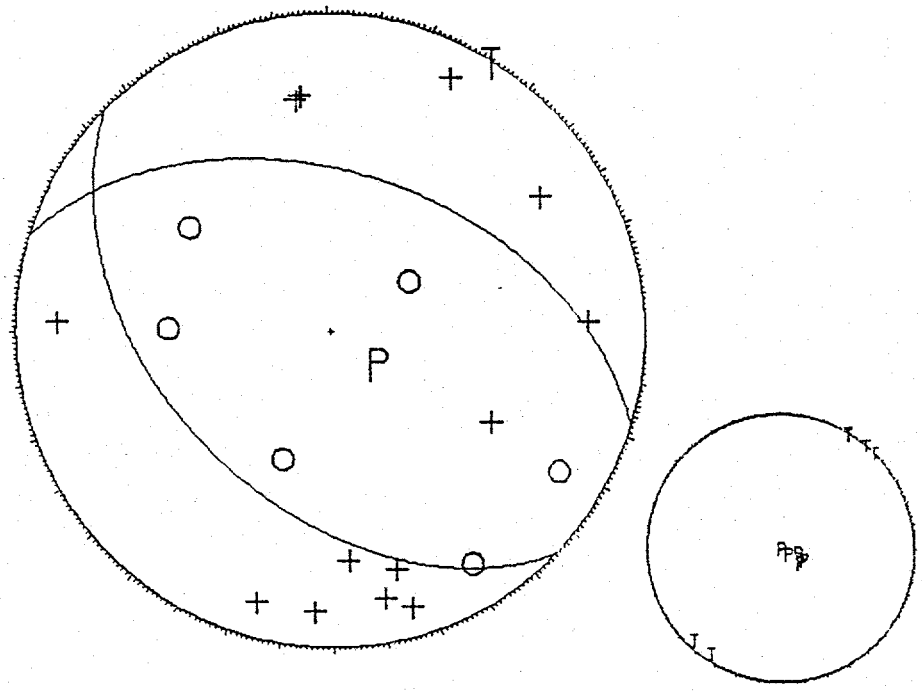

840908 1900 37.10 44-23.59 114- 8.05 6.92 1.30 20 50 6.0 .03 .4 1.1

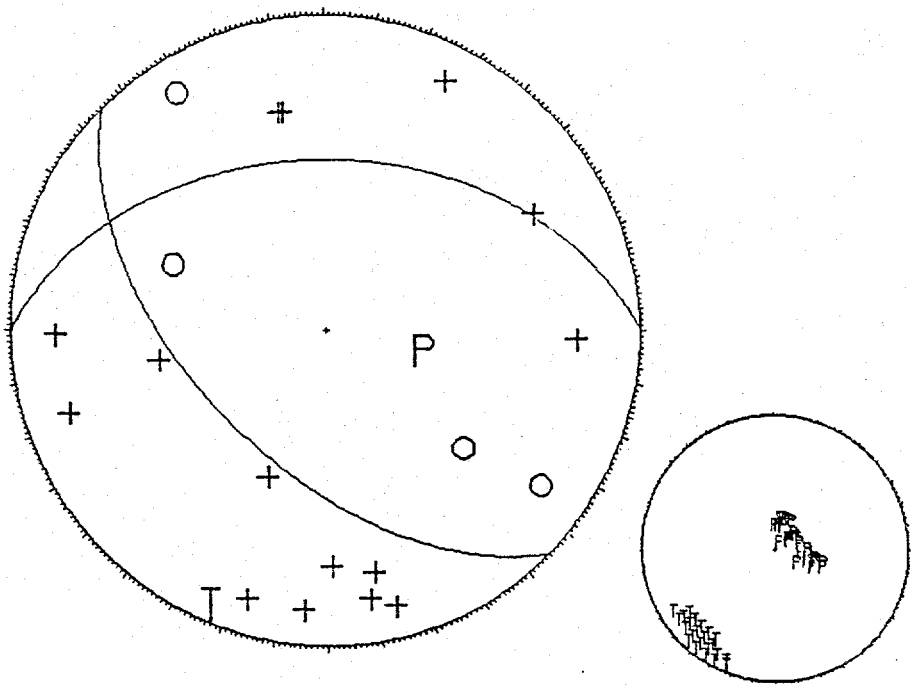

LONE PINE FAULT

840908 1930 3.27 44-23.06 114- 6.03 7.02 1.00 21 49 3.0 .05 .4 .9

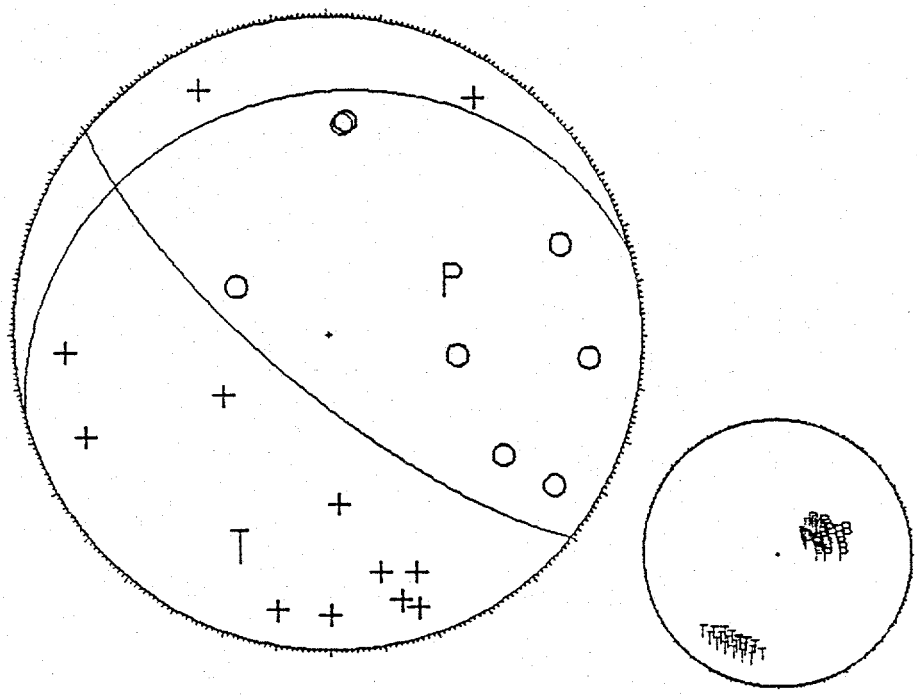

840909 21 33.46 44-23.36 114- 8.13 6.49 1.10 21 49 2.0 .05 .4 .9

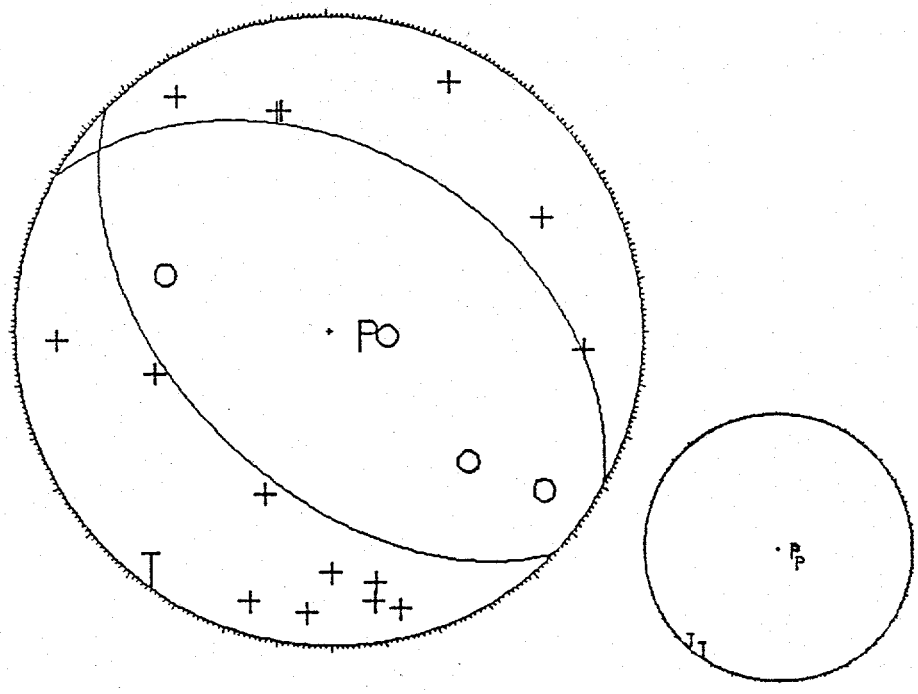

LONE PINE FAULT

840909 738 20.78 44-23.13 114- 8.30 6.23 2.00 21 48 1.0 .04 .4 .9

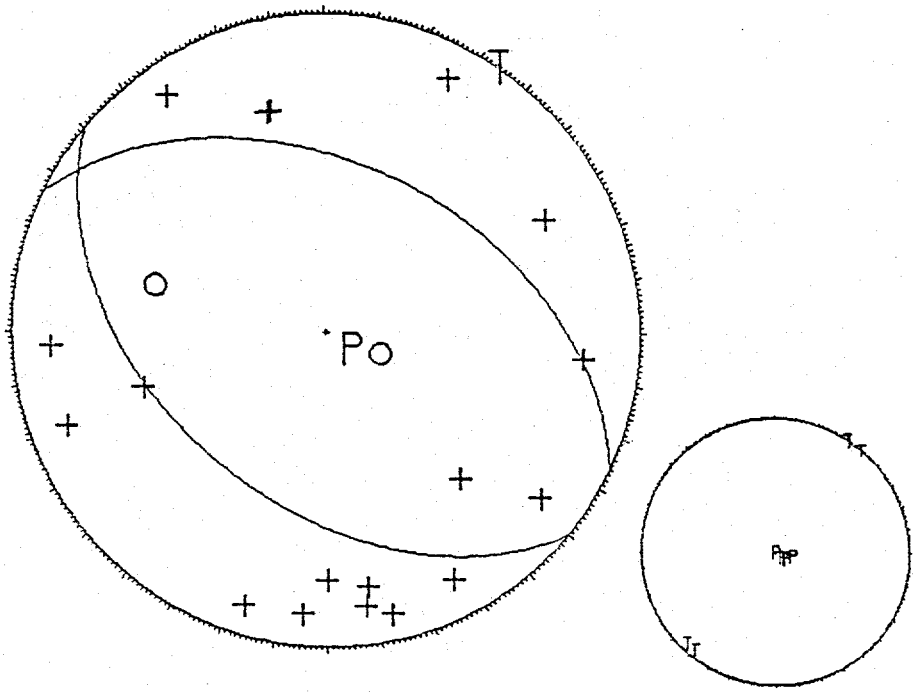

840910 920 14.24 44-23.45 114- 7.04 8.06 1.00 18 61 3.0 .03 .4 1.0

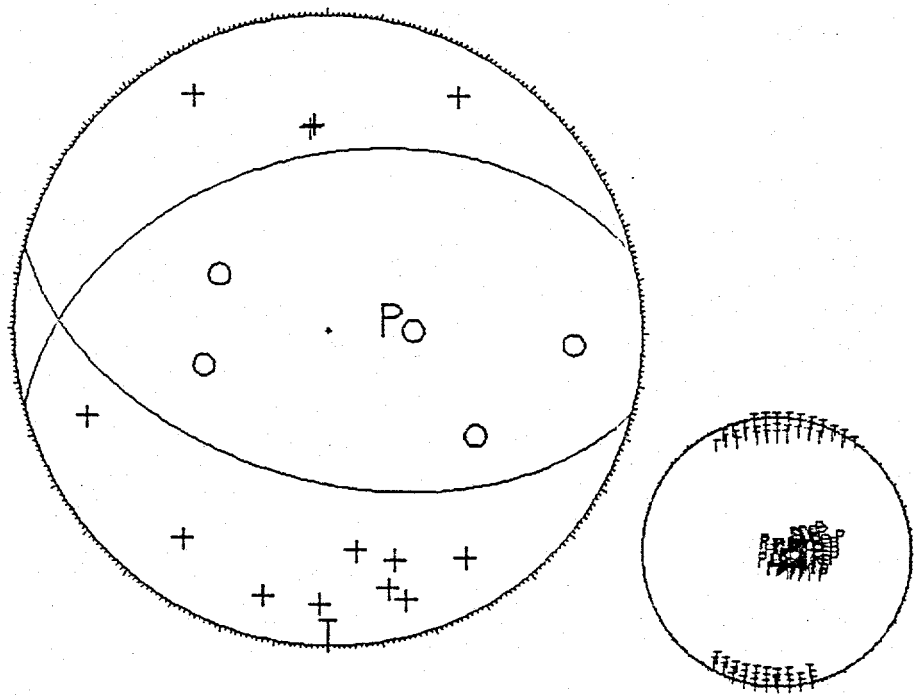

WARM SPRING SEGMENT

840903 2028 .60 44-19.88 114- 3.40 9.87 2.30 19 105 5.0 .07 .6 1.1

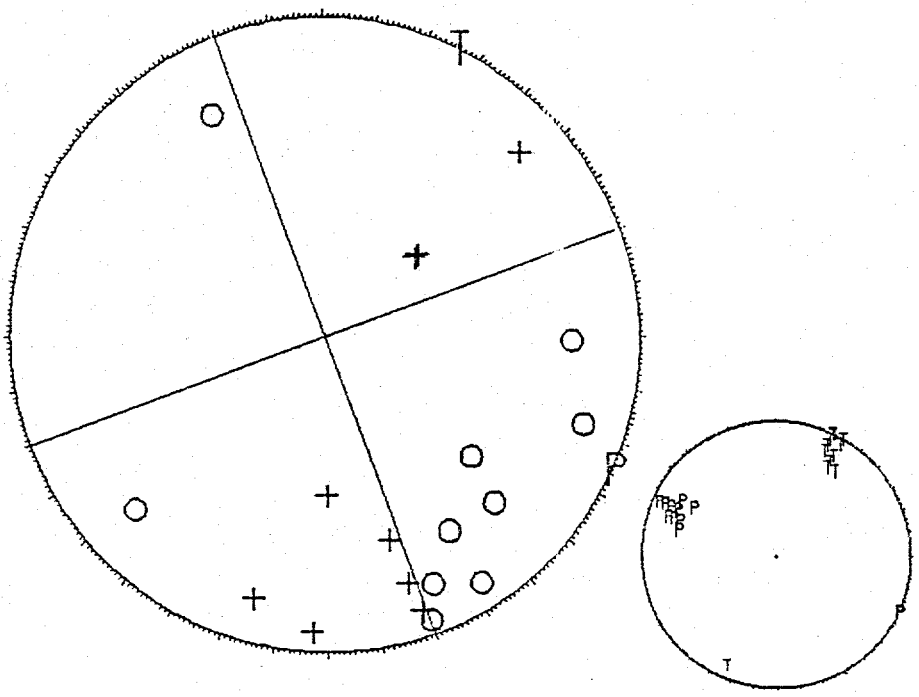

840831 2046 16.28 44-20.23 114- 3.24 9.28 1.40 18 72 6.0 .07 .4 1.1

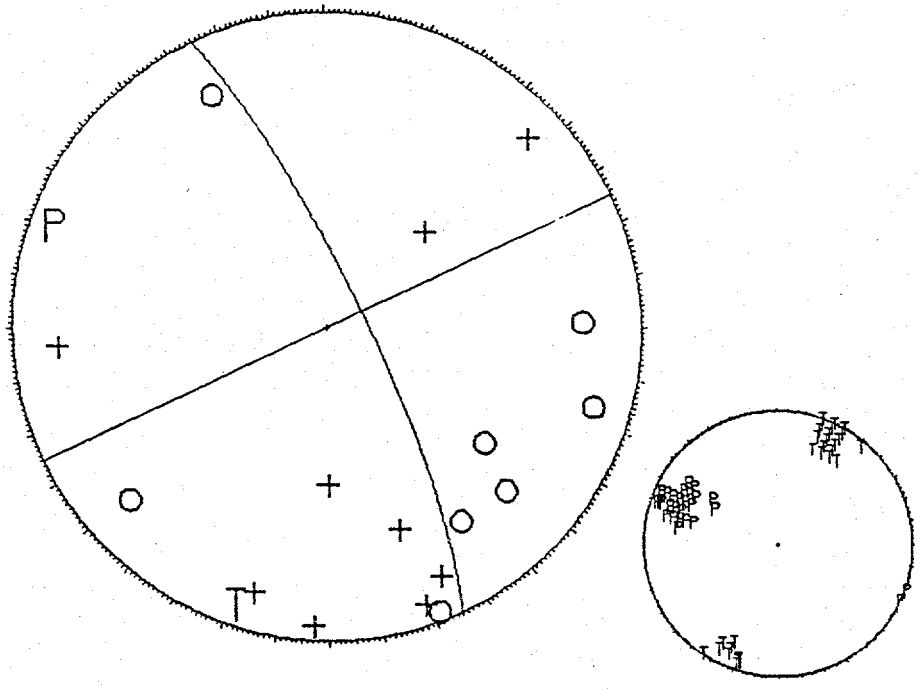

SOUTHERN PORTION OF THE LONE PINE FAULT

840829 947 51.16 44-20.10 114- 5.47 7.92 2.50 14 66 4.0 .09 .6 1.4

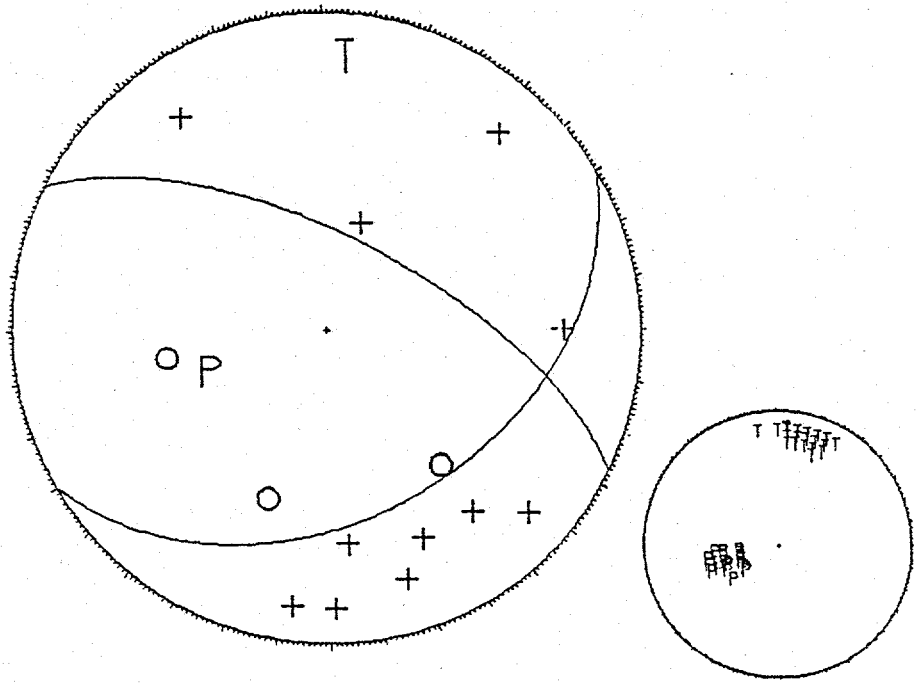

840829 951 14.17 44-20.04 114- 5.09 8.33 1.80 18 62 4.0 .09 .5 1.0

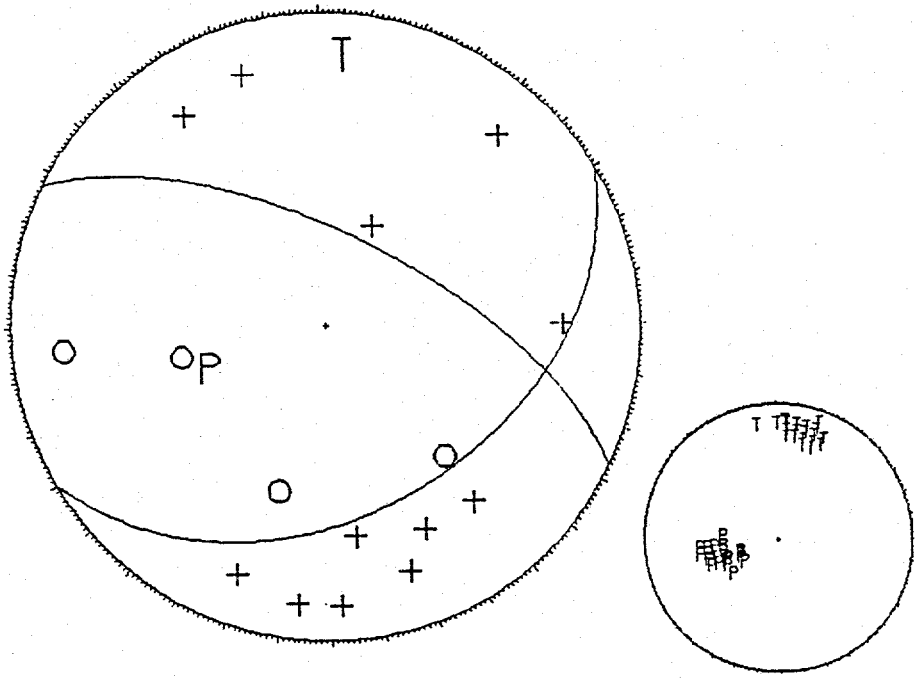

CHALLIS SEGMENT

Upper boundary of intermediate layer (5.9 km/s) at 8.0 km depth.

840901 455 23.82 44-25.91 114- 5.82 8.85 1.30 19 43 1.0 .04 .4 .8

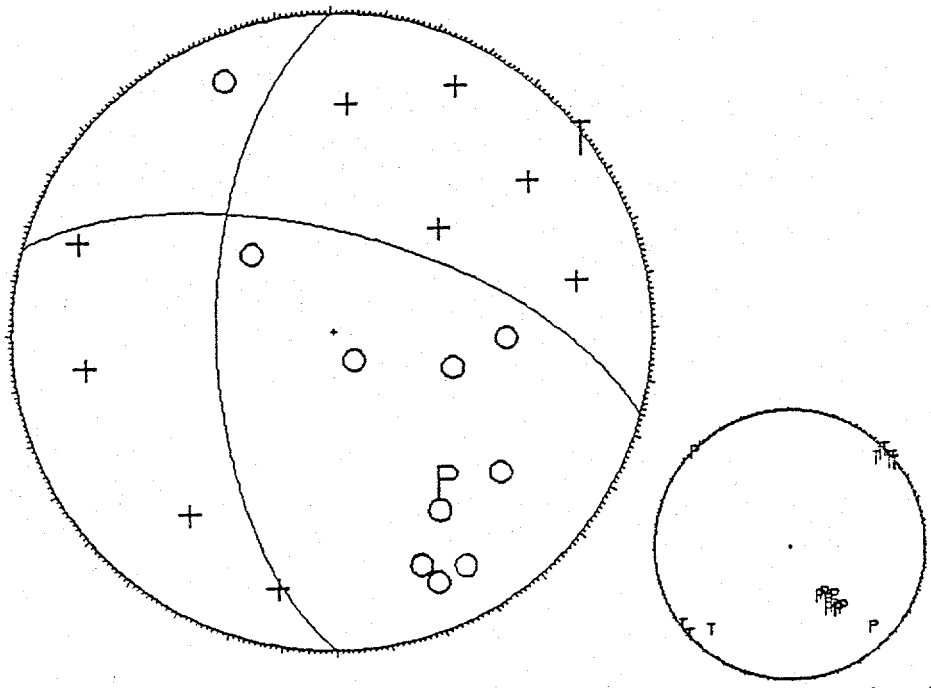

Upper boundary of intermediate layer (5.9 km/s) at 9.0 km depth.

840901 455 23.86 44-25.92 114- 5.81 8.55 1.30 19 43 1.0 .04 .4 .8

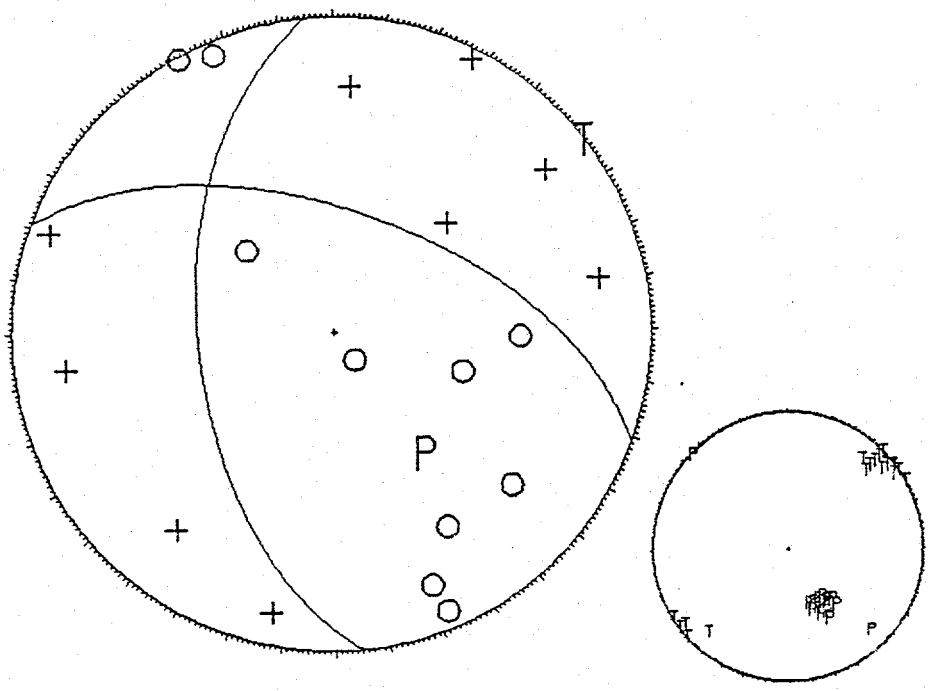

CHALLIS SEGMENT

Upper boundary of intermediate layer (5.9 km/s) at 8.0 km depth.

840905 22 46.93 44-25.82 114- 5.83 8.39 1.10 21 68 1.0 .05 .4 .8

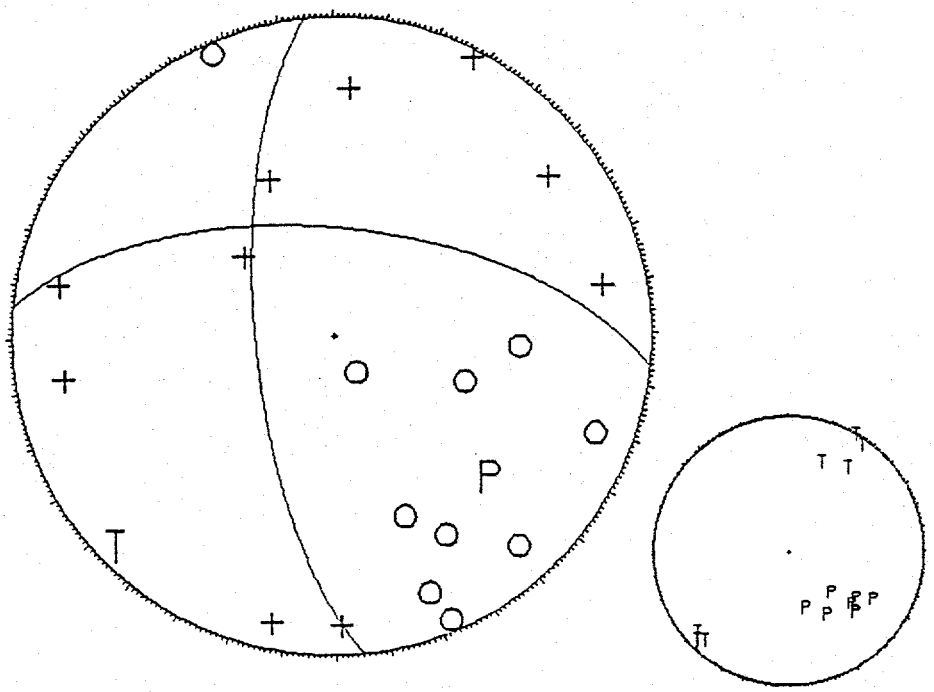

Upper boundary of intermediate layer (5.9 km/s) at 9.0 km depth.

840905 22 46.91 44-25.81 114- 5.85 8.44 1.10 21 68 1.0 .05 .4 .9

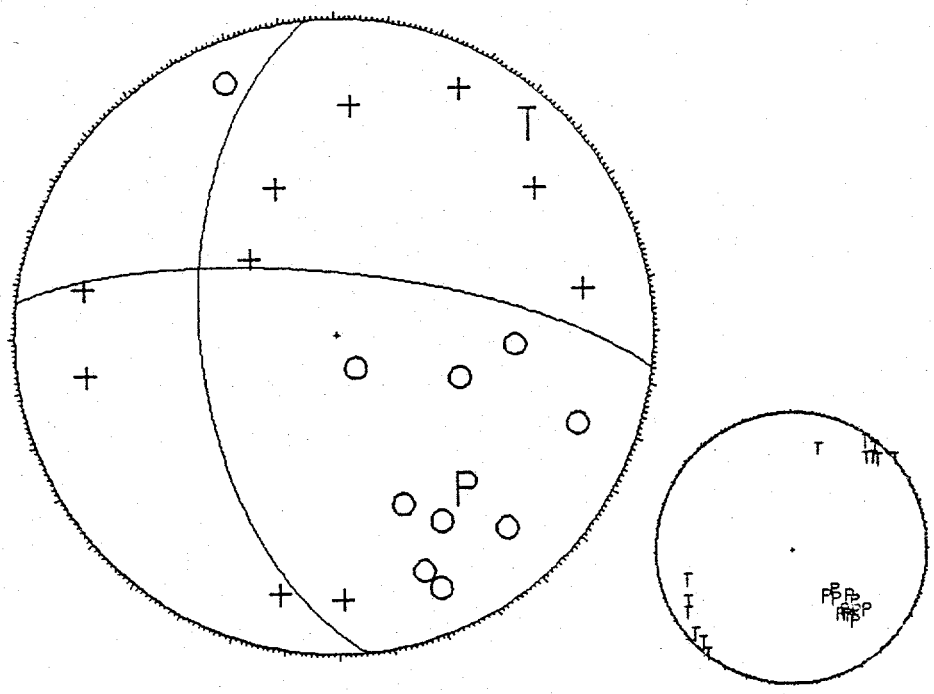

CHALLIS SEGMENT

Upper boundary of intermediate layer (5.9 km/s) at 8.0 km depth.

840905 436 39.63 44-22.46 114- 4.02 8.65 1.40 21 68 .0 .04 .4 .8

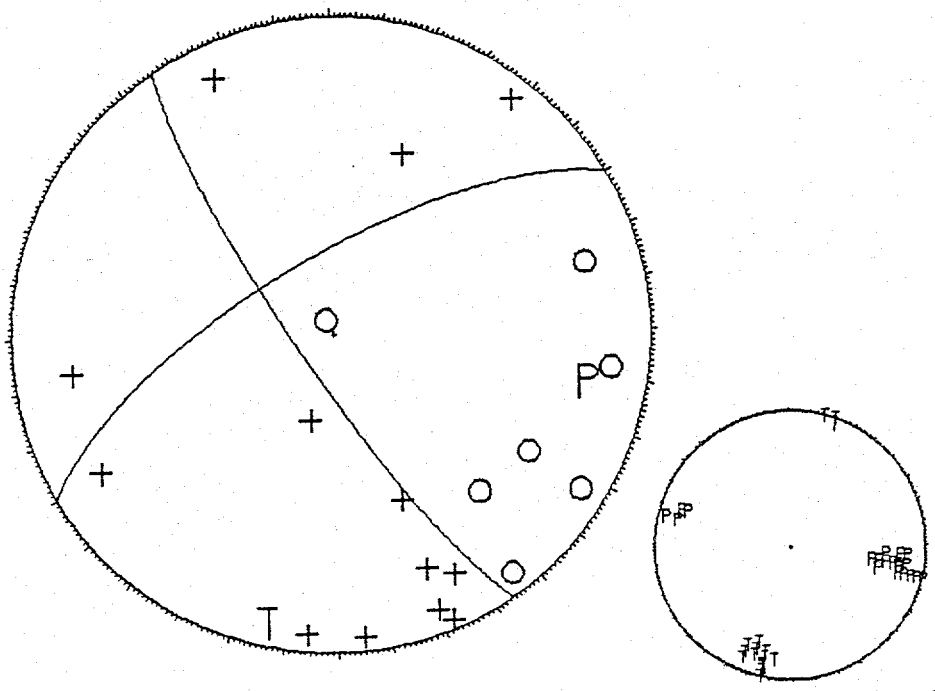

Upper boundary of intermediate layer (5.9 km/s) at 9.0 km depth.

840905 436 39.60 44-22.47 114- 4.01 8.79 1.40 21 70 .0 .04 .4 .9

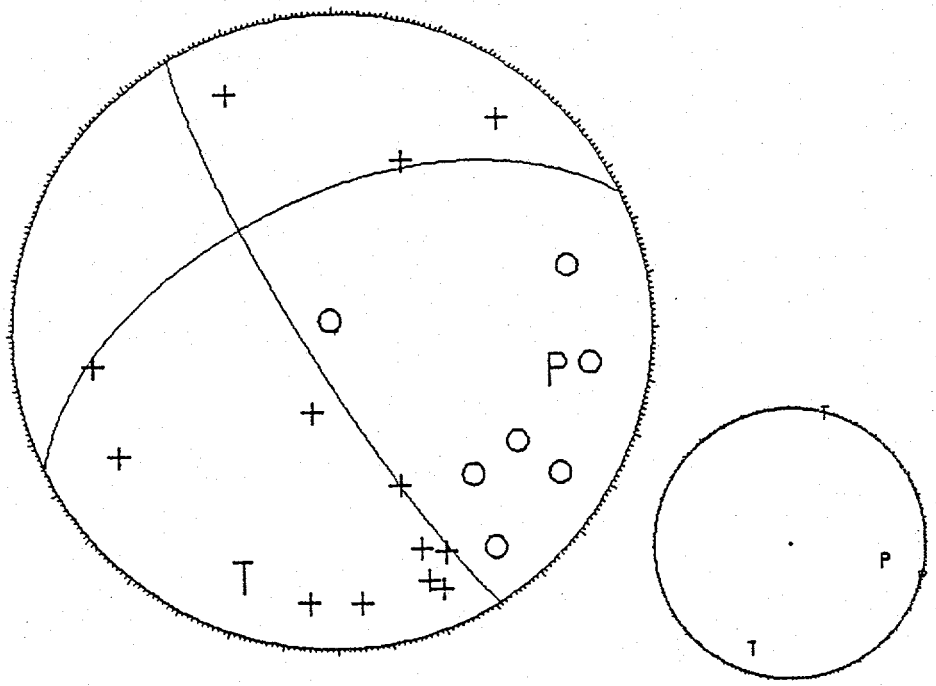

CHALLIS SEGMENT

Upper boundary of intermediate layer (5.9 km/s) at 8.0 km depth.

840909 501 53.43 44-23.17 114- 4.83 8.76 1.50 21 56 2.0 .05 .4 .8

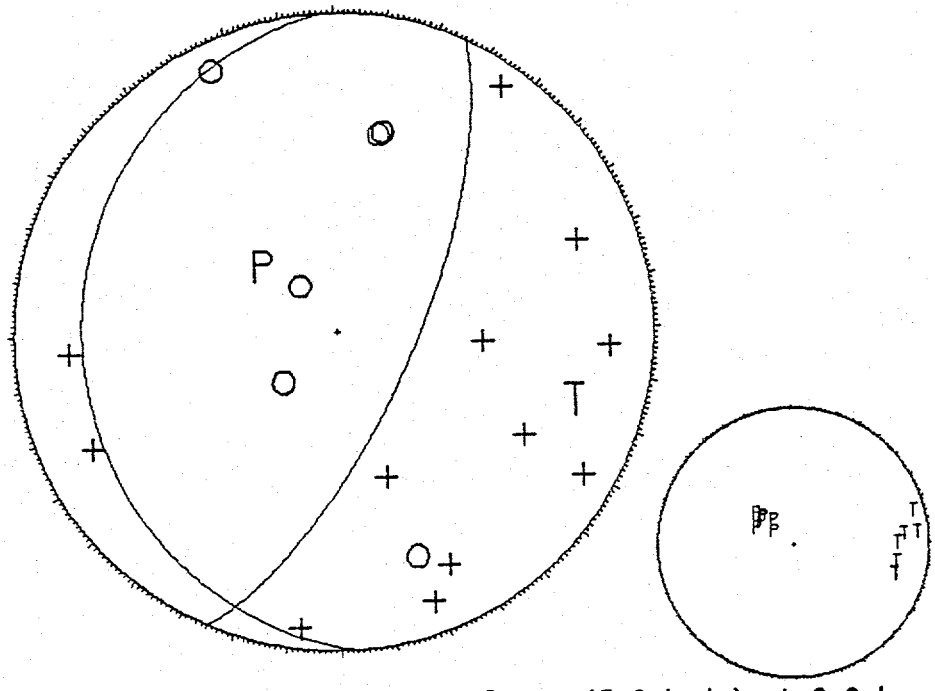

Upper boundary of intermediate layer (5.9 km/s) at 9.0 km depth.

840909 501 53.40 44-23.17 114- 4.84 8.94 1.50 21 56 2.0 .05 .4 .8

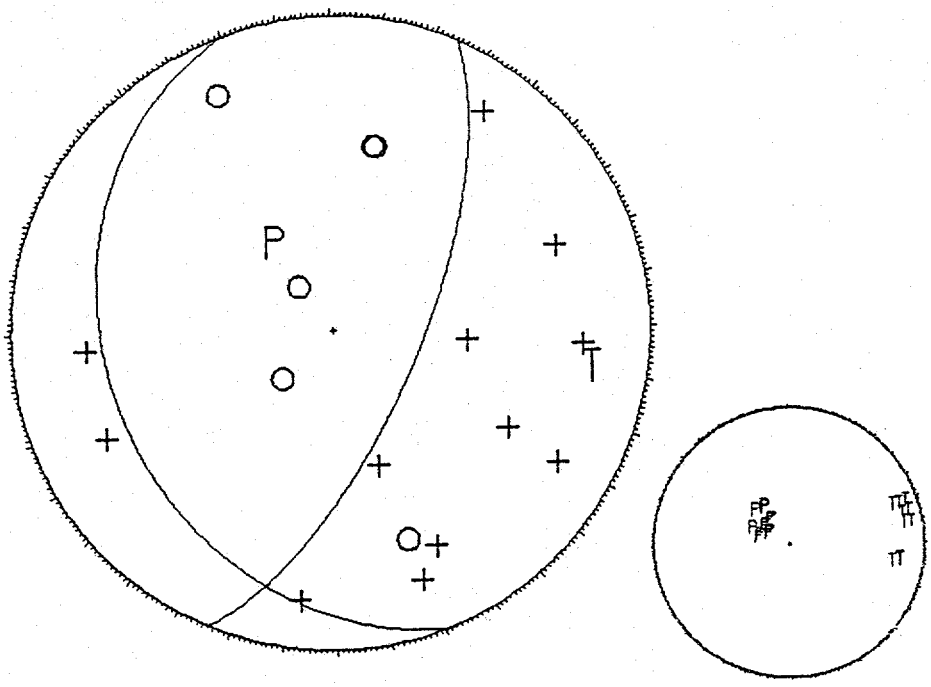

LONE PINE FAULT

Upper boundary of intermediate layer (5.9 km/s) at 8.0 km depth.

840830 1514 23.69 44-24.60 114- 6.53 8.98 1.40 20 61 3.0 .05 .4 .8

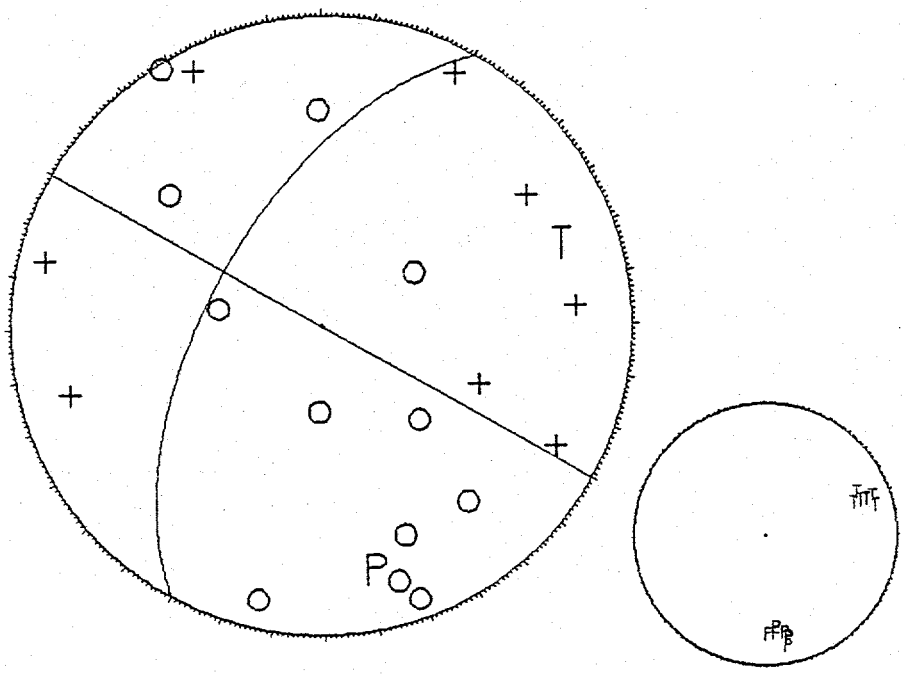

Upper boundary of intermediate layer (5.9 km/s) at 9.0 km depth.

840830 1514 23.66 44-24.59 114- 6.53 9.15 1.40 20 61 3.0 .05 .4 .7

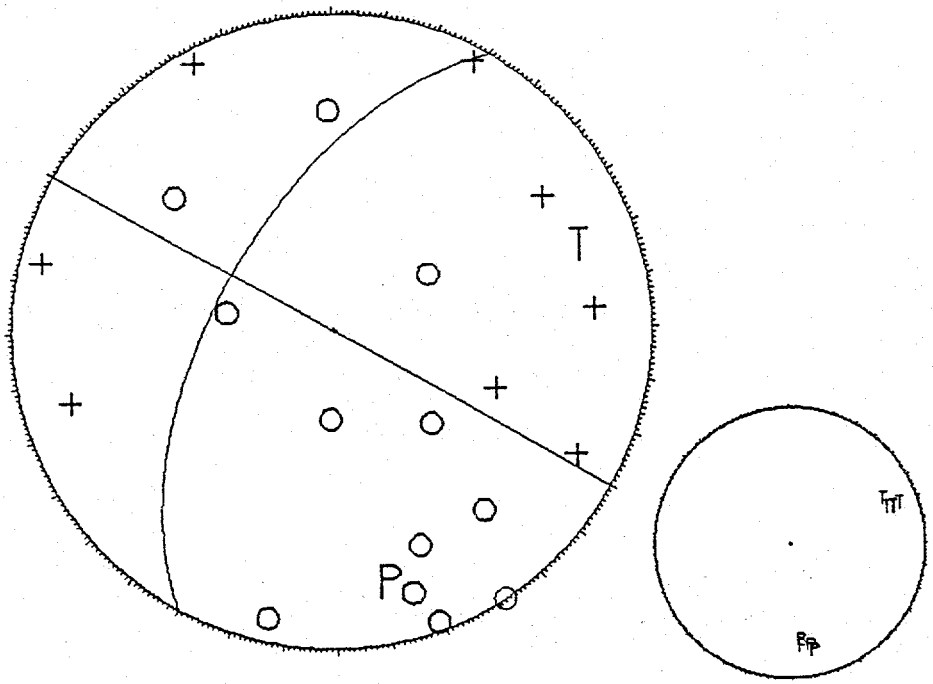

LONE PINE FAULT

Upper boundary of intermediate layer (5.9 km/s) at 8.0 km depth.

840830 1842 27.39 44-23.94 114- 6.70 9.07 2.60 20 57 4.0 .05 .4 .8

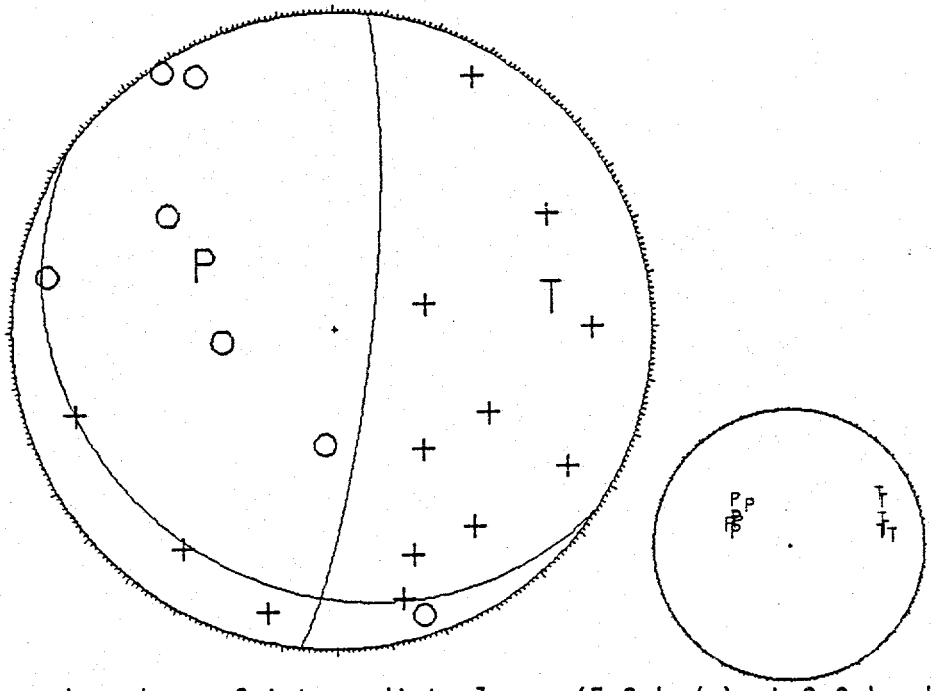

Upper boundary of intermediate layer (5.9 km/s) at 9.0 km depth.

840830 1842 27.36 44-23.92 114- 6.69 9.29 2.60 20 57 4.0 .05 .4 .8

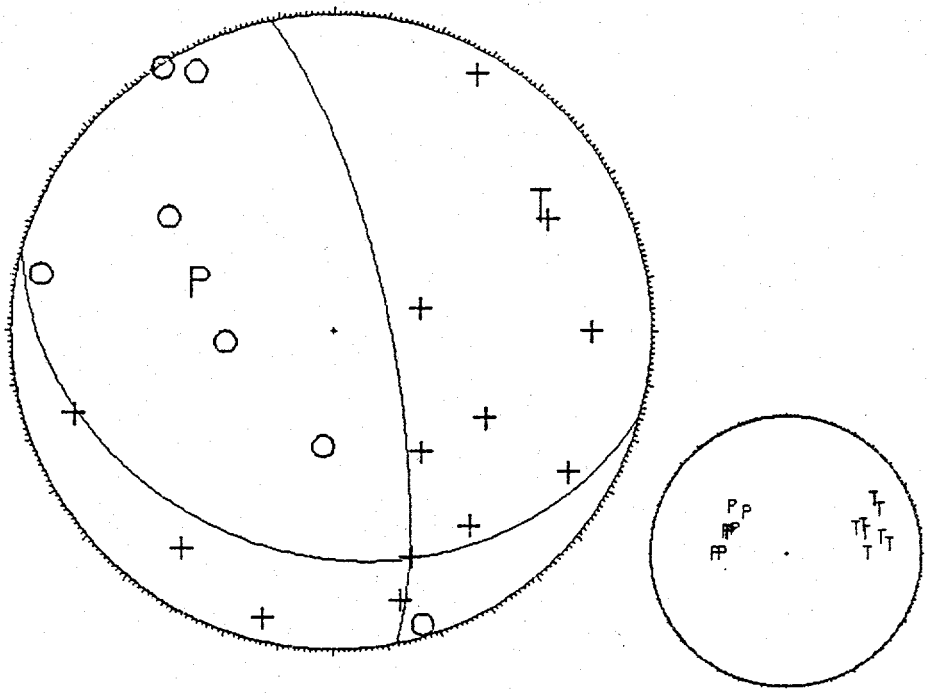

LONE PINE FAULT

Upper boundary of intermediate layer (5.9 km/s) at 8.0 km depth.

840901 634 44.90 44-23.58 114- 6.69 9.29 1.70 19 46 4.0 .04 .4 .8

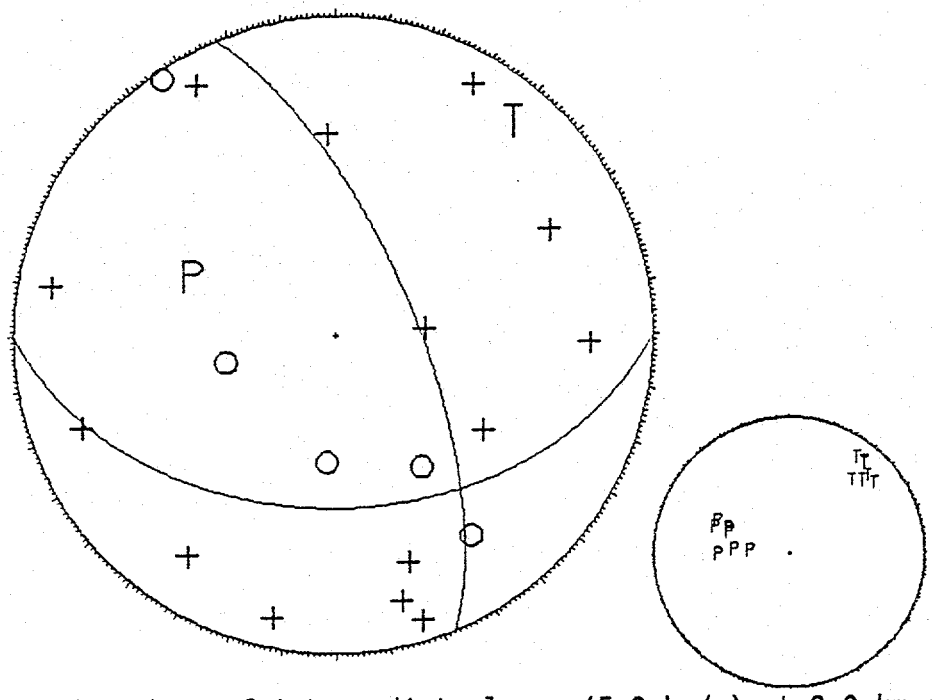

Upper boundary of intermediate layer (5.9 km/s) at 9.0 km depth.

840901 634 44.87 44-23.57 114- 6.69 9.45 1.70 19 46 4.0 .04 .4 .8

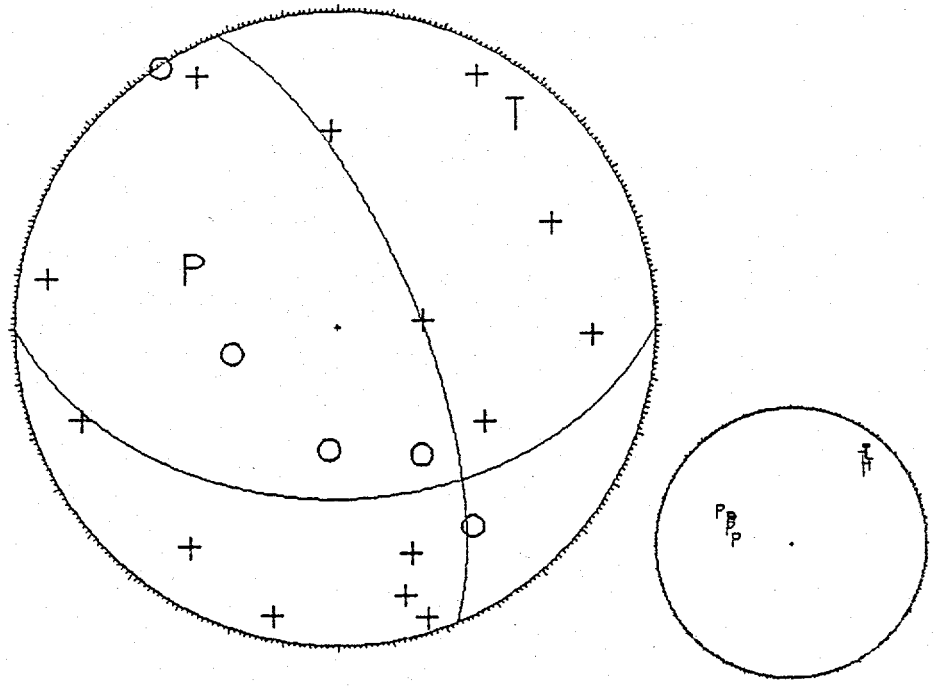

LONE PINE FAULT

Upper boundary of intermediate layer (5.9 km/s) at 8.0 km depth.

840905 1738 58.65 44-23.33 114- 6.94 8.09 2.70 20 62 5.0 .05 .4 .8

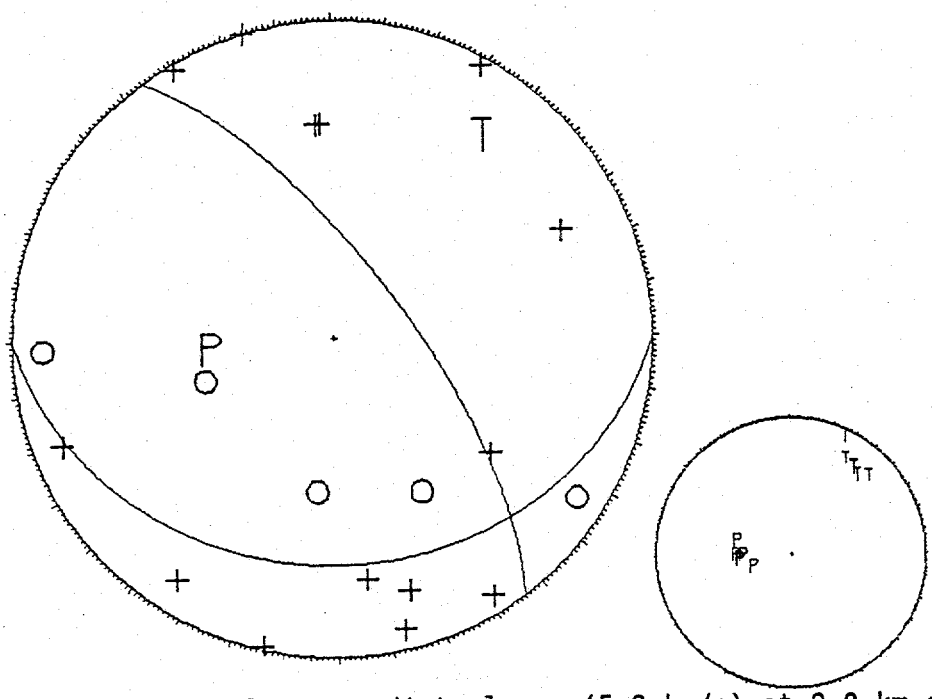

Upper boundary of intermediate layer (5.9 km/s) at 9.0 km depth.

840905 1738 58.64 44-23.33 114- 6.93 8.14 2.70 20 62 5.0 .05 .4 1.1